Electronic Theses and Dissertations, 2004-2019

2013

Microstrip Patch Electrically Steerable Parasitic Array Radiators

Justin Luther
University of Central Florida

Showcase of Text, Archives, Research & Scholarship

MICROSTRIP PATCH ELECTRICALLY STEERABLE PARASITIC ARRAY RADIATORS

by

JUSTIN LUTHER
B.S. University of Central Florida, 2008
M.S. University of Central Florida, 2010

A dissertation submitted in partial fulfillment of the requirements
for the degree of Doctor of Philosophy
in the Department of Electrical Engineering and Computer Science
in the College of Engineering & Computer Science
at the University of Central Florida
Orlando, Florida

Spring Term
2013

Major Professor: Xun Gong

ABSTRACT

This dissertation explores the expansion of the Electrically Steerable Parasitic Array Radiator (ESPAR) technology to arrays using microstrip patch elements. Scanning arrays of two and three closely-coupled rectangular patch elements are presented, which incorporate no phase shifters. These arrays achieve directive radiation patterns and scanning of up to 26° with maintained impedance match. The scanning is effected by tunable reactive loads which are used to control the mutual coupling between the elements, as well as additional loads which compensate to maintain the appropriate resonant frequency. The design incorporates theoretical analysis of the system of coupled antennas with full-wave simulation. A prototype of the three-element array at 1 GHz is fabricated and measured to exhibit a maximum gain of 7.4 dBi with an efficiency of 79.1%. Further, the microstrip ESPAR is thoroughly compared to uniformly-illuminated arrays of similar size.

To satisfy the need for higher directivity antennas with inexpensive electronic scanning, the microstrip ESPAR is then integrated as a subarray. The three-element subcell fabrication is simplified to a single layer with an inverted-Y groove in the ground plane, allowing for DC biasing without the need for the radial biasing stubs or tuning stubs found in the two-layer design. The 1 GHz ESPAR array employs a corporate feed network consisting of a Wilkinson power divider with switchable delay line phase shifts, ring hybrid couplers, and achieves a gain of 12.1 dBi at boresight with ±20° scanning and low side lobes. This array successfully illustrates the cost savings associated with ESPAR subarray scanning and the associated reduction in required number of phase shifters in the RF front end.

For Robin and Kandace

ACKNOWLEDGMENTS

TABLE OF CONTENTS

LIST OF FIGURES

LIST OF TABLES

CHAPTER 1: INTRODUCTION

1.1 Overview

Modern defense and communication systems are heavily dependent on the use of highly directive antennas. Point-to-point communication systems, e.g. satellite communication networks, require large apertures and high transmit powers to overcome the severe free space path loss (FSPL) associated with the distance between the satellite and base station, ensuring a high signal-to-noise ratio (SNR) and consequently low bit error rate (BER). The design of these systems often requires cost/benefit analysis, trading the aperture size and efficiency against the transmitter power to balance size, weight, and power (SWAP) considerations. In the cellular telephony and WiFi areas, the increased demand for bandwidth per user and explosion in number of subscribers has created an environment rife with interference. While efficient spectrum use and frequency selectivity is constantly improved by intelligent modulation schemes and high-Q filters on the RF front end, the receivers in these systems are still subject to higher noise in the form of interference from undesired sources. In each of these systems, the spatial selectivity afforded by highly directive antennas can mean the difference between functionality and failure. The ability to not only actively scan the main beam toward the desired source, but also place pattern nulls on the interference sources, dramatically increases the "signal to interference plus noise ratio," or SINR.

Applications in target detection and tracking may employ multiple large antenna array systems integrated together in an Integrated Air Defense System (IADS.) The rapid and precise scanning ability of Active Electronically Scanned Arrays (AESA) often works in tandem with slower, mechanically scanned systems to provide a robust and comprehensive denial of enemy air. While the directivity of physically large radiating apertures provides a longer maximum target detection range, these smaller beamwidths increase the probability of missing the target entirely should it fall off the beam maximum. The electronic scanning in such phased array antennas allows for a moving target to still be effectively tracked by rapidly adjusting the location of the beam maximum. Unfortunately, the application of this powerful technology has historically been limited to primarily military applications due to the exorbitant fabrication cost.

The beam steering capability of a phased array antenna is traditionally provided by phase shifters. However, phase shifters contribute heavily to the total cost of a phased array system. Additionally, phase shifters exhibit considerable loss at *X*-Band and above, which also generally varies depending on phase shift [1, 2] for digital implementations. This loss directly leads to reduced performance in passive arrays [3]. In such cases, the linear phase shift across the radiating aperture requires progressively larger phase shifts, causing proportionally larger losses subject to the phase shifter loss figure of merit. This creates an inherent magnitude error across the aperture, causing broadening of the main beam and a loss in directivity. Therefore, a reduction in number or elimination of phase shifters is of great fiscal benefit and can significantly improve performance and mean time between failure (MTBF). The reduced cost would allow more widespread use of this technology in both military and civil applications.

1.2 Motivation

The development of the Electrically Steerable Parasitic Array Radiator (ESPAR) has grown from the desire for electrically scanned beams with inexpensive fabrication. The driving concept behind the ESPAR is that radiation from an antenna element fed by a generator can be parasitically coupled to nearby passive elements with an overlapping near-field region. For such antennas, the phase difference of radiating currents between the elements can be tuned by variable reactive loads connected to the parasitic elements. The resulting magnitude and phase changes in the parasitic element radiating currents cause significant variation in the radiation characteristics of the structure.

The immediate benefits of the ESPAR technique are apparent. By utilizing relatively inexpensive tunable reactances, such as reverse-biased diode varactors, an analog reconfigurable antenna system can achieve switched beams, frequency diversity, continuous scanning, or element pattern shaping. Further, integration of adaptive control techniques for the reactive loads can enable frequency stability in a varying environment, or signal tracking for systems mounted on a moving platform. However, such benefits do not come without a new set of functional restraints. While scanning of the main beam is desired, this scanning should not come at the cost of directivity or efficiency, which necessitates low-loss reactive loads; indeed, high-Q capacitors are integral to the feasibility of the ESPAR. A low sidelobe level (SLL) must be maintained, and the resonance of the structure should remain at the intended operation frequency, lest the return loss become unacceptable. Care must be taken to avoid excitation of undesired modes at the

operation frequency. Finally, the magnitude of the parasitic current should not drop sharply with variation in the loads, otherwise lower aperture efficiency will result.

Clearly, the ESPAR technique is a promising approach for reducing the cost of a scanning antenna array.

1.3 Literature Review

1.3.1) Parasitic Arrays

Ongoing research in the field of scanning antenna systems has focused significantly on achieving beam scanning with reduced phase shifters. Designs utilizing RF switches commonly operate by routing the radiating current along isolated paths of varying orientations, allowing polarization switching and variable direction of the main beam [4-6]. However, the binary nature of the switches does not lead to great precision in the beam scanning, precluding their use in systems where highly-directive and finely scanned beams are required; sharing the given aperture area with mutually-exclusive radiating sections lends to low aperture efficiency. For example, the microstrip Yagi-Uda pattern reconfigurable antenna presented in [7] contains 4-way rotational symmetry. The return loss, gain, and pattern shape is necessarily identical for the 4 scan cases, but additional resolution in azimuth beyond the 4 cardinal directions is not achieved due to the binary RF switches and heavily discretized rotational symmetry. Further, the guarantee of identical return loss for different switched configurations is dependent on symmetry

in the structure; configurations which lack symmetry with other modes will not necessarily maintain high performance in any of the critical metrics.

It is clear that analog tuning capability should alleviate this concern. Additionally, the desire for high directivity will require that the proposed solution will be readily integrated into a larger coherent radiating aperture. The best candidate for such an antenna will have consistent and relatively simple and inexpensive fabrication, with a robust planar design and a straightforward control network.

1.3.2) Reactively-controlled Directive Arrays

The first prevalent analog-tuning parasitic scanning array was the work of Roger Harrington in 1974 [8]. In this seminal work, the N-port radiating network is shown to theoretically scan by adjusting reactive loads at the ports. The directive properties of Yagi-Uda antennas are then expanded to include pattern reconfiguration in azimuth. The Yagi-Uda antenna is an array of dipole elements of varying lengths, where a single driven element is parasitically coupled with multiple passive elements at computed spacings [9]. This antenna was developed as a narrowband directive single element and is arguably the most well-known example of radiation enhancement using parasitic elements. However, the reactively controlled directive arrays developed by Harrington used only a centered driven element, and a ring of parasitic dipoles at an equal angular separation, as shown in Figure 1. In this way, the variable spacing and length of the Yagi-Uda parasitic elements are made obsolete by the presence of the variable load as a phase-control mechanism. Depending on the desired main beam direction, the phases of the parasitic element currents are controlled by the reactive loads, allowing azimuthal scanning.

5

However, elevation scanning is not possible in this array. Also, the lack of groundplane results in large backlobes for certain scan angles, precluding their use in larger arrays.
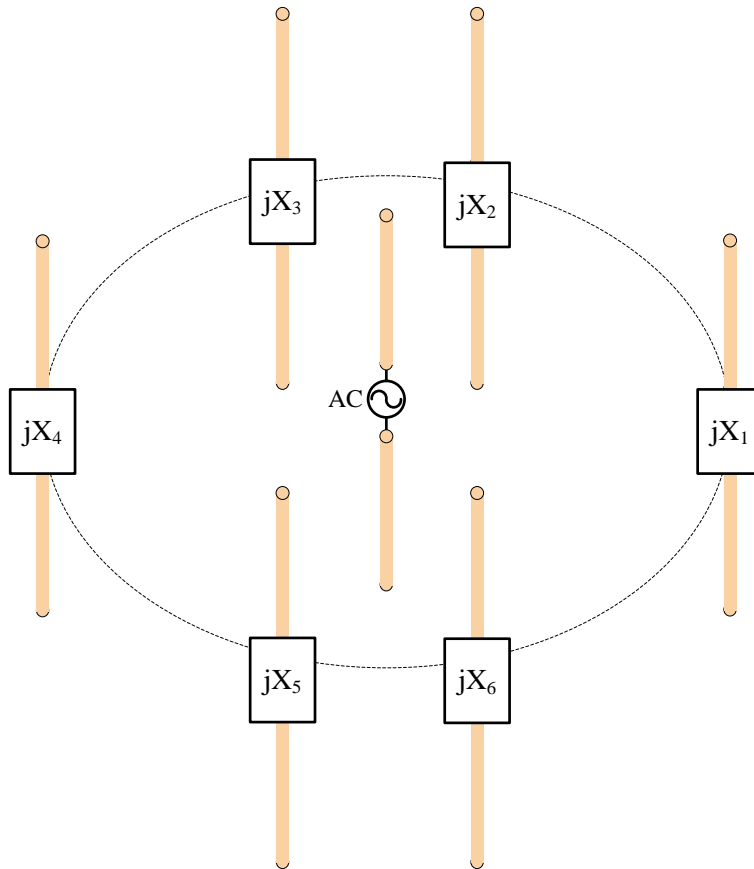
Figure 1: The reactively controlled directive array.

1.3.3) The ESPAR

The ESPAR antenna has been an active area of research for the past 10 years. With a primary focus of wireless ad-hoc networks, the scanning ability of this inexpensive antenna array is meant to allow improvement in battery life by ensuring maximum directivity in the direction of the next link, allowing reduction of power to the RF amplifier stage [10]. The N-port network theory of the reactively-controlled arrays applies regardless of element type, allowing the

ESPAR category to vary widely in application and function. In the first significant design improvement, the profile of the parasitic array is reduced by replacing the dipole elements with monopoles above a ground plane [11]. A conductive skirt around the edge of the ground plane provides protective housing to the RF feed circuitry beneath the ground and serves to maximize the horizontal gain. Further improvement to the device profile is made in [12], where a dielectric slab is placed to totally encompass the monopole elements, significantly reducing their length and shrinking the device diameter. However, this device still lacks elevation scanning capability, and its ability to be incorporated into electrically large arrays has yet to be explored. Manufacture of these prototypes is also a complicated process compared to traditional PCB fabrication, requiring precise machining of the ground and skirt and custom processing of the dielectric material. For these reasons, the simpler PCB fabrication process associated with microstrip antenna arrays has sparked research into expansion of the ESPAR to planar arrays with the PCB technique.

A direct transfer of the ESPAR technique to employ microstrip circuits has been explored previously. This work began with characterization of the coupling between patch elements in the E-Plane and H-Plane [13-15], which showed some common trends. First, substantial magnitude coupling is possible with coupling in both planes, which ensures that the technique can accommodate parasitic elements coupled to the driven element along both principal planes. Second, coupling these elements together can cause an apparent increase in the impedance bandwidth of the device. It must be noted, however, that this increased impedance bandwidth

comes at the cost of changing pattern shape and beam squinting, and is therefore not useful for some applications.

A microstrip patch parasitic array with H-Plane coupling and using the ESPAR technique was presented in [16]. In this design, beam scanning was effected by placing tunable reactive loads at the ports of patch elements which are mutually coupled to the driven element. This technique is directly analogous to the dipole and monopole ESPAR forms. Radiation pattern scanning is achieved, however the reactive loads are changed by swapping out various static value capacitors. Therefore, the issue of integrated DC biasing is left unsolved. Further, some scan cases resulted in very low magnitude current on at least one parasitic element, causing growth of sidelobes which reached within 3 dB of the main lobe. A second design was published in [17], where priority was given to the SINR rather than to maintaining low return loss. This device featured coupled patch elements in both principal planes and achieved scanning toward the 4 cardinal directions as well as the boresight. While this array may be well suited to single ESPAR array applications as a low power RF transmitter, the integration of this device into a larger array would be difficult considering the poor impedance matching.

The proceeding chapters show the full transition of the ESPAR technique to include microstrip patch antennas and the maturation of the design procedure. With the introduction of additional reactive loading locations on the parasitic elements, the mutual coupling between the antennas is more controlled, ensuring high magnitude parasitic currents and good pattern shapes. Further, the resonant frequency of the structure is carefully maintained at the desired operation frequency, ensuring high return loss for all scan cases. The simplified fabrication of printed

8

circuits is used to create low-cost prototypes for both the ESPAR array and a larger array of integrated ESPAR subcells. These devices include fully implemented DC biasing for the varactors. In this manner, the goal of achieving a design methodology for low-profile, electrically large parasitic phased array with reduced phase shifters is achieved.

CHAPTER 2: REACTIVELY-LOADED AND COUPLED MICROSTRIP PATCH ANTENNAS

2.1 Rectangular microstrip patch antennas

Rectangular microstrip patch antennas are commonly used as standalone radiators, and as elements in larger phased array antennas. This popularity is highly due to the simplicity of their fabrication and low profile nature. While inset microstrip lines, coaxial pins, and ground plane coupling apertures are widely-employed methods for feeding these antennas [18], rectangular patches without feed circuits are also utilized as parasitic elements in phased arrays, and as reflector elements in reflectarrays [19, 20]. The design of reconfigurable phased arrays and reflectarrays specifically requires accurate modeling of these feedless antennas in order to predict the more complex behavior of the elements as well as the mutual coupling between them.

Analysis of the rectangular microstrip patch antenna generally focuses on one of a few common models. Determination of the resonant frequencies of the antenna can be performed by solving Maxwell's equations inside the structure, which is normally accomplished through numerical techniques and is always valid. The most common of the analysis approaches are the cavity model and the transmission-line model because of their intuitive natures and straightforward application. These techniques each provide a reasonably fast approach for determining the fundamental resonant frequency. However, the transmission-line model is less accurate, and does not yield much insight into the radiation characteristics of the device.

An expedient method is presented to calculate the lumped element values of the equivalent parallel resonator circuit for a rectangular microstrip patch antenna. The model is shown to accurately predict the resonant behavior of patch antennas lacking traditional feed circuits, such as parasitic patch antennas and reflectarray unit cells. The cavity model of the rectangular patch provides the basis for analysis of the effect of tunable reactive loading on the fundamental mode resonant frequency. Predictions from the model are compared to full-wave simulation and show excellent agreement.

In the microstrip patch ESPAR antenna, microstrip patches with feeds are coupled, via close proximity, to feedless parasitic patches. This mutual coupling is tuned by way of variable reactive loads; additional variable loads are used on the parasitic elements to control the resonant frequency and maintain impedance matching. As the reactive loads control both coupling and resonant frequency, the exact load values must be precisely known. Parametric analysis in full-wave solver packages can provide these values at the cost of extensive computation time. However, a precise equivalent circuit model for the driven element, the coupling network, and the parasitic elements, will dramatically reduce this computation requirement and expedite the design process.

To account for the reactive loading effect on resonant frequency and the lack of a traditional feed, the cavity model of the rectangular microstrip patch is combined with the parallel RLC representation of the equivalent circuit and ESPAR reactive loading. This combination yields a method for extraction of accurate equivalent circuit model parameters for the feedless microstrip patch from full-wave simulations. The resultant model accurately predicts

11

the resonant frequency of the reactively loaded rectangular patch for various loads and loading locations. This technique allows the circuit model parameters to be found using as few as two full-wave simulations, for the unloaded patch, and a loaded case. Excellent agreement is found between the equivalent circuit model and a full-wave parametric analysis of the problem, illustrating the potential for saved simulation time.

2.2 Equivalent circuit representation

The equivalent circuit model of the rectangular patch antenna is a resonant parallel RLC circuit. The values for L and C are determined by the electromagnetic fields in the near field of the antenna, and represent the capacity for stored magnetic and electric energy in the circuit during resonance. As such, both parameters are greatly completely governed by the geometry of the structure and any connected loads. Additionally, parasitic reactance in the feed network can be reflected into the circuit and affect the resonant frequency; this effect is obviously ignored for the present case of feedless antennas. The resonant frequency of this circuit is given by Equation 1 and occurs at the frequency where the stored magnetic and electric energy are equal [21]:

$$2\pi f_0 = \frac{1}{\sqrt{LC_U}}.$$

(1)

C_U represents the total capacitance of the unloaded rectangular patch structure, and f_0 is the resonant frequency of the fundamental mode before loading.
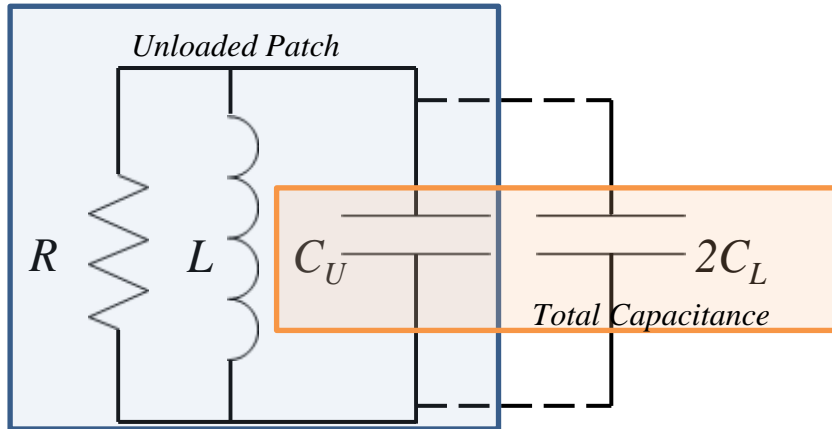
Figure 2: Parallel RLC circuit representation of the symmetrically loaded patch.

Assuming that the primary consequence of loading the patch with a pair of capacitors C_L is to store some additional electric energy in the circuit, then the total capacitance becomes the parallel combination of this load with the unloaded capacitance C_U, as seen in Figure 2.

Assuming L is unchanged, the loaded resonant frequency f_L is

$$2\pi f_L = \frac{1}{\sqrt{L(C_U + 2C_L)}}. \tag{2}$$

Given that these loads are known and the resonant frequencies are able to be extracted through full-wave simulation, the unloaded patch lumped element value for C_U is given by:

$$C_U = \frac{2C_L}{\left(\frac{f_0}{f_L}\right)^2 - 1}. \tag{3}$$

L is then easily found by back-substitution into equations (1) or (2). R is related to the quality factor of the patch and is also quickly calculable [19].

13

The effective value of C_L for use in (2) and (3) is dependent on the loading location in the structure. The relative magnitude of the voltage at the loading point controls the total possible contribution of additional electric stored energy in the resonant circuit. Therefore, C_{LEFF} is directly impacted by the electric field distribution inside the structure. For a rectangular patch in the fundamental mode, this relative voltage magnitude varies sinusoidally along the resonant edge, with the potential energy storage dependent on the squared cosine of the offset O divided by the total patch length, L_P :

$$C_{LEFF} = C_L \cos^2(\pi\alpha), \tag{4}$$

$$\alpha = \frac{O}{L_P}$$

The loading point must be selected to balance the sensitivity of the resonant frequency to the loading value and the diminished range of loading reactance. After choosing the loading location, (4) should be used to calculate the precise load value for substitution into (2). Similarly, accurate calculation of the unloaded capacitance requires that the loading location be taken into account.

2.3 Simulation and results

To demonstrate the technique, the feedless rectangular patch modeled is the parasitic element utilized in the single-layer microstrip ESPAR at 1 GHz presented in [20]. In Figure 3, two open-ended stubs, at gap G, are weakly coupled to the patch and traverse to two wave ports.

The gap was increased until the size of the gap no longer affected the perceived resonant frequency, and the final gap size is 10 mm.

This large distance results in an average maximum S_{21} value of -55 dB, peaking at the resonant frequency. The structure is solved for the unloaded case, and for a loading of 3pF with no offset ($O = 0\ mm$.) Using (3) in conjunction with (2) reveals the values for C_U and L to be 31.5 pF and 0.78 nH, respectively. A parametric analysis of C_L from 0.2 pF to 3.6 pF is then performed in HFSS, and the results are plotted against the model predictions in Figure 4. The data trend matches across the range of loads with less than 1% deviation from the full-wave results for any loading.

Figure 3: Weakly-coupled feedless microstrip patch with symmetric capacitive loading.
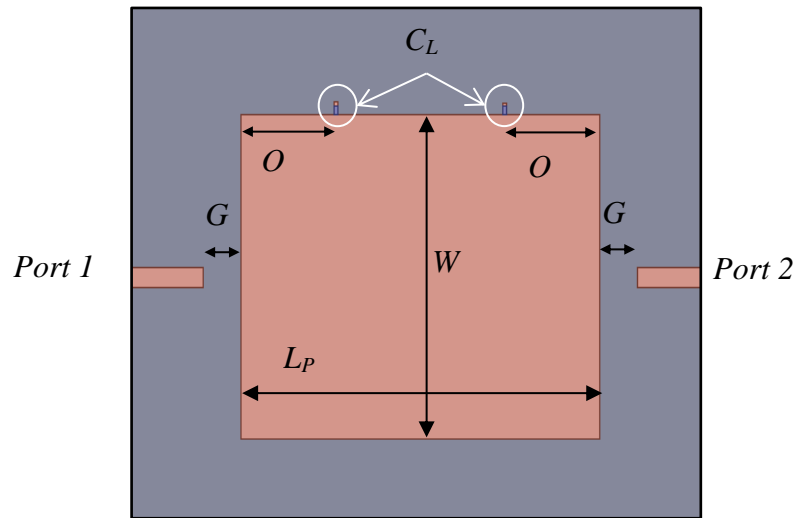
($L_P = 97$, $W = 77$, $G = 10$, $O = 24.25$.) All dimensions
in mm. Substrate: Rogers RT/duroid 5880. Thickness:
62 mil. $\varepsilon_R = 2.2$.

Generation of the full-wave curves of Figure 4 and Figure 5 required simulation of over 20 different loading cases. As the extraction of the circuit model parameters for this example required only two simulations – the unloaded case, and one simulation including a reactive load – it is clear that generation of such design curves for both phased arrays and reflectarray antennas can be greatly expedited without sacrificing accuracy. Further, the reactive loading technique provides the lumped circuit elements accurately even for antennas which will not be reactively loaded in their final stage regardless of the feed mechanism.
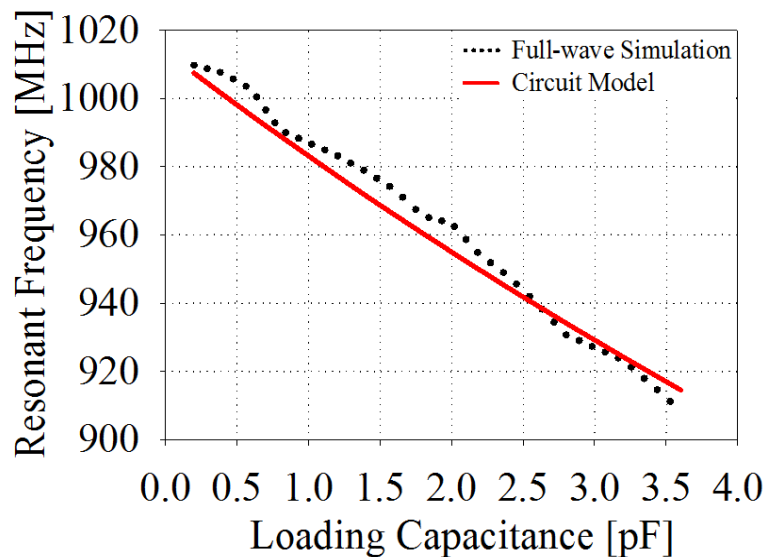
Figure 4: Comparison of full-wave calculated resonant frequency to the circuit model prediction for various load values. [α = 0.]
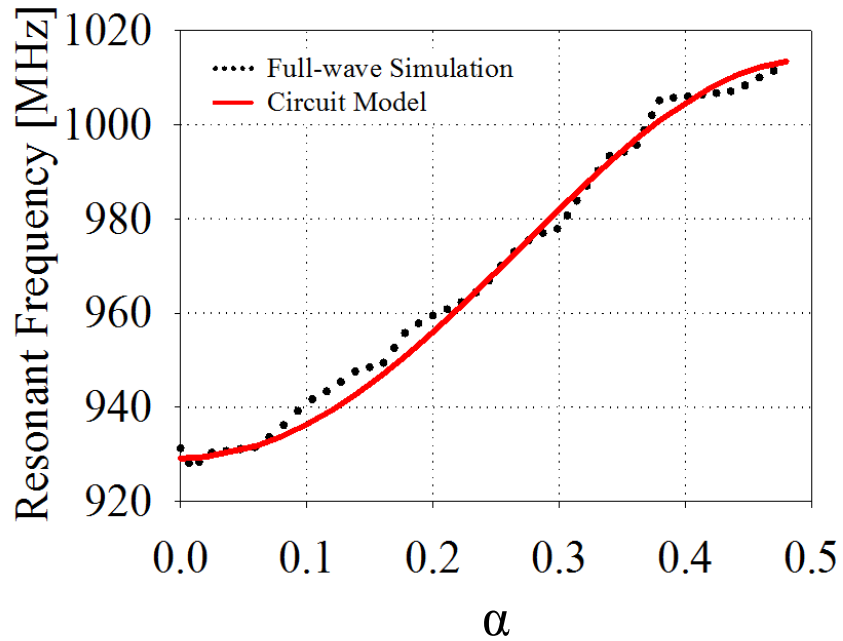
Figure 5: Comparison of full-wave and equivalent model resonant frequency prediction for various loading location.

2.4 Conclusion

The presented technique allows extraction of the equivalent circuit model with reduced simulation time, and without relying on the existence of a traditional feed connection. This method is extendable to resonant antennas, both parasitic and traditionally-fed, and should simplify the design procedure for such systems where an antenna equivalent circuit is beneficial.

17

CHAPTER 3: DESIGN, FABRICATION & MEASUREMENT OF THE 3-ELEMENT MICROSTRIP PATCH ESPAR

3.1 Overview

The undesirable expense associated with phase shifter use in large scanning arrays has stimulated exploration in new, inexpensive methods of achieving pattern reconfigurability. Parasitic and switched elements have been designed to accomplish this task. For parasitic element designs, active arrays will benefit two-fold, as the entire T/R module function is shared among multiple elements for a fraction of the cost without sacrificing aperture efficiency. However, reduction in phase shifter count for scanning arrays has thus far come at the expense of pattern shape, return loss, or precision in the beam scanning.

The ESPAR has been explored previously as a method to reduce the number of traditional phase shifters within a phased array system [8, 11, 12, 16, 17]. The ESPAR exhibits a unique phase shifting mechanism where mutual coupling between adjacent radiators feeds the parasitic radiators, and tunable reactive loading at the terminals of the parasitic radiators creates the necessary phase shift. This type of array has been implemented using a number of element types [12, 16, 17, 22-25]. An ESPAR design employing monopoles, focused on 360° azimuth scanning ability was published in [12]. Similarly symmetric structures were presented in [7, 26]. Such arrays maintain stable radiation patterns and impedance matching during operation; however, this symmetry only holds for a few discrete values of scan angle using switches, precluding their use in continuous range scans and fine angle scan. Microstrip patch antennas

were utilized in [16, 17], which achieved higher total directivity in a low-profile structure. Recently, an ESPAR for handheld mobile platforms was presented [25]. The design consists of a Printed Inverted-F Antenna (PIFA) mutually coupled to two parasitic Inverted-L Antennas with a tunable reactance at the parasitic ports. While this design is well-suited to the mobile device where signal-to-interference ratio (SIR) may be more critical than the absolute power level, a design with higher directivity is better suited to applications in mobile satellite TV systems, point-to-point communications and radar systems.

The resulting radiation patterns in the previous microstrip patch ESPAR variations were generally broad, with low gain. More importantly the mutual coupling was not controlled. Lack of such a control mechanism resulted in tapered distributions across the array, creating broad patterns, and in some instances, large grating lobes occurred at the extrema of the scan angles.
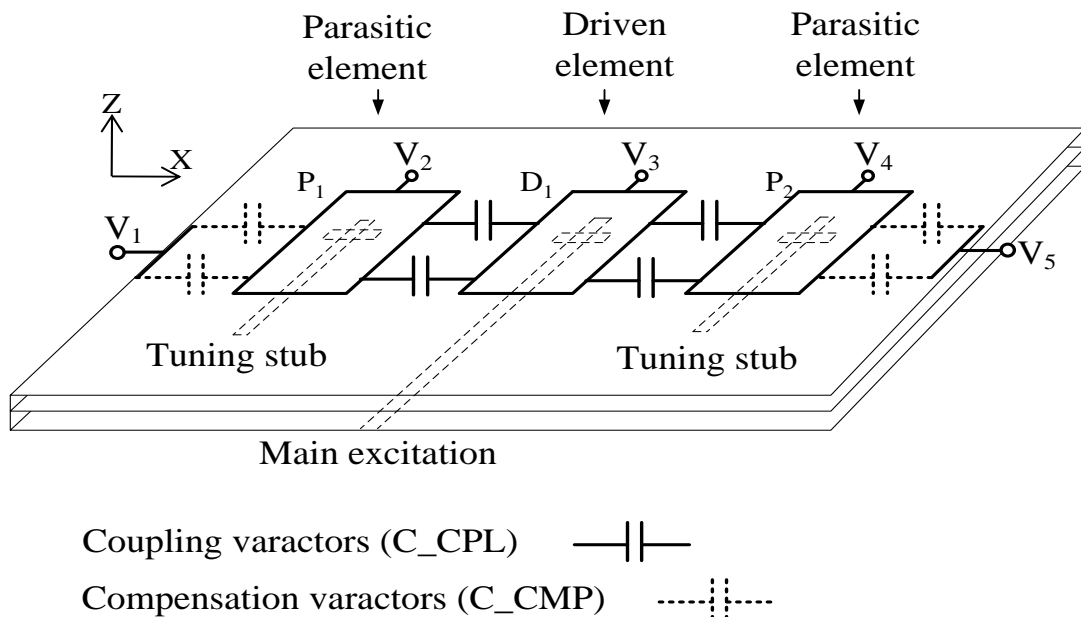
Figure 6: Double-layered microstrip patch ESPAR schematic.
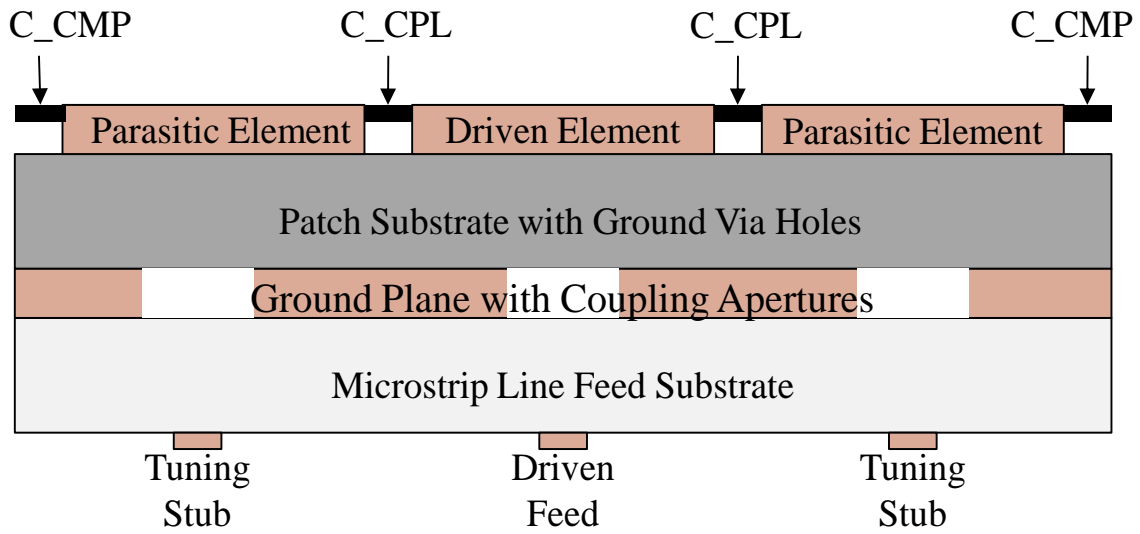
Figure 7: Stacked layer view of the patch ESPAR

Additionally, resonance and impedance matching were not explicitly maintained, to the detriment of total realized gain. The patch ESPAR approach results in a low profile and inexpensive design, but the aforementioned shortcomings necessitate further exploration into novel approaches which improve on our predecessors.

A new configuration of microstrip patch reactively controlled ESPAR with controlled mutual coupling, maintained impedance matching, high gain, and continuous scanning ability is presented. A three-element patch array is designed as shown in Figure 6 and Figure 7. Coupling capacitors, designated as C_CPL, are placed between the driven and parasitic patches as a means to control the coupling between them. To the authors' best knowledge, this is the first use of a variable reactance to tune the mutual coupling in a parasitic array. Compensation varactors, designated as C_CMP, are placed on the parasitic patches to preserve resonance at the operation frequency, which is also a phenomenon which has been largely neglected in previous publications. The coupling and compensation varactors both have an effect on the mutual

coupling between the patches and the structure's resonance. The coupling capacitance has the stronger impact on the mutual coupling, while the compensation varactors have the strongest impact on the overall resonant frequency.

The traditional tunable reactances at the parasitic ports are replaced by open circuited stubs, the lengths of which are optimized in the design stage. This method achieves simulated electronic scanning from -15° to +15° with maintained impedance matching and pattern integrity with no grating lobes and a peak gain at boresight of 7.4 dBi. A traditional, uniformly-illuminated phased array of this size would employ at least two phase shifters, whereas the proposed approach utilizes eight commercially available and inexpensive diode varactors. The junction capacitances of the reverse-biased diodes are directly controlled by the DC voltage biases across them, which are controlled by the bias voltages V_1-V_5 in Figure 6 and Figure 8. A prototype is fabricated and measured, with integrated DC biasing. The theory, design, full-wave simulations, and prototype measurements of this novel array are presented and discussed.

3.2 Theory and design

The design of the patch ESPAR is driven by a small number of critical parameters. The individual patch antennas must be designed, and are defined by their length and width, and feeding mechanism. The feeding apertures, microstrip lines and dielectric materials are primary factors, as are the loading capacitances, tuning and grounding stubs. This design process is illustrated in Figure 8, and shall commence as described below.
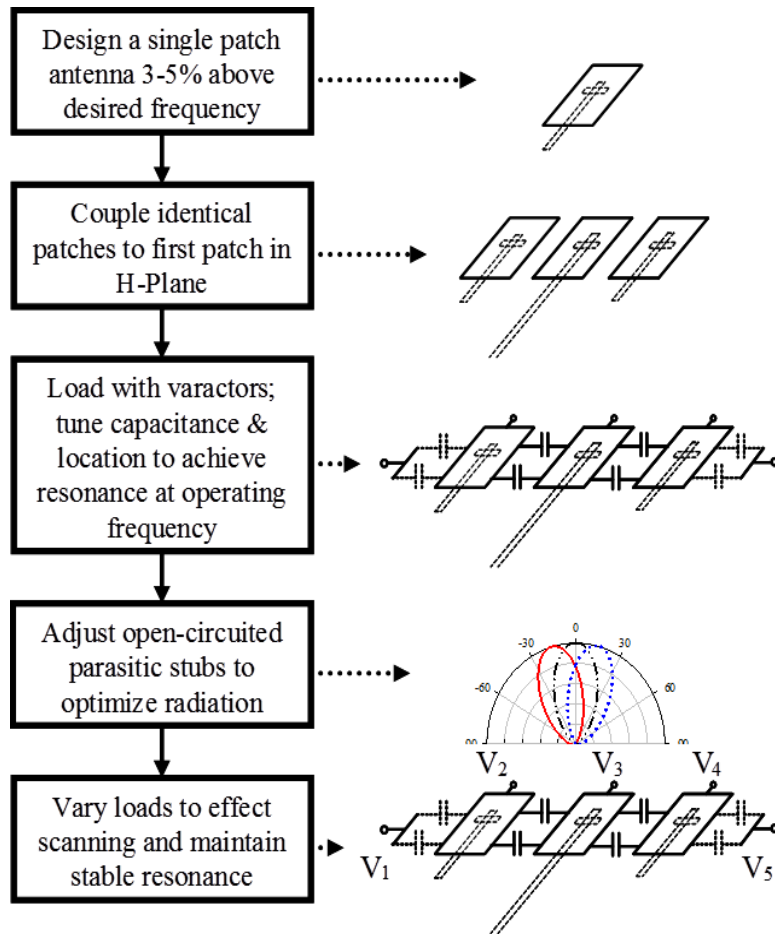
Figure 8: Design flow of the microstrip patch ESPAR

3.2.1) Radiating Element Design

Rectangular patch antennas were selected for their well-known high H-Plane coupling level [15, 27, 28] and ease of fabrication. Mutual coupling between closely-placed patch antennas has previously proven effective as a feed mechanism in [22]. Practical biasing concerns and the desire to expand to a larger array dictates a separation of the feed and radiator layers, and therefore, aperture coupling is utilized as the feed method.

The center antenna is the driving element, and is fed through 50Ω microstrip-to-slot coupling as illustrated in Figure 9, with coupling aperture dimensions L_S and W_S.

(a)

(b)
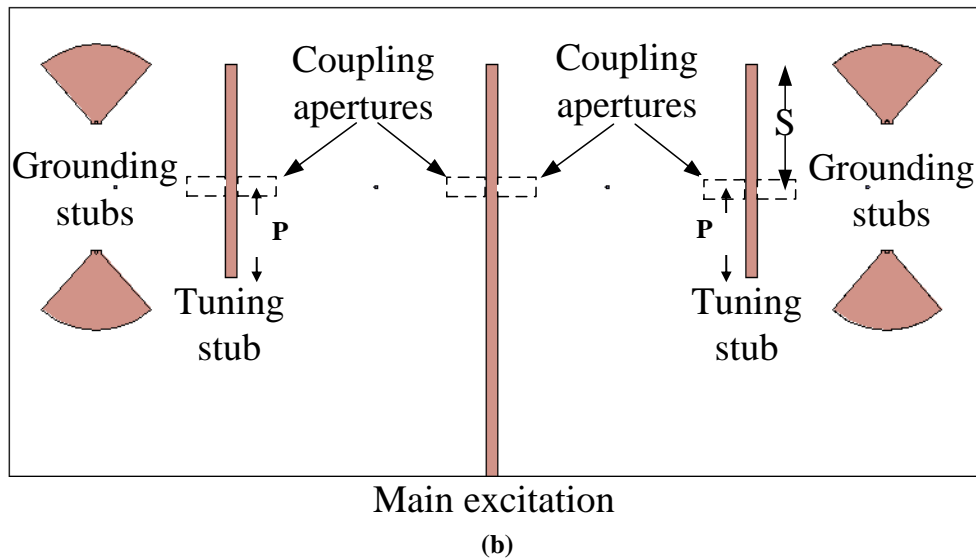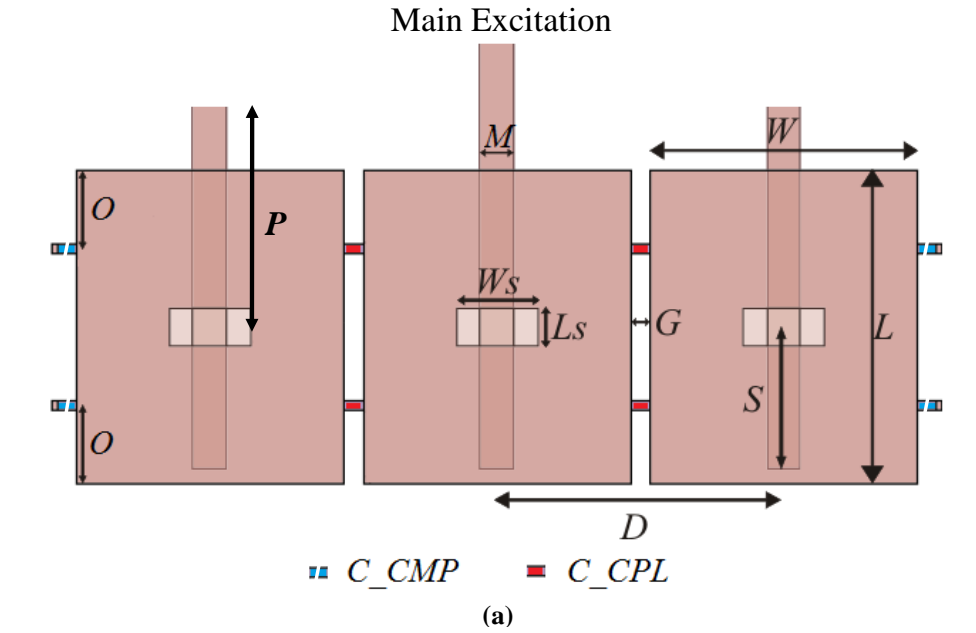
(L = 91, W = 78, D = 81, G = 3, S = 38, WS = 21, LS = 6, O = 25.5, M = 3.5, P = 28). All dimensions are in

Figure 9: Dimensions of the radiating structure. (a) Patch layer. (b) Feed layer.

The antenna dielectric layer consists of 62-mil Rogers Duroid 5880 ($\varepsilon_r = 2.2$, *tanδ* = 0.0009) substrate, while the microstrip feed layer is 60-mil Rogers RO4003 ($\varepsilon_r = 3.55$, *tanδ* = 0.0027) substrate. The low permittivity substrate is selected for the antenna layer for bandwidth considerations, while the higher permittivity is better suited to maintaining a lower backside radiation level from the feed layer.

The parasitic elements are designed identically to the driven element, save for the feeding line. The driven element is connected to the source through a 50-ohm microstrip line, while the parasitic element is terminated with an open-circuited stub offset by a length of transmission line, *P*. The stubs are essentially microstrip resonators which couple to the parasitic patches and affect the magnitude and phase of the induced current. This is analogous to the reactive termination loads of the previous ESPAR designs [8, 11, 12], [22-25]. The stub length is the parameter adjusted during the simulation stage to achieve optimal coupling and pattern characteristics. The array operation frequency is chosen to be 1 GHz. Two identical patches are coupled to the driven element in the H-Plane and the final structure is completely symmetric. Elements are coupled at a gap distance *G*, chosen to realize a desirable coupling level between the antenna elements. Coupling resonant structures, as in the proposed ESPAR, generally causes resonance splitting behavior [29], which disrupts impedance matching. Strong coupling is desired for uniform current magnitude across the array, maximizing gain; however, over-coupling causes more

pronounced resonance splitting and is avoided.

3.2.2) Capacitive Loading Configuration and Effects

Tunable capacitances are employed to enable scanning in the array, and must be utilized in a manner which minimizes any undesired effects. The primary impact of such loading is on the resonant frequency, since it is well understood that a capacitive loading at the edge of a patch antenna decreases the resonant frequency [30]. This resonance sensitivity is directly related to the location of the loading, as the stored electric energy in the capacitor will depend on the strength of the electric field at the load point. Points with strong electric fields, corresponding to larger voltage swings, prove to be more sensitive. Considering the E-Field distribution underneath the resonant edge of the patch, a point should be chosen to avoid the E-Field null at the midline and maximum at the radiating edge. The varactors used for this antenna array can be either analog or digital, e.g., a digital capacitor bank. This array incorporates Infineon BB857E7902 varactors, with capacitance vs. reverse bias characteristics given in Figure 10.
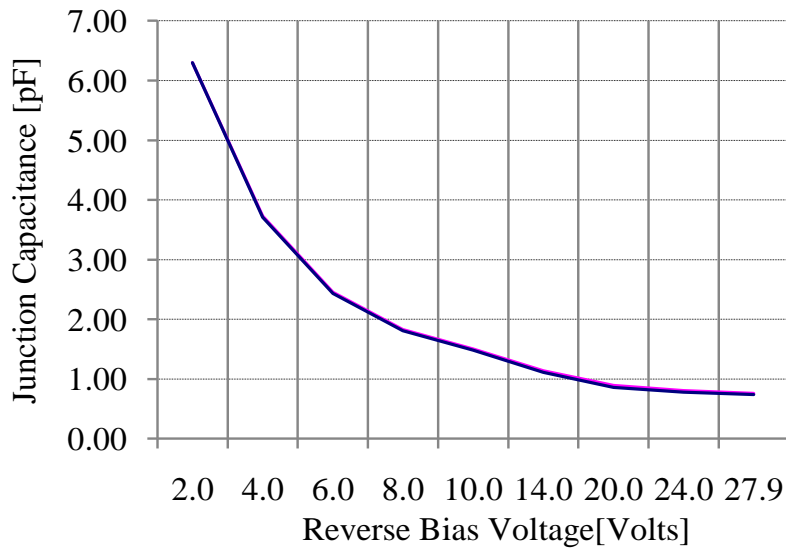
Figure 10: Measured varactor characteristics at 1 GHz.

The horizontal axis of the plot denotes the difference in voltage between the varactor terminals, which is the deciding factor in the junction capacitance of the varactor diode. The capacitance curves for two specimens are shown in the figure, but are indistinguishable due to their identical performance. These components exhibited desirable loss performance at 1 GHz. Characterization was performed by viewing the smith chart input impedance loci of multiple specimens on an Agilent PNA-L N6230A with TRL calibration. The varactors used on the prototype demonstrated excellent consistency across each specimen, and the input impedance loci remained on the outer contour of the smith chart, indicating low loss at 1 GHz.

(a)   C_CPL

The coupling capacitors, C_CPL, are connected to the driven element and the parasitic element, at a location O from the radiating edge, for this purpose. The placement and adjustment of the varactors is chosen to retain symmetry along the non-radiating slot, suppressing cross-polarized radiation. The loading effect of the capacitors is largely sensitive to the location along the resonant length. Loading location is therefore a degree of freedom best utilized to tailor the design to use practically available capacitance values. From Figure 10, it is clear that capacitances on the order of 2.5 pF to 3 pF are near the center of the available capacitance range. To efficiently use the range of the capacitors, the starting bias point of the design is set to achieve resonance in the boresight case with all varactors set to a fixed value in the utilized range. In this design, a starting bias point of 2.6 pF is selected. This value is not critical; the effect of choosing a different starting value for the capacitance would be countered by adjusting the patch lengths and capacitance loading location O.

26
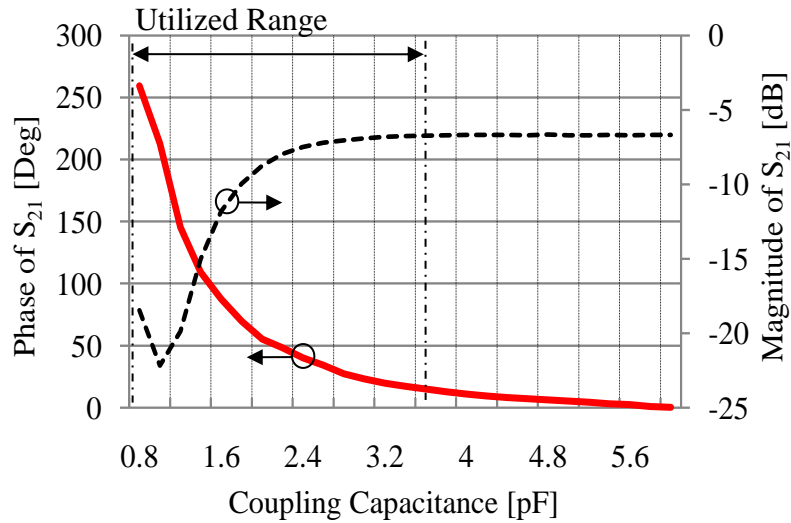
Figure 11: Simulated effects of coupling capacitance on parasitic element current at 1 GHz

Regardless of the exact varactor loading point, the resonance will shift downward; it is then imperative to design the individual resonant radiator to resonate, unloaded, at a higher frequency than the desired array operation frequency.

The coupling capacitors are the primary contributors to the phase shift between the parasitically-coupled antennas. To demonstrate this, a simulation of the structure in Figure 9 was performed with static value capacitors of 2.6 pF everywhere. Ports were defined at the parasitic element microstrip lines to facilitate data extraction. The coupling capacitance between the driven element and a parasitic element was scanned, with the effect on induced current, in both magnitude and phase, documented in Figure 11. Note that Figure 11 is not used as a design curve as the transmission line and coupling aperture effects are not removed. It is likewise noted that the region of sensitivity will shift as the other loads in the structure are varied, but the trends seen are characteristic.

(b)   C_CMP

As the coupling capacitors are adjusted, the resonance of the structure will shift as discussed in Chapter 2. In order to allow variations of the coupling capacitance while maintaining the same operation frequency, grounded compensation varactors, C_CMP, are placed along the exterior edges of each patch. These varactors directly affect the parasitic patch resonant frequencies. The result is the ability to retain a well-matched resonance at the operation frequency which would have been otherwise disrupted. Scanning in this array is achieved through active control of the mutual coupling between the patches which is primarily impacted by the coupling capacitance. Therefore, the compensation varactors are a critical mechanism for maintaining impedance match across the scan range.

3.2.3) Parasitic Element Open-circuited Tuning Stubs

An ideal varactor would exhibit no loss, and cover an infinite range of capacitance values. Unfortunately, commercially-available varactors may have a tuning ratio as large as 10:1, which is far from infinite. Further, the non-zero inductance at the chip leads will cause the device to exhibit self-resonance, possibly further limiting the useful range of capacitance. Therefore, open-circuited microstrip stubs are included underneath the parasitic elements to provide an additional degree of freedom in the design, limiting the necessary varactor capacitance range. By varying the length of these stubs, the phases of the induced currents on the parasitic elements are adjusted, by manipulating the termination impedance ZT, given by

$$Z_T = -jZ_0 \cot(\beta l). \tag{5}$$
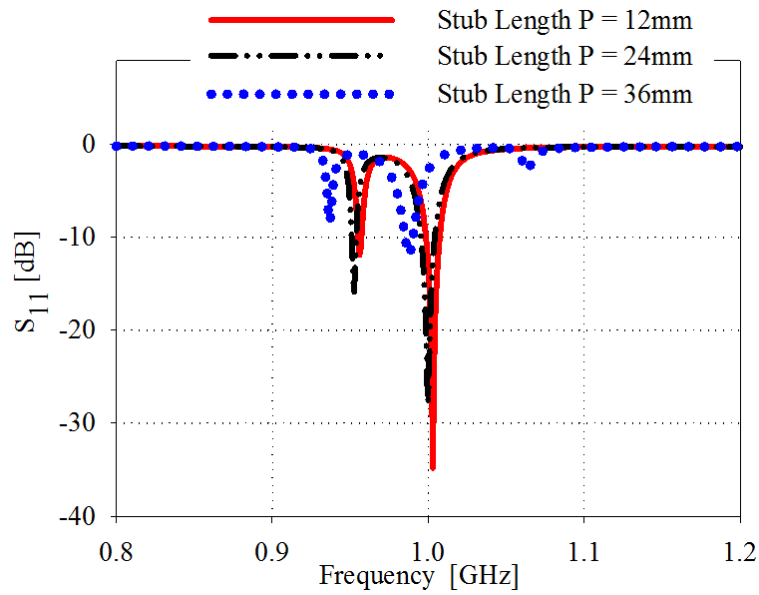
Figure 12: Tuning stub effect on resonance.
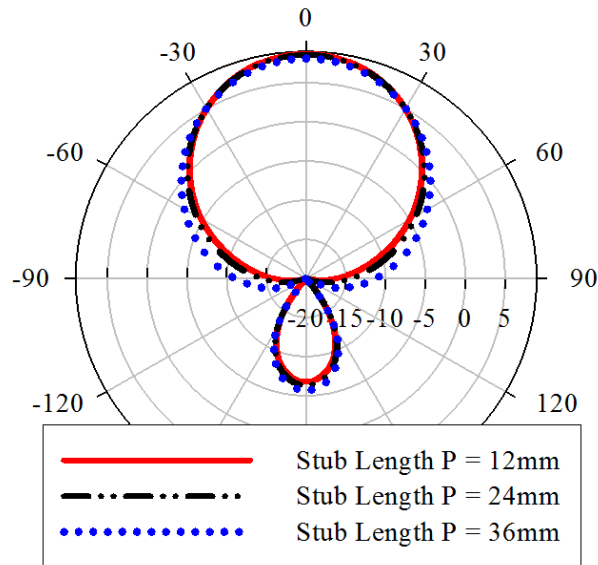
Figure 13: Tuning stub effect on directivity variation.

The effects of the tuning stub length on resonance behavior and array directivity are shown in Figure 12 and Figure 13, respectively, with the loading capacitors held constant at 2.6 pF. The relative separation between resonances stays nearly constant across a large stub length variation, while the center frequency of the resonances shifts due to the additional energy storage

capacity introduced by the microstrip resonator. In this manner, it is clear that the stubs provide a similar function to the compensation varactors *C_CMP*. The coupling level and relative induced current phases are also altered by the presence of these stubs. This effect is manifested in a varying directivity as shown in Figure 13. The magnitude and phase of the induced current changes, resulting in the variations of the directivity patterns. The exact length of the stubs are finalized in the simulation phase.

3.2.4) Array Factor Interpretation

The scanning ability of the parasitic phased array depends on the ability to manipulate the magnitude and phase of the induced parasitic currents. Let I_1 be the current on the driven element, and I_2 and I_3 are the vectors corresponding to the induced parasitic currents. The total radiation pattern will be the multiplication of a single patch antenna hemispherical pattern with the summed vector array factor, *AF*, given by

$$Array\ Factor = \sum_{i=1}^{3} \left|\frac{I_i}{I_1}\right| e^{j\left(kd_i*cos\theta+ang\left(\frac{I_i}{I_1}\right)\right)}. \tag{6}$$

The parasitic radiator current has been expressed conveniently in [31] as a ratio to the driven element current using Z-Parameters. This approach utilizes a rewritten Z Matrix, where the voltages at the parasitic ports are replaced by the currents at the ports multiplied by their respective load impedances. Letting Z_{T2} and Z_{T3} equal the terminal loading impedances, the Z-Matrix becomes

$$\begin{bmatrix} V_1 \\ -I_2 Z_{T2} \\ -I_3 Z_{T3} \end{bmatrix} = \begin{bmatrix} Z_{11} & Z_{12} & Z_{13} \\ Z_{21} & Z_{22} & Z_{23} \\ Z_{31} & Z_{32} & Z_{33} \end{bmatrix} \begin{bmatrix} I_1 \\ I_2 \\ I_3 \end{bmatrix}. \tag{7}$$

For the 3-element patch ESPAR, this matrix yields the following expression, applied at the terminals of the radiators (8):

$$\frac{I_2}{I_1} = \frac{Z_{21}(-Z_{T3}-Z_{33})+Z_{32}Z_{31}}{(Z_{T2}+Z_{22})(Z_{32}+Z_{33})-Z_{32}^2} \qquad (8)$$

Z_T in (8) are controllable mechanisms, and represents the impedance at the parasitic port due to the termination impedance. These are the selected tuning points for previous iterations of the ESPAR. It is clear that adjusting the value Z_T will also impact the magnitude of the parasitic current [25]. More importantly, the limited range of Z_T for a tunable capacitive load can make it impossible to achieve both positive and negative phase values.

The solution, presented for the first time in this work, is a combination of judicious termination and an additional degree of freedom in controlling the parasitic coupling. Therefore, the open-circuited tuning stubs are utilized to present Z_T, which is static after the design phase, while scanning is achieved through active adjustment of Z_{21} and Z_{31} *in situ* (Z_{12} and Z_{13} are consequently identically adjusted due to reciprocity):

$$Z_{21}^L = Z_{21}^U + F\{C\_CPL, \omega\}. \qquad (9)$$

Tunable coupling capacitors C_CPL are connected between the adjacent patches to maintain the magnitude of induced current on the passive radiator while providing the sufficient phase shifting mechanism. The loaded coupling term, $Z_{21}{}^L$, is altered to consist of the unloaded $Z_{21}{}^U$ and an additional corrective term due to the coupling capacitor. This formulation is general, but is descriptive of the effects on coupling levels and phase effects from the coupling capacitance variation.

31

3.2.5) Nondisruptive DC Biasing

DC biasing is required to provide the appropriate voltage differences for the reverse-biased diode varactors. The discrete bias voltages controlling the varactors, V_1-V_5, are visible in Figure 6. These voltages are supplied by small diameter wires passed through vias in the dielectric layers and ground plane, and are directly connected to DC power supplies. The compensation varactor quarter-wavelength radial grounding stubs are visible in Figure 9 (b), as are the small holes for the bias wires. A wire of 0.5-mm diameter connects from the surface of the patch to power supply lines on the feed layer, passing through a hole in the ground plane. These wires terminate at the short-circuit position of quarter-wavelength radial stubs on the feed layer, which is also the connection point of the DC bias wires. The location of connection to the patch is selected to bisect the patch along its resonant length, at a point where surface current sees a virtual short due to the minimized electric field and maximized current magnitude for the patch's fundamental resonant mode. The resonance and radiation characteristics are preserved, and the DC power supply remains isolated from the RF signal by both the inductance of the small-diameter wire and the existence of an RF virtual short in parallel.

3.3 Full-wave Simulation

3.3.1) Simulation package and configuration

The design illustrated in Figure 6 and Figure 7 was simulated using Ansoft's High Frequency Structure Simulator (HFSS) full-wave solver package. After a single element was designed and simulated at 1.04 GHz, identical parasitic patches were coupled as shown in Figure 6, Figure 7, and Figure 8. The varactors were modeled as idealized lumped components, and were adjusted in unison to tune the resonance for the boresight case to 1.0 GHz. The varactor values were identical for both coupling and compensation positions in this stage to ensure that there were no large discrepancies in loading across any individual patch, which would facilitate cross-polarization problems. The result of this study is the starting bias point of 2.6 pF for all varactors for the boresight case.

The slot dimensions were simultaneously adjusted for each of the patches to minimize return loss. As the varactors were all of the same value and the structure was symmetric, the generated pattern was symmetric and no scanning was exhibited. Finally, the parasitic termination stub lengths were tuned through a parametric sweep to produce optimal coupling characteristics, which increased gain and reduced the half power beamwidth and ensuring no grating lobes. To achieve beam scanning, the symmetry of the design is altered by adjusting the capacitances loading the structure in a non-symmetric fashion. For the beam scans, the coupling capacitors for each parasitic element are adjusted from their nominal value to alter the mutual coupling characteristics. As this typically alters the structure's resonant frequency, the

compensation varactors are then tuned to bring the resonance back to the desired operation frequency of 1 GHz.

3.3.2) Simulation results

Five simulated configurations are presented in Table 1, and the simulated results for critical scan configurations are displayed graphically in Figure 14 and Figure 15. These scanning schemes are chosen to show that the scanning performance of the patch ESPAR is continuous both in range and pattern integrity, with exhibited beam maxima at regular intervals across positive and negative scan angles. It is noted that as the structure is symmetric, values of the parasitic element varactors are interchanged to produce a radiation pattern mirrored in the H-plane and identical resonant behavior.

Table 1: Simulated Results of 3-Element Dual-Layer Patch ESPAR

(All Values Given at 1 GHz)

Scan Angle [deg]	Loading Schemes and Gain Characteristics				
	Peak Gain [dBi]	*CPL_1 [pF]*	*CPL_2 [pF]*	*CMP_1 [pF]*	*CMP_2 [pF]*
-15	6.9	3.0	1.5	3.5	0.8
-7	7.5	2.9	1.7	3.2	1.1
0	7.5	2.6	2.6	2.6	2.6
7	7.5	1.7	2.9	1.1	3.2
15	6.9	1.5	3.0	0.8	3.5

The return loss is maintained at the operation frequency to better than 15 dB for all cases. Furthermore, it is clear that the scanning is achieved without sacrificing pattern integrity. Side lobes are not present.
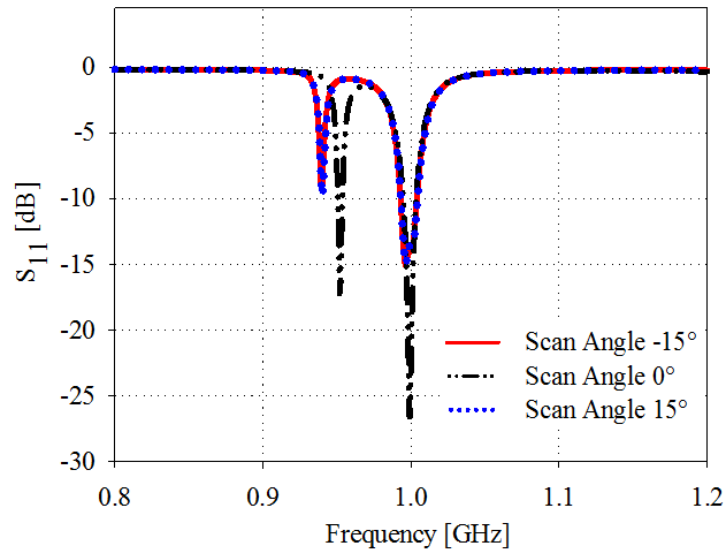
Figure 14: Simulated performance of S11 vs. frequency.
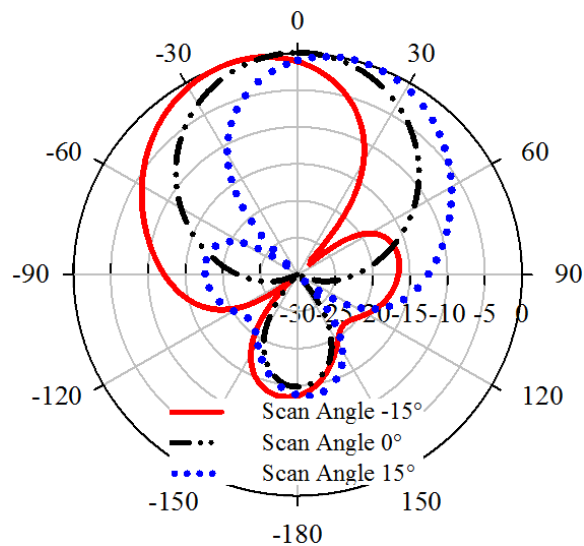
Figure 15: Simulated radiation patterns for multiple scan cases.

The half-power beamwidth of 56° at boresight does not increase at the extremes of the scan range as would be expected in a traditional design; rather, the HPBW decreases to 54°. This is a result of the non-uniform, varying current magnitude for different scan angles. The gain variation is around one half decibel across the range. Sensitivity analysis was performed by adjusting the values of the coupling and compensation varactors and recording the performance degradation. It was found that bias voltage fluctuations of up to 10% did not cause adverse performance effects. This is due to the utilization of the varactors in the range where capacitance does not change sharply with voltage, as seen in Figure 10. Additionally, the varactor load points were carefully selected to avoid such sensitivity, by choosing a location away from the radiating edge. Coupling resonant structures, such as the patch antennas used here, results in resonance splitting. This phenomenon can be most easily viewed in terms of multiple nulls in the S11 response in Figure 14 around the operation frequency, and becomes apparent in the design simulation results.

3.4 Comparison to traditional array with N=3

The comparison of this patch ESPAR and a traditional 3-element patch array employing phase shifters is necessary to understand the differences and advantages of our approach. A traditional phased array uses element spacings of, at maximum, one half-wavelength to minimize mutual coupling effects while preventing grating lobe formation. The elements are fed with identical magnitudes and a linear phase gradient which is dependent on the desired scan angle. Previous patch ESPAR designs have shown that mutual coupling is an essential mechanism for

beam scanning without phase shifters, and the element spacings are necessarily smaller [16, 17]. The same trend of closely-spaced elements is seen in the proposed arrays.

To better demonstrate the effects of the proposed loading technique, the ESPAR is compared to a 3-element array with element widths and spacings identical to those given in Figure 9, and lengths of 95.5 mm, corresponding to resonance at 1 GHz. This array is fed in the traditional method, with phase shifters controlling the excitation of each element. A simulation was constructed with these dimensions, but without capacitors, and each antenna was fed with a wave port. This allowed the magnitude and phase for each element to be controlled from the excitations. The patch antennas are coupled at a gap of 3 mm, which correspondingly facilitates a large coupling level. This fact is clearly seen in Figure 16 (a), where S11 for the traditional array is compared to that of the simulated patch ESPAR. While a single patch antenna had been matched to better than 15 dB, the presence of closely spaced neighboring elements has worsened the return loss to approximately 7 dB at the operating frequency. Obviously, it would be necessary to either reduce the coupling or introduce a matching network. The patch ESPAR does not have this issue. Due to the careful manipulation of the compensation varactors, the resonance characteristics have been maintained for suitable return loss. Figure 16 (b) and Figure 17 compare the patterns and peak gains for each array type, respectively, which were generated by manipulating the relative phases. The patterns of the proposed ESPAR maintain good shape and gain across scan, which had not been previously demonstrated in a continuous scan range ESPAR.
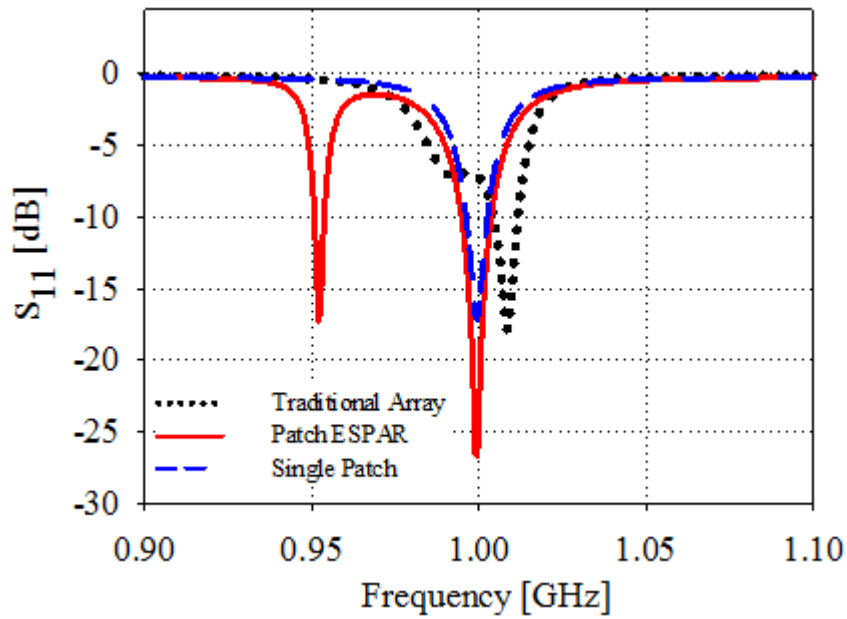
(a)
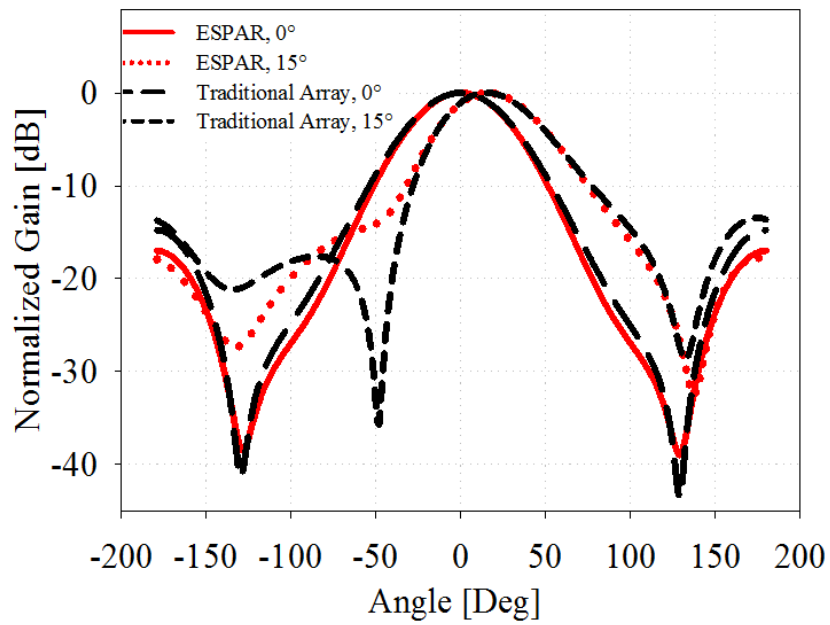
(b)

Figure 16: Comparison of traditional array and patch ESPAR simulations. (a) Input impedance matching. (b) Normalized pattern comparison.
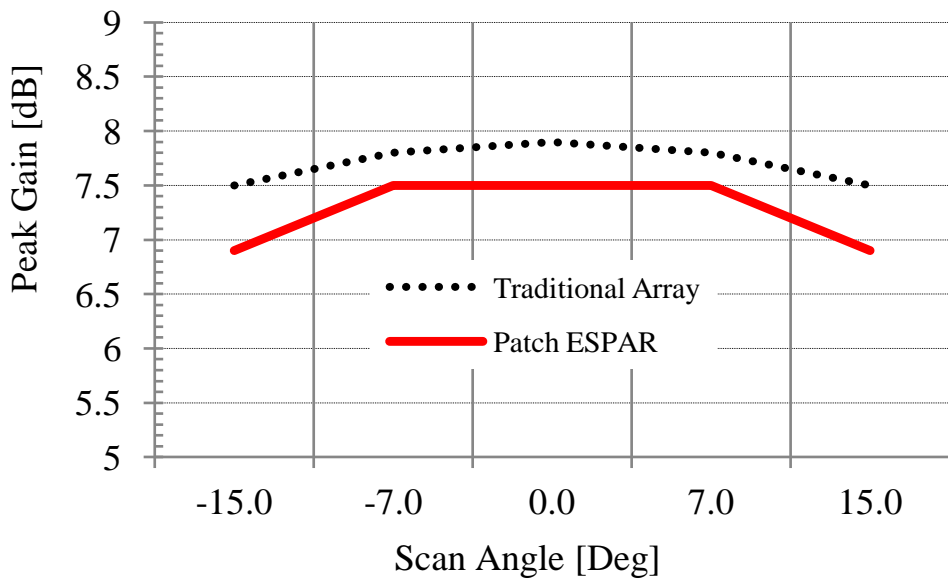
Figure 17: Simulated gain vs. scan angle for patch ESPAR and uniformly-illuminated patch array

While a uniform cumulative phase distribution is utilized for maximized gain in the traditional array, the patch ESPAR phases are not a uniform distribution. Figure 16 (b) compares the radiation patterns versus scan angle for the patch ESPAR and the traditional patch array. It is noted that due to the magnitude tapering across the ESPAR, the side lobes are inherently lower than the uniform distribution side lobes. Figure 17 records the gain variation versus scan angle for the compared topologies, which is quite similar save for a small (roughly 0.5 dB) offset in maximum gain, due to amplitude tapering in the patch ESPAR. Additionally, coupling level varies slightly through the scanning configurations. This results in a lower gain than the traditional case.

In Figure 18, current phase distribution for the boresight scan angle case is presented for each array type. It is clear that while there is no phase variation for the traditional array, the patch ESPAR has a small, symmetric phase variation across the elements. Figure 19 and Figure 20 likewise exhibit the phase variations for scanning to 7° and 15°. For the traditional array, the phase variations are linear progressions with a slope that increases with scan angle. The patch ESPAR does not exhibit linear phase progressions; rather, the variations are of the same trend, but non-linear.
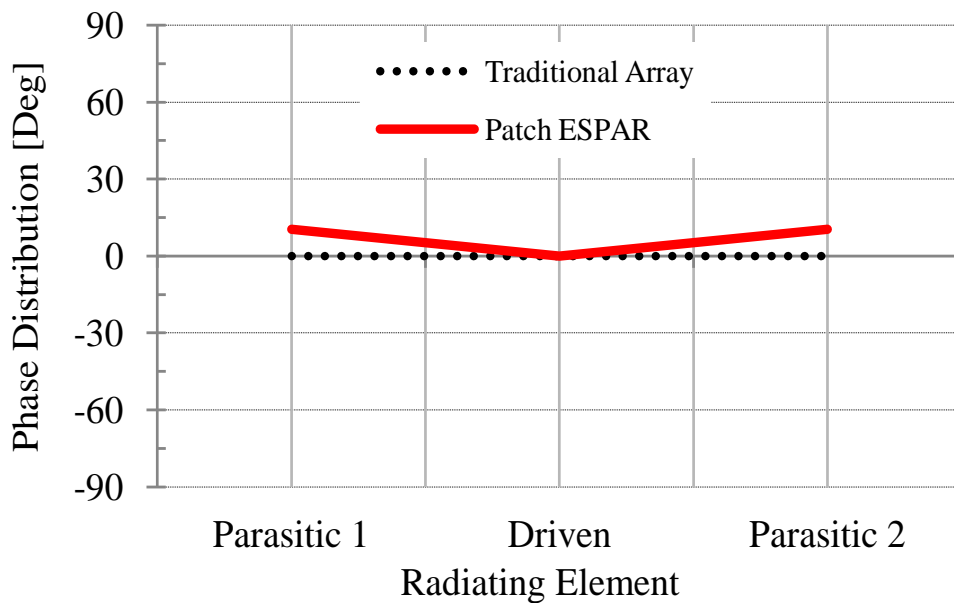
Figure 18: Element current phase comparison at boresight.

The parasitic current magnitude is also different from the traditional array, where the magnitudes of all elements are identical. This behavior is evident in Figure 21. The resulting patterns for the patch ESPAR have their maxima coincident with the traditional array, indicating similar scanning performance at the cost of a small amount of gain.
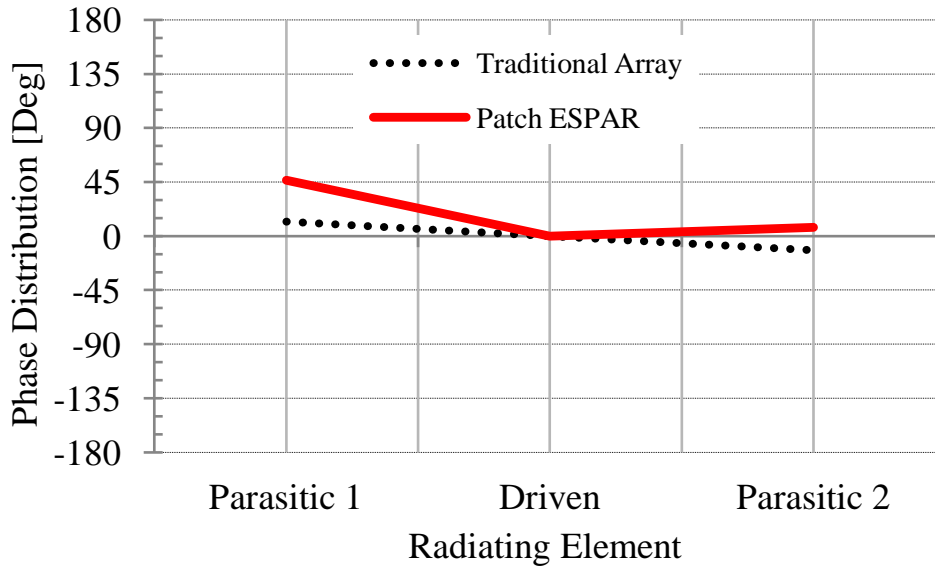
Figure 19: Element current comparison for scan angle 7 degrees.
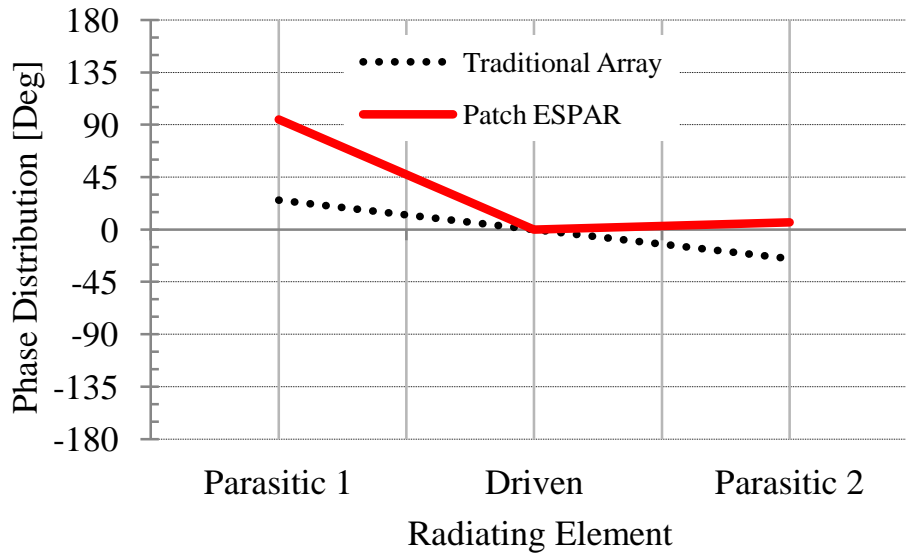
Figure 20: Element current comparison for scan angle 15 degrees

This non-ideal but fully functional compromise gives the patch ESPAR its advantage in cost. It is clear that the induced current levels and phases are being controlled by the reactance variations.
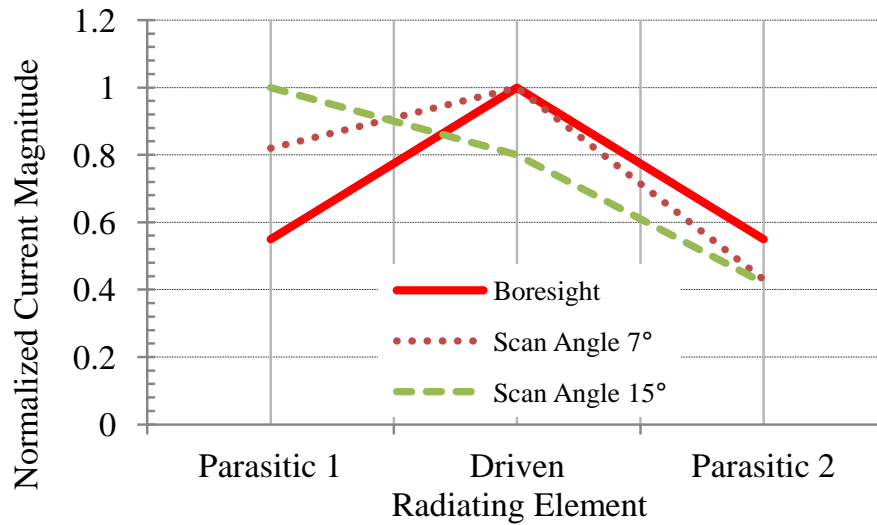
Figure 21: Normalized ESPAR current magnitude distribution vs.scan angle.

3.5 Fabrication, Measurement, and Results

3.5.1) Fabrication Technique

A prototype of this array was fabricated and measured. The fine features of the antenna and feed layers were milled out by an LPKF ProtoMat S100 milling machine, including drilled via holes, with the majority of extraneous copper removed by etching. Concentric apertures were milled out from the ground planes of each layer, and those ground planes were coated in a thin layer of solder. The individual layers were aligned, clamped together, and bonded with a layer of tin solder by heating in a reflow oven. Finally, the Infineon BB857E7902 chip varactors were mounted and soldered. Figure 22 illustrates the fabricated patch layer. The patch elements are labeled, and the varactors pads and biasing vias are visible on the parasitic element exterior edges. Small pads for the surface mount chips are visible in the inter-element gap.

42
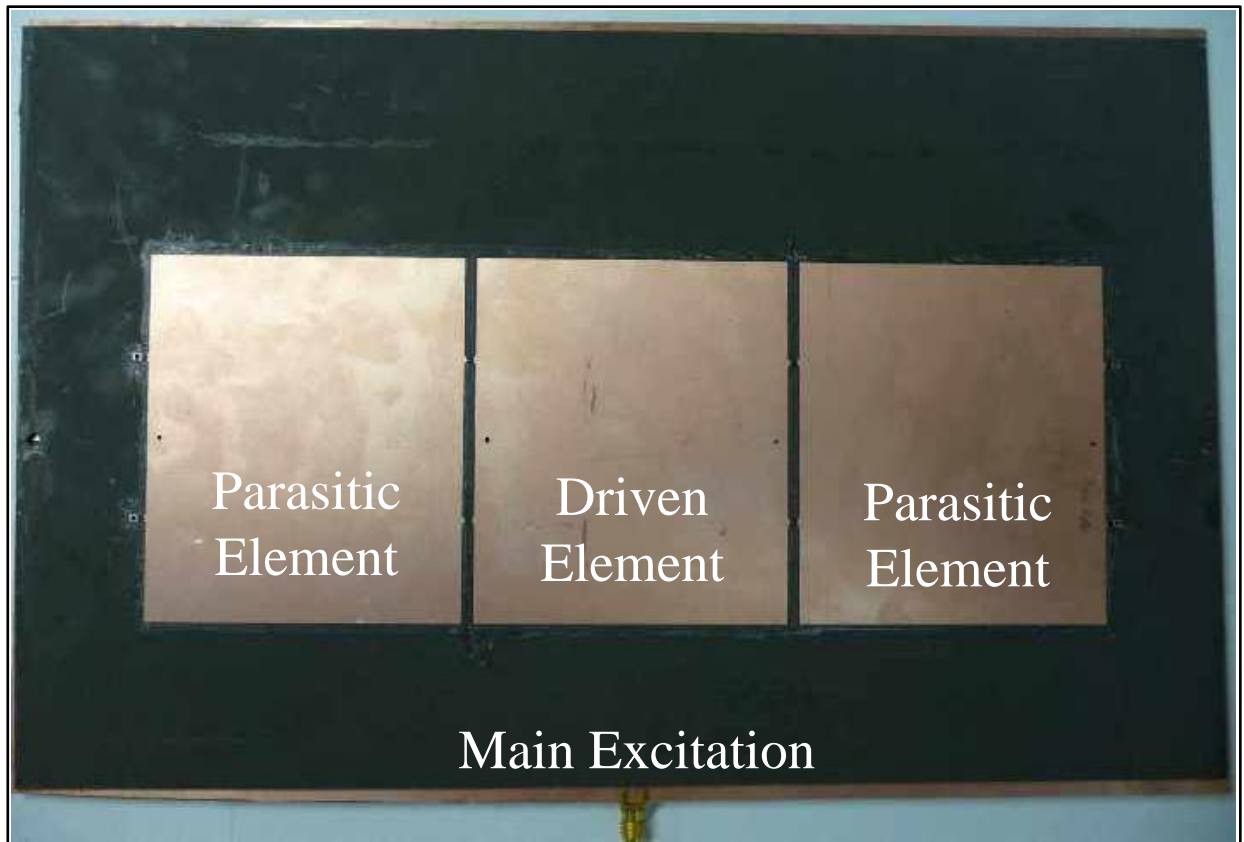
Figure 22: Photos of the array prototype patch layer with varactors.

Some scoring in the dielectric near the patch edges is apparent and is due to the depth of the milling machine bit.

Figure 23 shows the feed layer, composed of the driven microstrip, DC bias via holes, tuning stubs and ground stubs. The coupling varactors and bias pin are shown in Figure 24, while Figure 25 illustrates the mounted device and the biasing during measurement, respectively. The wires, which are visible in the photo, were carefully grouped and restrained as to not become stuck during pattern measurement. Care was taken to seal the access points where the wires breached the anechoic chamber shielding.
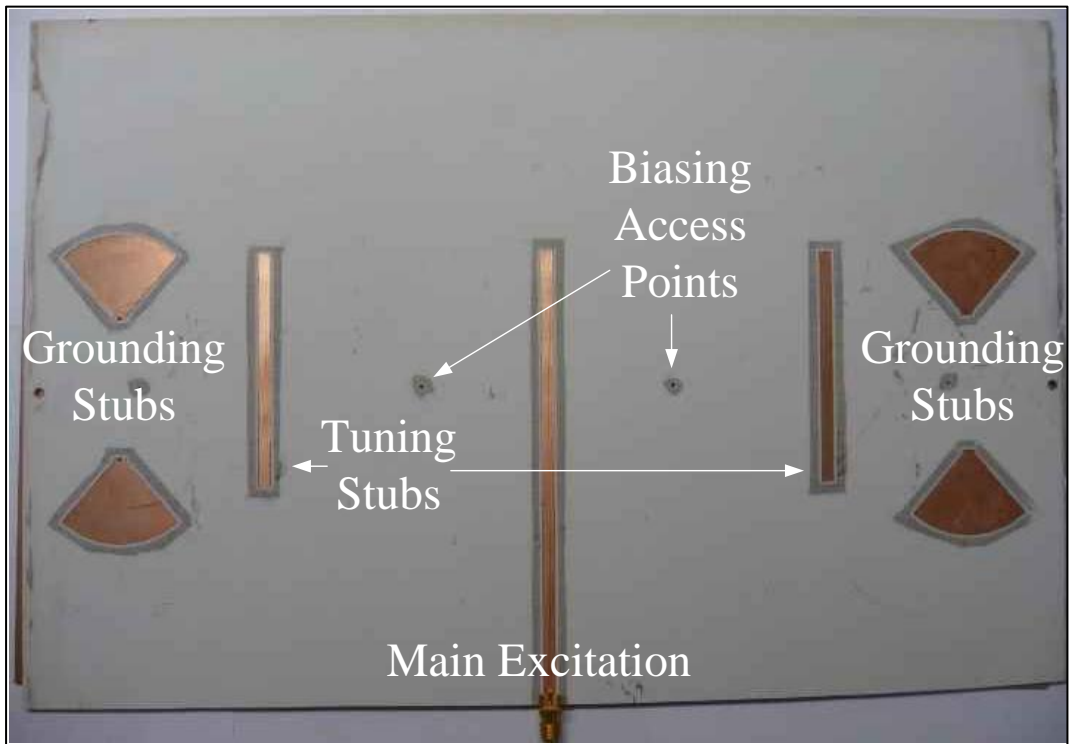
Figure 23: Photo of the array prototype feed layer.
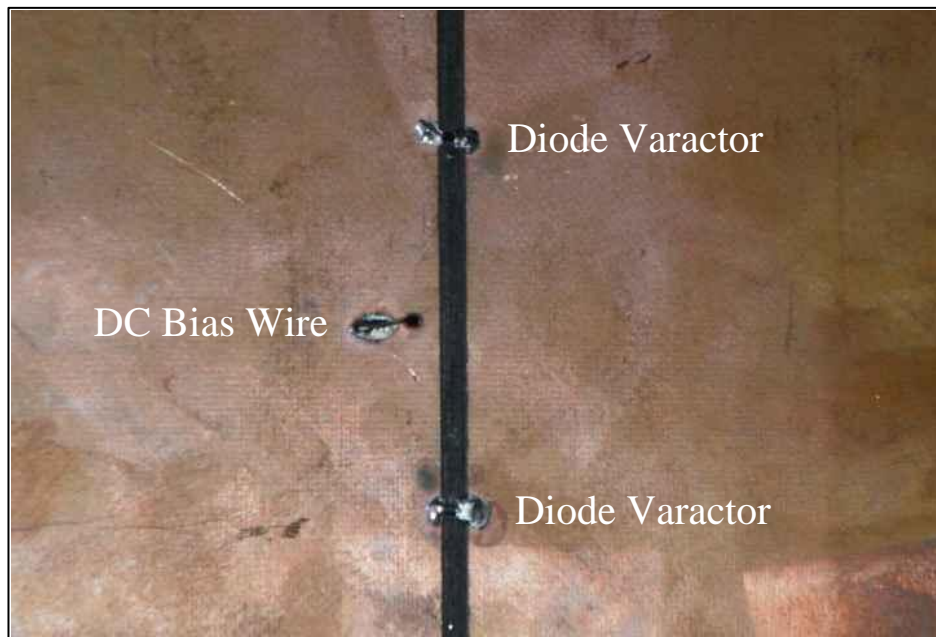
Figure 24: Photo of the surface mount diode varactors and biasing vias.
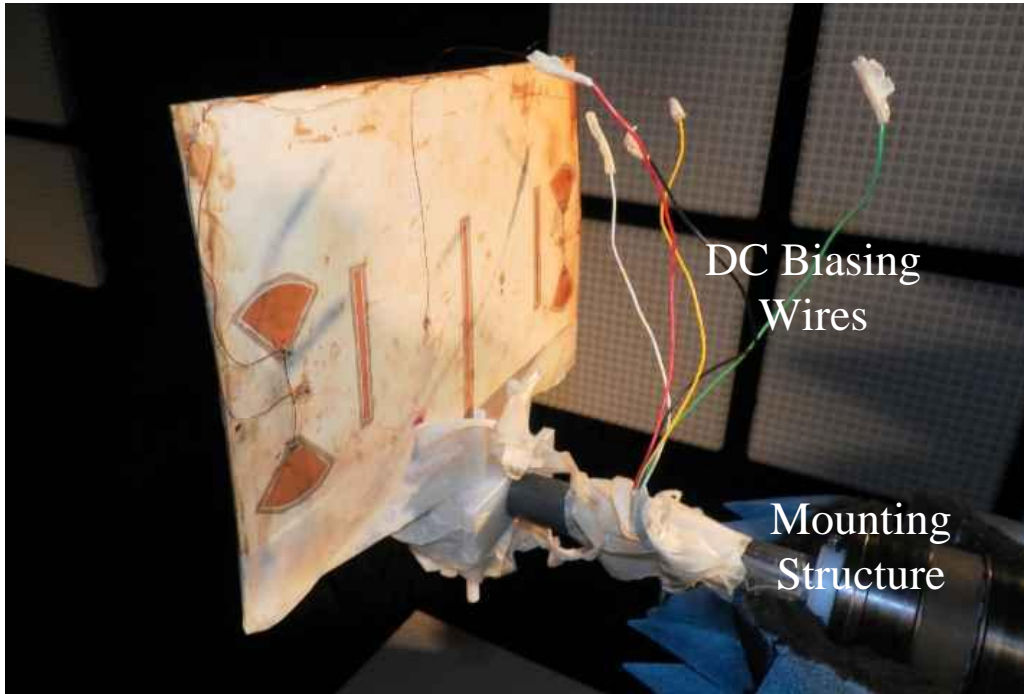
Figure 25: Photo of the mounted prototype during measurement.

3.5.2) Array Radiation Pattern Results

The antenna was measured in an anechoic chamber under biasing schemes corresponding to the simulation cases. Gain measurement is shown in Figure 26 and Figure 27. The gain of the patch ESPAR was measured in an anechoic chamber. The varactors were biased according to the boresight case and S_{21} measurements were made utilizing the ESPAR and two standard gain horn antennas at the operation frequency. Calculation of the gain after accounting for free space loss and comparing to a standard gain horn yielded a total gain of 7.4 dB at 1 GHz, which is .1 dB less than the simulated gain. The bias voltages were adjusted according to Figure 10 to achieve the loading configurations for the scanning cases from Table 1. The gain at the maximum scan angle of 15° degrees was computed to be 6.5 dB, corresponding to a total gain variation of 0.9

dB across the scanning range, as shown in Figure 27. This decline in gain is attributed to the combination of a reduction in magnitude of the individual patch element factor in this region. The half power beamwidth for the array is 56° in the H-Plane, with E-Plane patterns identical to those of the single patch.
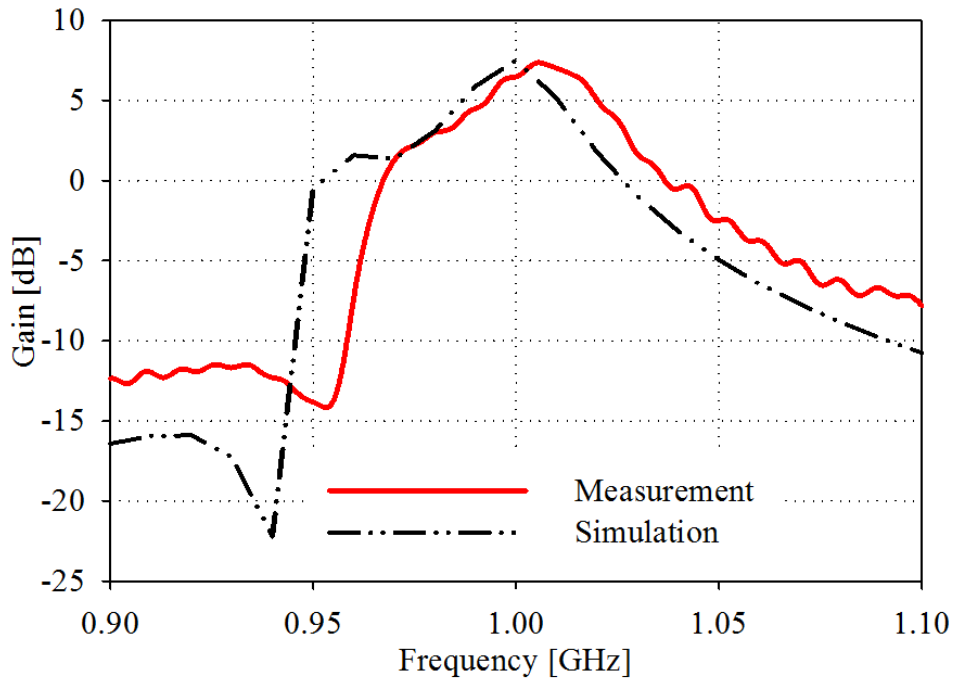
Figure 26: Gain vs. frequency at boresight.

The resonance behavior is displayed in Figure 28, and closely matches the trends of the simulated case, with a 0.5% center resonance shift due to fabrication tolerances. However, the slight shifts in the resonance behavior introduces the additional phase shift over the simulation case, resulting in the beam squint error of 5°, and the introduction of side lobes which are absent in simulation.
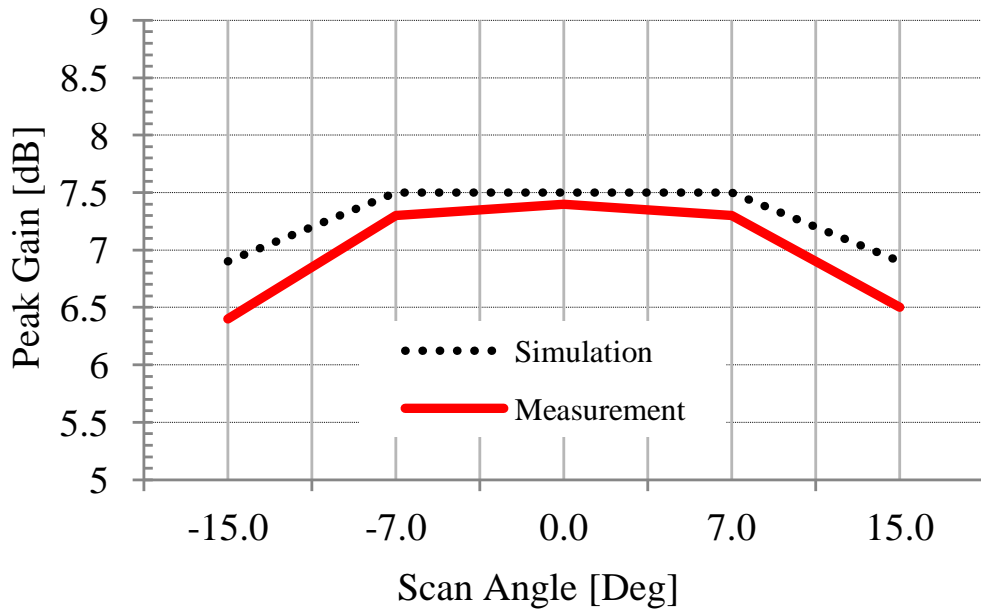
Figure 27: Gain vs. scan angle at 1 GHz.

The main mechanisms for this frequency shift are the combined effects of slightly altered dielectric permittivity of the patch substrate, and deviation in the varactors from their expected value. This can be due to biasing voltage error, but is most likely due to simple variations from batch to batch during the varactors fabrication.

(a) -15o. (b) -7 o. (c) 0 o. (d) 7 o. (e) 15 o.
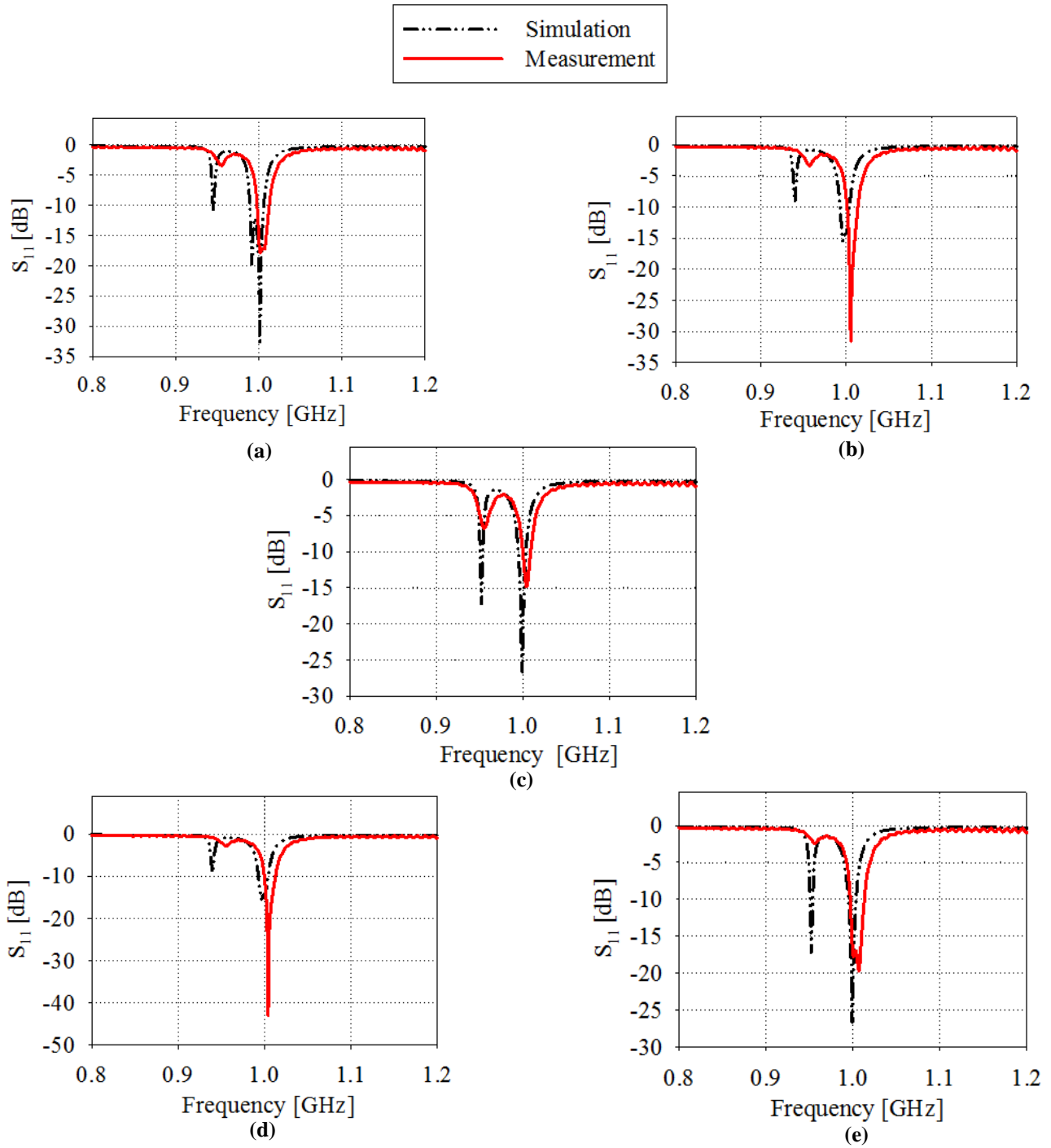
Figure 28: Simulated and measured normalized scattering parameters for different scan angles.

48

The resulting radiation patterns are displayed in Figure 29. The simulations and measured patterns match closely, with exhibited symmetric scanning from -20° to 20°. The patterns are narrow and match the simulated patterns very well. There is an offset of 5° in the -15° and 15° cases. This is attributed to the altered resonant behavior due to fabrication tolerance. While the varactors are unable to be measured after incorporation with the prototype, their prior characterization and precise voltage control during the measurement yield high confidence in the values stated here.

The efficiency of the patch ESPAR exceeds that of a traditional array, with a calculated efficiency of 79.1%. The efficiency was calculated using the common method where measured peak gain is divided by simulated directivity, and therefore includes the varactor diode losses. This efficiency monotonically decreases away from 1 GHz, as expected. The patch ESPAR is more efficient than its traditional analogue, due to the elimination of phase shifters, which would exhibit loss. To demonstrate, a three element patch antenna array was simulated. The patches were spaced similarly to the proposed array, but were thinner, as to enlarge the inter-element gap and reduce mutual coupling. The efficiency of this patch array was 79.7%. Inclusion of 0.5 dB insertion loss phase shifters for each element would reduce the total efficiency to 71%. The equivalent isotropic radiated power (EIRP) of the patch ESPAR would inherently be higher than that of the traditional array using a power splitter and lossy phase shifters, considering the efficiency difference.

(a) -15°. (b) -7 °. (c) 0 °. (d) 7 °. (e) 15 °.
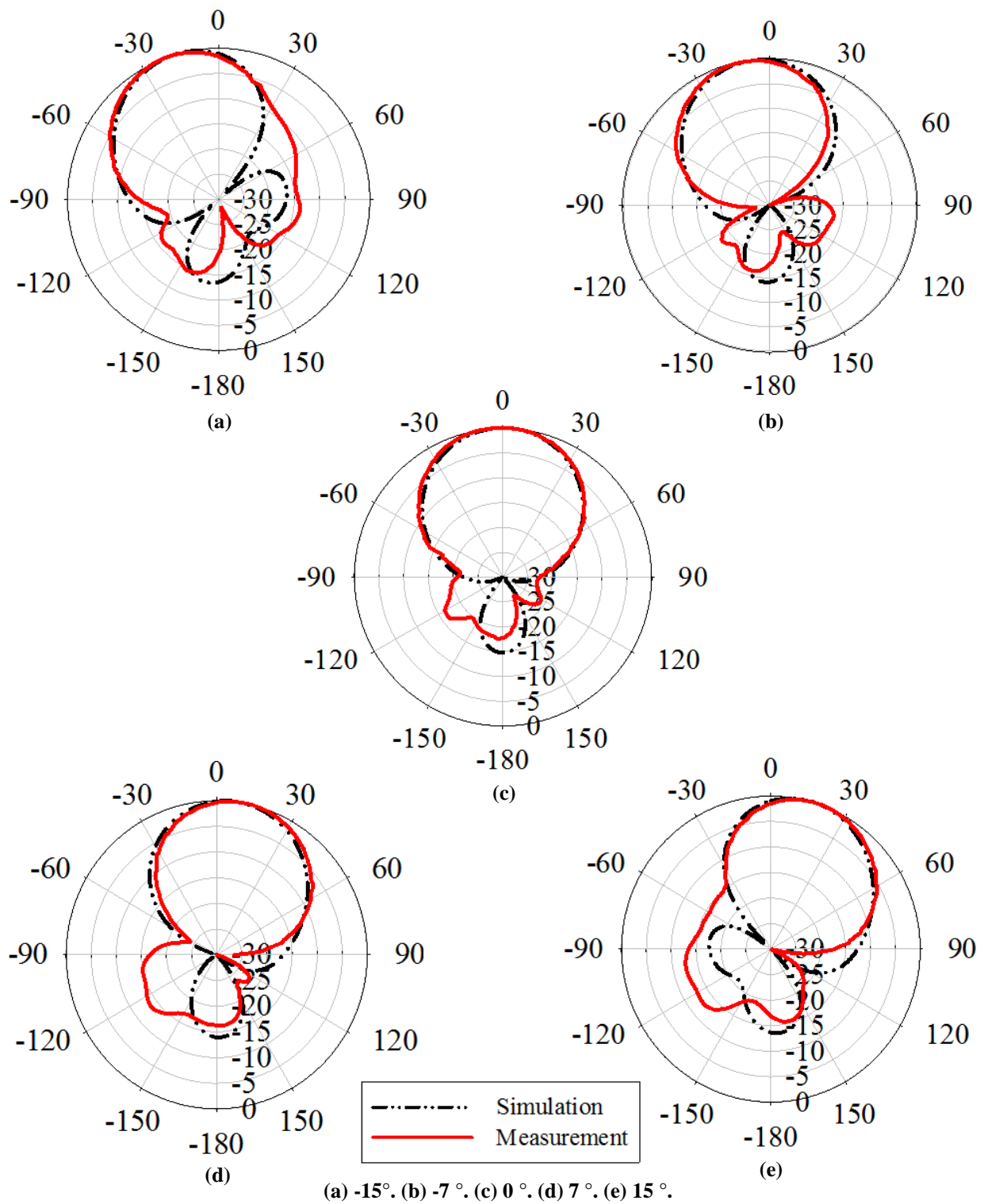
Figure 29: Simulated and measured normalized linear gain patterns for different scanning angles.

3.6 Conclusion and Further Improvements

A novel, inexpensive parasitic phased array antenna has been presented. The approach exhibits ample beam scanning in a measured -15° to 15° range with maintained pattern integrity, no side lobes, and low return loss for all cases. There are no phase shifters in the design and only inexpensive, commercially-available diode varactors were employed. The structure was fabricated and measured, and its performance was accurately predicted by theory and simulation.

The general form of the presented patch ESPAR will be improved upon in the forthcoming chapters, which will increase directivity and gain while reducing beamwidth and enhancing fabrication reliability. Elimination of both the feed layer and the open-circuited tuning stubs are desired, as the stubs may be made obsolete by appropriate adjustment to the parasitic element size. This array will be incorporated as a unit cell in a linear or planar array as part of future work. Due to the ability to scan this 3-element array without phase shifters, it can easily be integrated into a larger array as a unit cell without concern for large side lobes or excessive gain loss while scanning. In this manner, higher directivity and scan range will be achieved, while the pattern will exhibit a much smaller HPBW.

CHAPTER 4: THE 2-ELEMENT ESPAR ARRAY

4.1 Overview

In the preceding chapter, a microstrip patch ESPAR antenna was shown to achieve high gain, efficiency, and maintained impedance match across the scan range. Coupling capacitors were utilized in the inter-element space to control the mutual coupling, while compensation capacitors provided a resonance control mechanism, allowing maintained impedance match versus scan. This chapter further explores this phenomenon along two main avenues.

First, a 2-element ESPAR antenna will be investigated for the first time using the proposed capacitive mutual coupling control mechanism. Previous patch ESPAR iterations have not demonstrated double-sided scanning with a single parasitic radiator, although this is physically possible. This sort of driven/parasitic element pair can easily be inserted in narrowband uniformly-illuminated arrays in place of the single element to enhance directivity and reduce the side-lobe level by actively tailoring the element factor during scans. Second, both two and three-element ESPARs are theoretically studied with graphical illustration of effects on the array factor (AF), which is the first such demonstration for this new topology. Full, double-sided scanning in the H-Plane is simulated for a two-element non-symmetric array at 2.5 GHz.

4.2 Two-element ESPAR Theory and Design

To demonstrate a low-profile and easily fabricated array with high gain, rectangular microstrip patch antennas are chosen as the radiating elements. The patch antennas are coupled at a small distance and are connected to a feed network through apertures in the ground plane. The feed circuits are microstrip lines which are terminated in open-circuits approximately one quarter-wavelength beyond the apertures to facilitate impedance matching. One element is fed by connecting the microstrip line to a signal source. Figure 30 illustrates the array geometry for the two-element ESPAR.
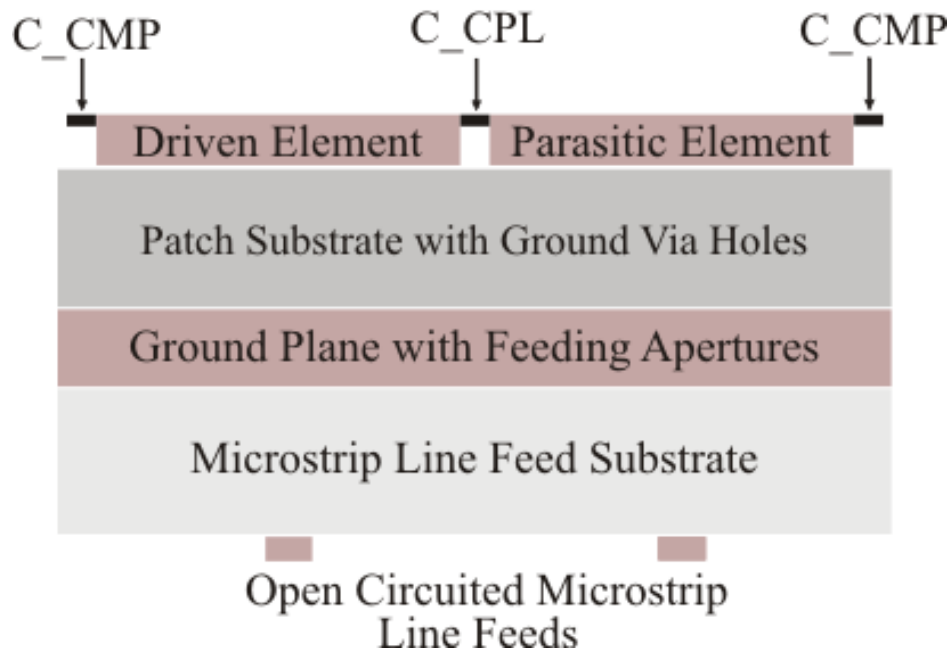
Figure 30: Stacked layer view of the microstrip patch ESPAR.

The antenna dielectric layer consists of 62-mil Rogers RT/Duroid 5880 ($\varepsilon_r = 2.2$, $tan\delta = 0.0009$) substrate, chosen for its low permittivity and low loss factor. The microstrip feed layer is 60-mil Rogers RO4003 ($\varepsilon_r = 3.55$, $tan\delta = 0.0027$) substrate. The parasitic element is terminated

with a matched load to reduce reflections, minimizing sensitivity to fabrication tolerance. The stub acts as a design-phase tuning mechanism which allows for selection of an optimal biasing point for the boresight scanning case.

Control of the phase between the radiators, and the consequent beam scanning, is realized through tunable coupling varactors (C_CPL in Figure 30.) Two varactors are used and are symmetrically placed about the center of the patch at a total separation of half the patch length. This is done to retain symmetry in the E Plane to avoid pattern distortion by asymmetric current variation. The two-element array operation frequency is 2.5 GHz, and the dimensions of the structure are shown in detail in Figure 31.
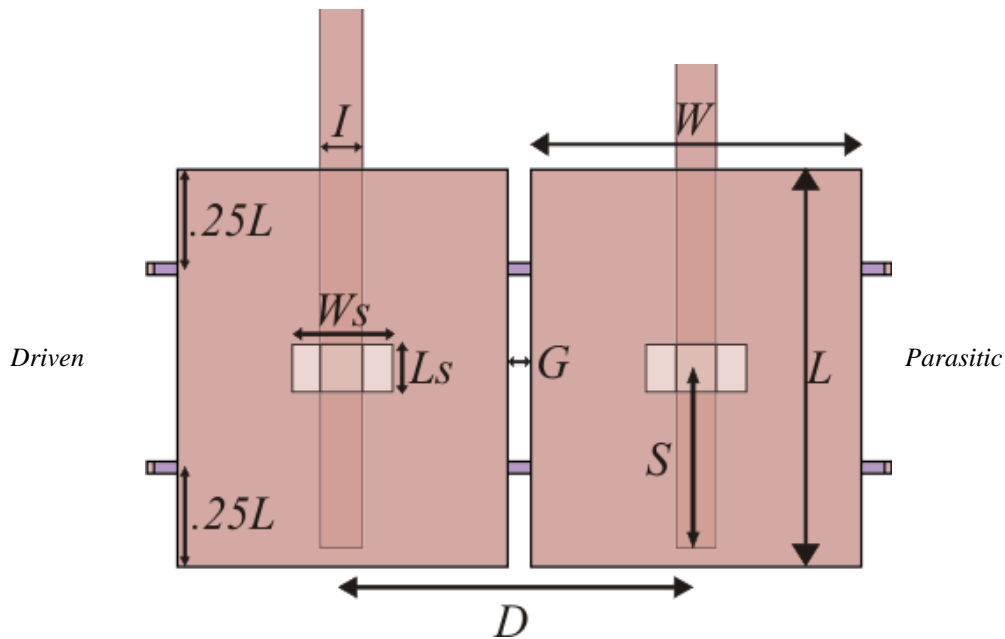
(L = 33, W = 28, D = 30, G = 2, S = 15.2, W_S = 7, L_S = 4.5, I = 3.5). All dimensions in mm.
Figure 31: Dimensions of 2-element ESPAR.

Two identical patches are coupled in the H Plane at a gap distance of 3 mm, and the final structure is not symmetric in the H Plane. This lack of symmetry will present some issues for the

boresight scanning case, and is the main factor in the necessity of the symmetric 3-element array. Maintained impedance match at the operation frequency for all scan angles is uncharacteristic of both traditional phased arrays and previous implementations of ESPAR antennas.

The loading of resonant structures with tunable reactive components is generally associated with resonance shifting [32]. The compensation varactors in the presented ESPAR antennas are a direct counter to this resonance shifting. As the coupling capacitance is tuned to achieve beam scanning, the compensation varactors (C_CMP in Figure 30) are adjusted to maintain stable resonance, resulting in maintained impedance match. Therefore, the beam scanning operation requires appropriate reverse biasing conditions to control both mutual coupling via coupling capacitors and resonance characteristics by the compensation varactors.

To scan the beam formed by a phased array, the inter-element phase differences must be controlled. The fields generated by each radiator are assumed to produce fields with the same radiation pattern. If ports are introduced at the radiating currents on the antennas, S-Parameters may be used to measure the magnitudes and phases of the radiating currents. The array factor (AF) is a useful theoretical tool which illustrates the effect of superimposing these generated fields which ultimately results in the beam scanning. Given that the S-Parameters at the 'n' radiators are available via simulation or calculation, the AF is calculated by

$$AF = 1 + \sum_{i=2}^{n} \left|\frac{I_i}{I_1}\right| e^{j[kd_i \cos(\theta)+\beta_i]}, \tag{10}$$

where

$$\beta_i = \arg(S_{i,1}). \tag{11}$$

55

Therefore, it is possible to plot the array factor if the relative phase and magnitude of the radiating currents are known. To this end, we employ full-wave electromagnetic simulation for specific loading schemes.

4.3 Full-wave Simulation

Simulation of the two-element array was performed for multiple loading schemes in Ansoft High Frequency Structure Simulator (HFSS). A wave port was utilized to feed the driven element, and the structure was meshed and solved at 2.5 GHz. The complex electric fields at corresponding points inside the radiating slots of each rectangular patch antenna were extracted. For a two-element array with the surface normal along the positive Z direction, the phase and magnitude of the radiated fields, respectively, are given by the expressions

$$\beta_2 = \tan^{-1}\left(\frac{\text{Im}\{E_{Z2}\}}{\text{Re}\{E_{Z2}\}}\right) - \tan^{-1}\left(\frac{\text{Im}\{E_{Z1}\}}{\text{Re}\{E_{Z1}\}}\right), \tag{12}$$

$$\left|\frac{I_2}{I_1}\right| = \frac{|E_{Z2}|}{|E_{Z1}|}. \tag{13}$$

Equations (12) and (13) were calculated for the E_Z values extracted from simulation, and the results were substituted into equations (10) and (11). The array factor calculations for three loading cases are shown in Figure 32.
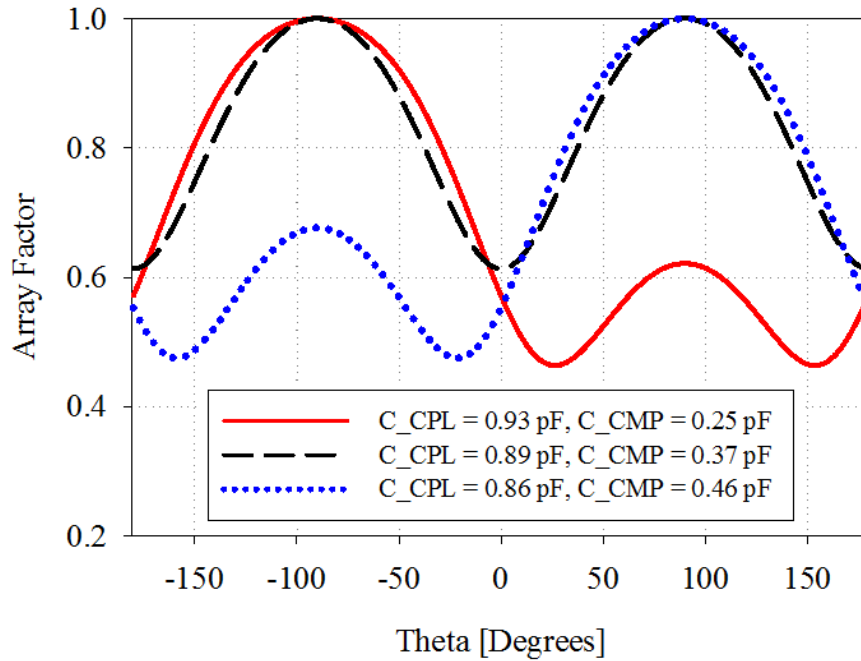
Figure 32: Calculated 2-element ESPAR array factor for various loading cases.

Lumped element capacitors were placed at the corresponding locations of the coupling and compensation varactors. After solving, the values of the coupling and compensation varactors are adjusted to control the mutual coupling and consequent beam scanning. Similarly, the structure was solved from 2.4 to 2.6 GHz with radiation patterns plotted for different scanning cases. The radiation patterns at 2.5 GHz and S_{11} are plotted in Fig. 4 (a) and (b), respectively. It is noted that the boresight scanned pattern corresponds to an array factor with a null at boresight. This is due to the patches resonating roughly π out of phase; the lack of symmetry in the design is counter-productive to exciting an even mode field distribution with broadside radiation. This concern is the driving factor in exploration of the symmetric 3-element ESPAR antenna.
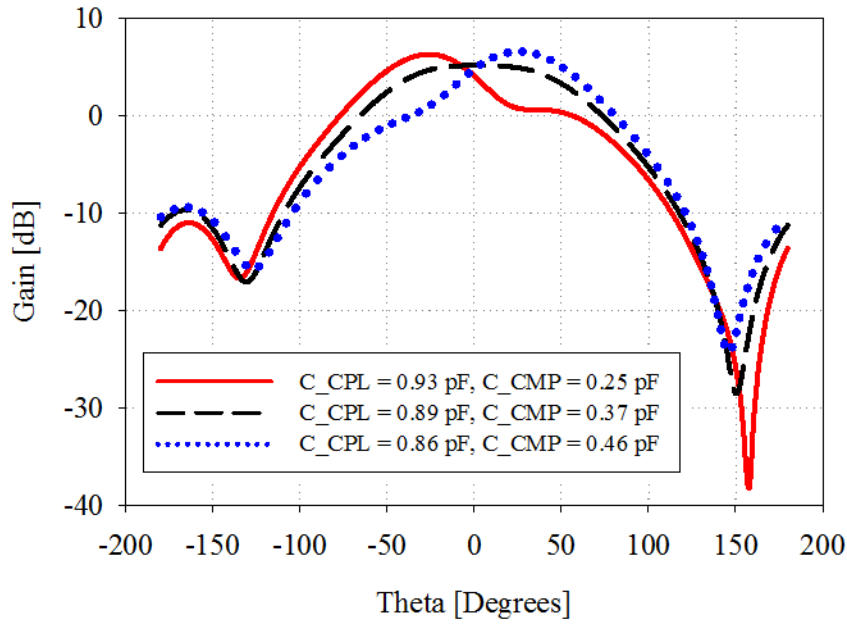
Figure 33: Simulated gain patterns of the two-element ESPAR antenna.
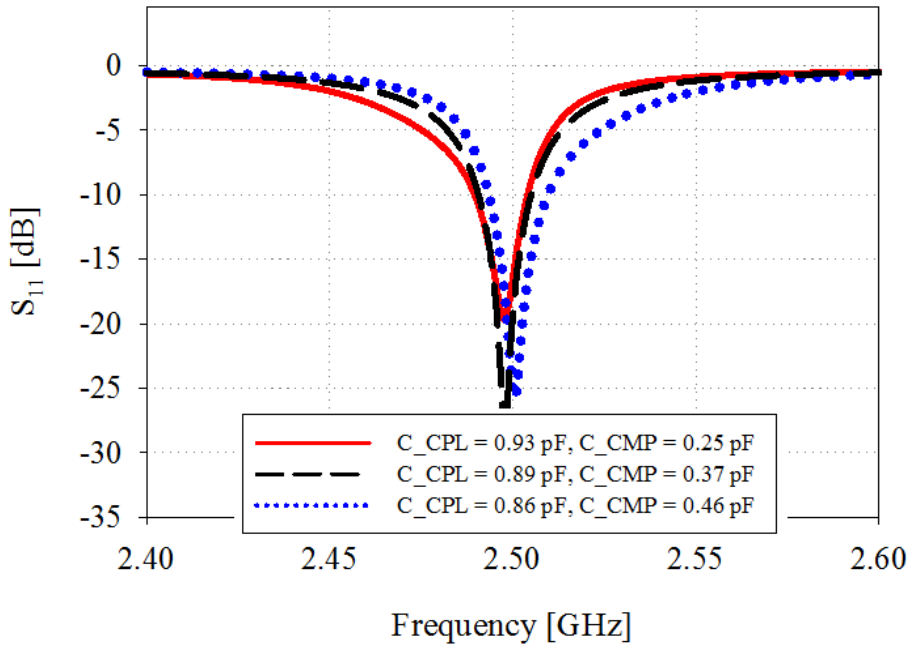
Figure 34: Simulated S11 of the two-element ESPAR antenna.

The array factor null depth is set by the ratio of the parasitic current to the driven element current, which is around 50%. The overall effect of the array factor on the patch radiation pattern

58

results in the beam broadening seen in Figure 33. This phenomenon is totally absent in the 3-element array.

4.4 Conclusion

A novel design method for microstrip patch ESPAR antennas has been presented for both 2-element and 3-element arrays. The array factor calculation for these antennas has been presented and is utilized to show beam scanning using mutual coupling control without phase shifters. Excellent performance in impedance match and gain versus scan angle are exhibited.

CHAPTER 5: A COMPARISON OF THE MICROSTRIP ESPAR TO TRADITIONAL PHASED ARRAY ANTENNAS WITH UNIFORM ILLUMINATION

5.1 Introduction

Phased array antennas are a common solution for applications requiring highly directive, steerable radiation patterns. The relative magnitude and phase of discrete radiators across the antenna aperture are controlled to produce a pattern maximum in a desired direction, to cancel radiation received from a certain direction, or both. While a continuous magnitude control is generally achieved utilizing a variable gain amplifier for each element in active arrays, phase shifters are the prevalent mechanism for achieving beam steering in phased array antennas. The prohibitive cost of precise phase shifters in such arrays has historically constrained the application of this technology. To this end, arrays using parasitic or dummy elements have been presented in an attempt to reduce the reliance on the expensive components, thereby ameliorating cost.

ESPAR antennas utilize mutual coupling between adjacent elements as a feeding technique, eliminating phase shifters for a portion of radiators. The inexpensive 3-element microstrip patch ESPAR at 1 GHz presented in the preceding chapters [33] demonstrated the first instance of reactive mutual coupling control. The design was thoroughly characterized in [34], and exhibited high gain, symmetric and continuous scanning with excellent pattern integrity. An extension of the patch ESPAR technique to include dual-sided beam steering with as few as 2 elements was demonstrated in [35]. In this design, the mutual coupling between the driven and

parasitic elements was actively controlled via tunable reactive loads connecting the elements. The relative phase between the elements was directly impacted by variations in the loads, allowing for beam scanning without the use of phase shifters.

A thorough and detailed comparison to a uniform array with traditional half-wavelength spacing and utilizing phase shifters will provide enhanced insight to the patch ESPAR and the impact of mutual coupling. It is expected that due to the parasitic array's smaller spacing and lack of phase shifters and associated losses, differences in directivity and efficiency will be evident. To best explore the ESPAR functional and performance differences, two uniform arrays with different element spacing and utilizing phase shifters are designed, which take the general form shown in Figure 35.

Figure 35: Layout of traditional uniform phased array.
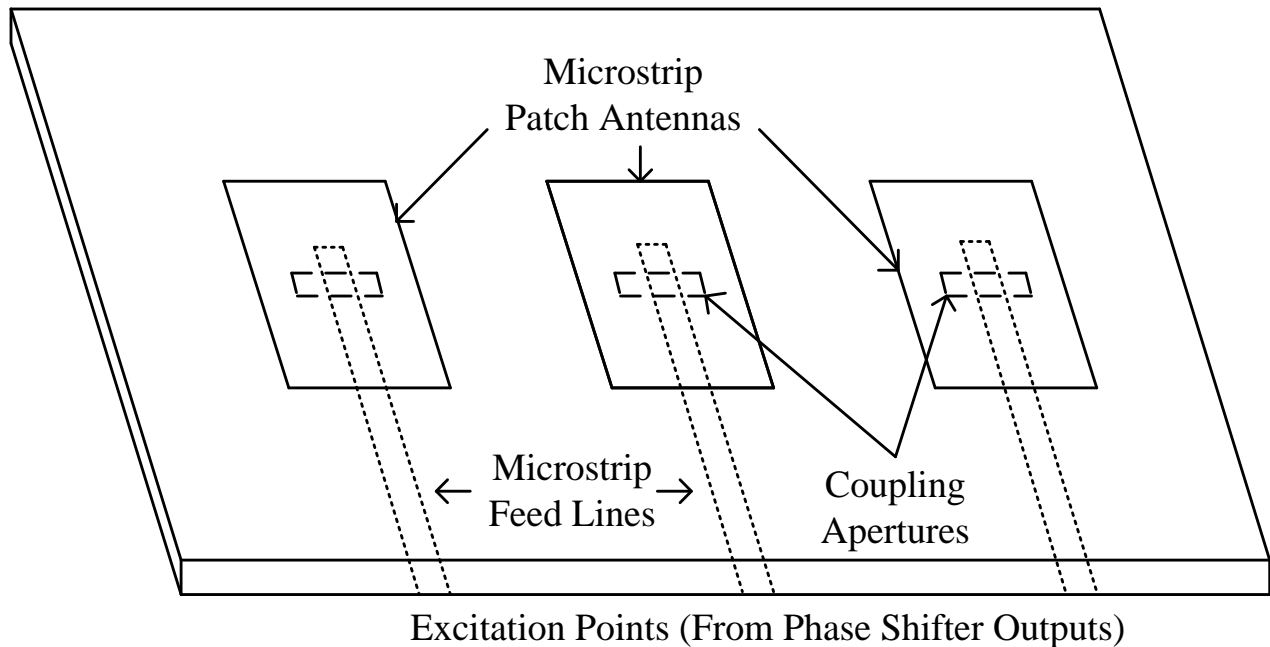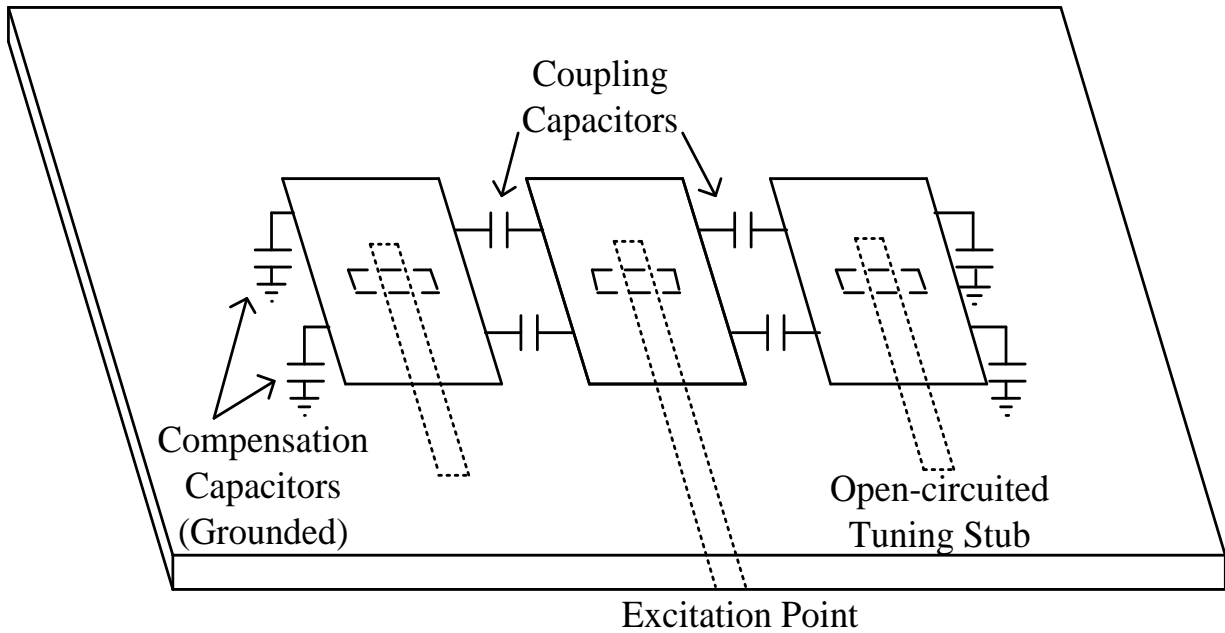
Figure 36: Microstrip patch ESPAR geometry.

The microstrip patch ESPAR employs a unique loading scheme, visible in Figure 36. The standard uniform array with half-wavelength spacing will emphasize the necessarily lower directivity associated with the smaller element spacing in the ESPAR. Secondly, a uniform array with spacing similar to the ESPAR will serve to highlight the benefit of the reactive mutual coupling control technique in terms of efficiency.

Presented herein is a comprehensive treatment of the design and analysis of each array type, with exploration of a number of key performance characteristics, including directivity, efficiency, and impedance matching. This discussion of the fundamental differences in these alternative solutions is critical for the ESPAR technique to be fully understood and more widely utilized.

5.2 Theory and Design

Scanning of the radiation pattern of a phased array antenna is the result of the complex superposition of the radiated fields from independent array elements. The Array Factor (AF) is a powerful tool for this analysis, and is affected by the magnitude and phase of these fields as well as the inter-element spacing:

$$Array\ Factor = \sum_{i=1}^{3} \left| \frac{I_i}{I_1} \right| e^{j(kd_i * cos\theta + \beta_i)}. \tag{14}$$

For the arrays presented, d represents the inter-element spacing, k is the wavenumber, and θ is the observation angle. The relative element current magnitudes, denoted I_i, are only non-unity for the ESPAR array, where the parasitic element currents are smaller in magnitude. The AF is multiplied by the single element radiation pattern to determine the total array pattern.

Controlling the phase shift β allows scanning the beam maximum to the desired observation angle. This is achieved in both uniformly-illuminated phased array antennas with phase shifters, which are typically structures with switched transmission paths which contribute variable signal propagation delays. The ESPAR achieves phase shift control by adjusting the mutual coupling between the elements with the coupling capacitance, C_CPL, while maintaining stable resonance with C_CMP. No phase shifters are utilized. The inter-element spacing is naturally smaller in the ESPAR in order to ensure stronger coupling between the patches; for similarly-sized elements, this roughly quarter-wavelength spacing results in a smaller total array. The anticipated result is a reduction in overall aperture area, which impacts overall directivity.

The compared arrays utilize rectangular microstrip patch antennas, with dimensions given in Figure 37, Figure 38, and Figure 39.
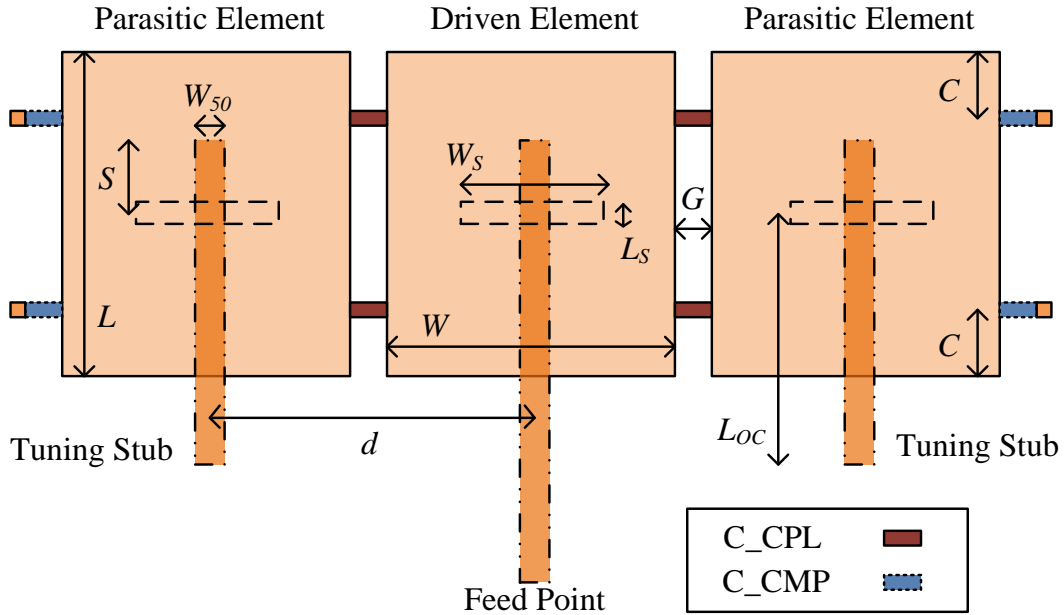
(L = 91, W = 78, d = 81, G = 3, S = 38, W$_{50}$ =3.52, W$_S$ = 21, L$_S$ = 6, C = 25.5, L$_{OC}$ = 28). All dimensions in mm.

Figure 37: Dimensions of the microstrip ESPAR array.
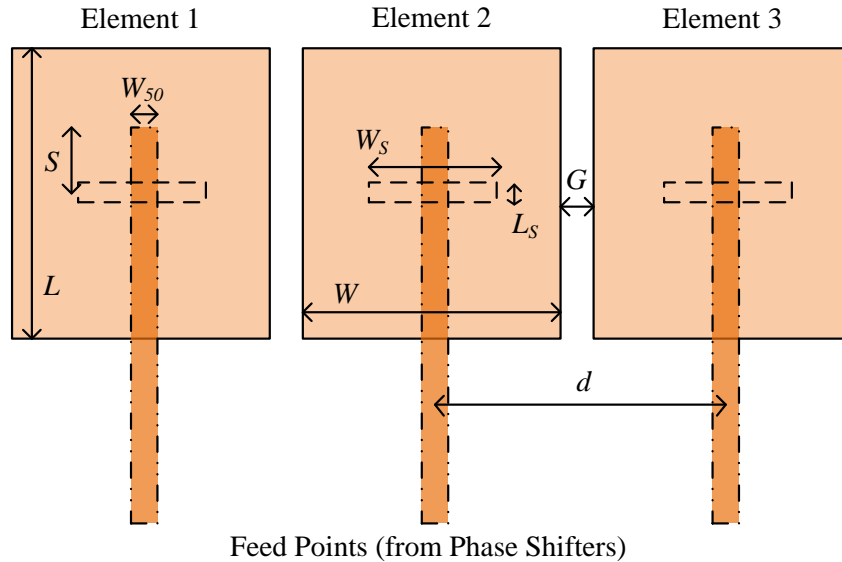
(L = 95.5, W = 78, d = 81, G = 3, S = 55, W$_{50}$ =3.52, W$_S$ = 21, L$_S$ = 6).All dimensions in mm.

Figure 38: Dimensions of the closely spaced uniform illuimation microstrip array.
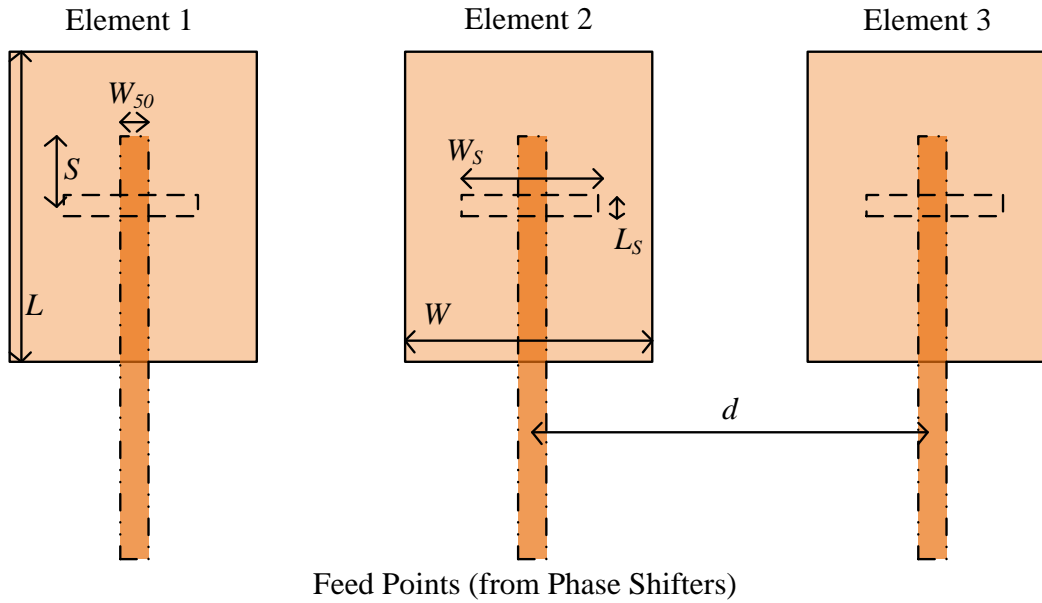
(L = 96.5, W = 78, d = 150, S = 55, W$_{50}$ =3.52, W$_S$ = 21.5, L$_S$ = 2). All dimensions in mm.

Figure 39: Dimensions of the uniform microstrip array, half-wavelength spacing.

While the uniform arrays utilize patch antennas with length corresponding to resonance at 1 GHz, the ESPAR patch lengths are chosen to resonate at 1.05 GHz to allow capacitive loading while operating at 1 GHz [34]. The widths are large to increase the single element directivity. However, care must be taken to avoid exciting the second mode of the patch antenna, corresponding to a resonant width. Such modes are similarly loaded by the varactors and can cause significant cross-polarized radiation at the operation frequency if left unchecked. All arrays utilize 62-mil Rogers Duroid 5880 ($\varepsilon_r = 2.2$, *tanδ* = 0.0009) substrate as the antenna layer. The feed layers are comprised of 60-mil Rogers RO4003 ($\varepsilon_r = 3.55$, *tanδ* = 0.0027). The uniform arrays utilize 50-ohm microstrip lines to feed the patches. Energy is coupled through apertures in the substrates' common ground plane. The microstrip lines are terminated with open-circuits approximately one quarter-wavelength beyond the apertures to induce a current maximum

directly below the slots, allowing for strong coupling. This distance is also tuned to achieve impedance matching.

5.3 Full-wave Simulation

Ansoft's High Frequency Structure Simulator (HFSS) full-wave solver package was utilized to compute the performance of each array. Wave ports were designed both to simulate feeding from a signal generator and to implement phase shifts. These phase shifters are non-dispersive and lossless. The three ports in each of the uniform arrays were fed with a phase delay to cause a phase gradient across the aperture, which resulted in scanning. Post-processing calculations allowed for inclusion of associated phase shifter losses to provide total efficiency figures.

The patch ESPAR radiation pattern was scanned using the method previously demonstrated in [33-35]. Variable capacitive loads were placed in the positions shown in Figure 37. Beginning with a symmetric loading design, the system was solved and a symmetric radiation pattern with a maximum at boresight was produced. Thereafter, the capacitive loads were adjusted to manipulate the mutual coupling between the driven and parasitic elements. The symmetry of the structure is then disrupted, necessitating relative changes between the parasitic element currents. The consequent adjustments to induced current phase directly altered the angle of beam maximum. Further, the adjusted capacitance values on the parasitic element edges were used to maintain stable resonance at the operation frequency.

5.4 Results and Discussion

Frequency sweeps were performed for each of the arrays, and the resulting impedance match is shown in Fig. 3.
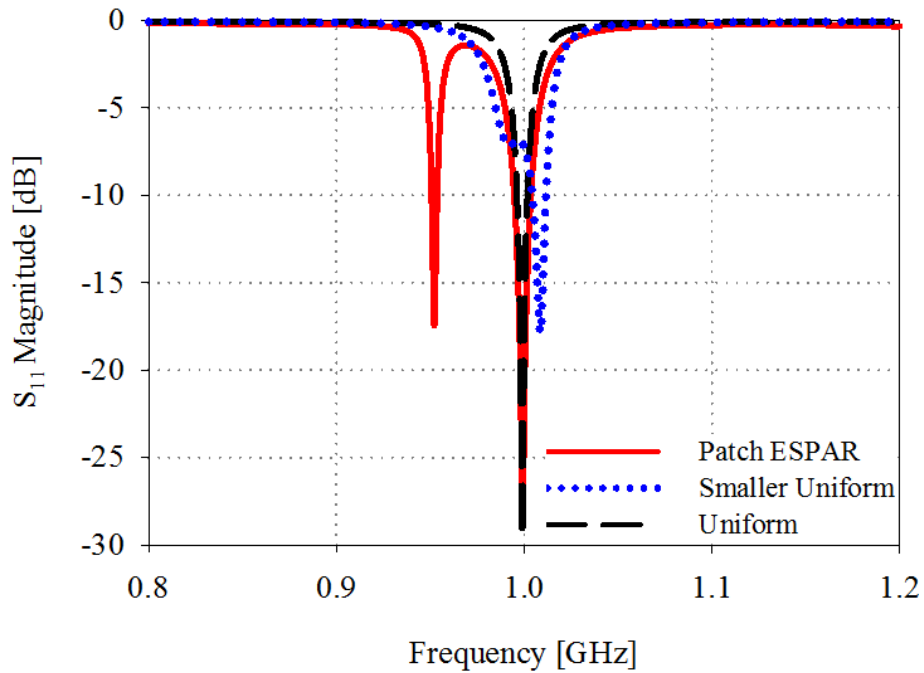
Figure 40: Simulated S11 of the phased array antennas.

It is evident that the uniform array with half-wavelength spacing is well-matched at 1 GHz, while the smaller uniform array is suffering from impedance mismatch. It is clear from the split resonance phenomena that mutual coupling between the elements is quite strong. This strong coupling is also present in the similar patch ESPAR geometry; however, careful inspection of the red curve reveals that the split resonance is even more pronounced, and impedance match is maintained at 1 GHz. The stronger coupling effect, which forces the resonant frequencies further apart, is caused by the large value of C_CPL. Maintained impedance

match at the operation frequency is a result of careful adjustment to the value of C_CMP. The second resonance at roughly 0.95 GHz is not utilized.

The radiation properties of all three array types were collected from the simulations and are displayed above in Table 1. The most critical and immediately obvious difference between the patch ESPAR and the uniformly illuminated arrays is the directivity. The difference in total aperture size in the array dimension of the uniform arrays causes the largest difference in directivity; as directivity is proportional to aperture size. The aperture sizes of the microstrip patch ESPAR and the smaller uniform array are nearly identical, save for a slight change in the patch length dimension. The 0.4 dB difference in directivity is the result of non-uniform current magnitude across the parasitic array. The directivity difference is clear in Figure 41 (a) and (b), which display the H-Plane radiation patterns for the 3 arrays both at boresight and scanned, respectively. The beamwidth difference is recorded in Table 1, and is pronounced and obvious at boresight, where the effect of the larger aperture is apparent in the uniform array radiation pattern. The first side lobes of the uniform array pattern are present due to its larger size. Figure 41 (b) shows the arrays at their maximum scan angle, given the stipulation that side lobe level (SLL) should be kept better than 10 dB. While the maximum of the patch ESPAR radiation pattern does not reach to the same limit as the uniform arrays, the pattern also exhibits much lower side lobe levels, showing a reduction of roughly 5 dB below the uniformly illuminated arrays in the upper hemisphere.

68

Table 2: Array Performance Comparison

| Array | Array Performance Characteristics at 1 GHz | | | | | | | | |
| | Without Phase Shifters | | | # of Phase Shifters | With Phase Shifters | | Max Scan Angle [deg] | Array Dimension [λ] | Boresight Beamwidth [deg] |
	Directivity [dBi]	Peak Gain at Boresight [dBi]	Efficiency		Peak Gain [dBi]	Efficiency			
ESPAR	8.4	7.5	81.4%	0	7.5	81.4%	±17	0.81	56
Smaller Uniform	8.8	7.9	80.8%	3	6.9	64.2%	±23	0.81	55
Uniform	10.9	9.8	77.3%	3	8.8	61.4%	±22	1.5	31

(a)

(b)
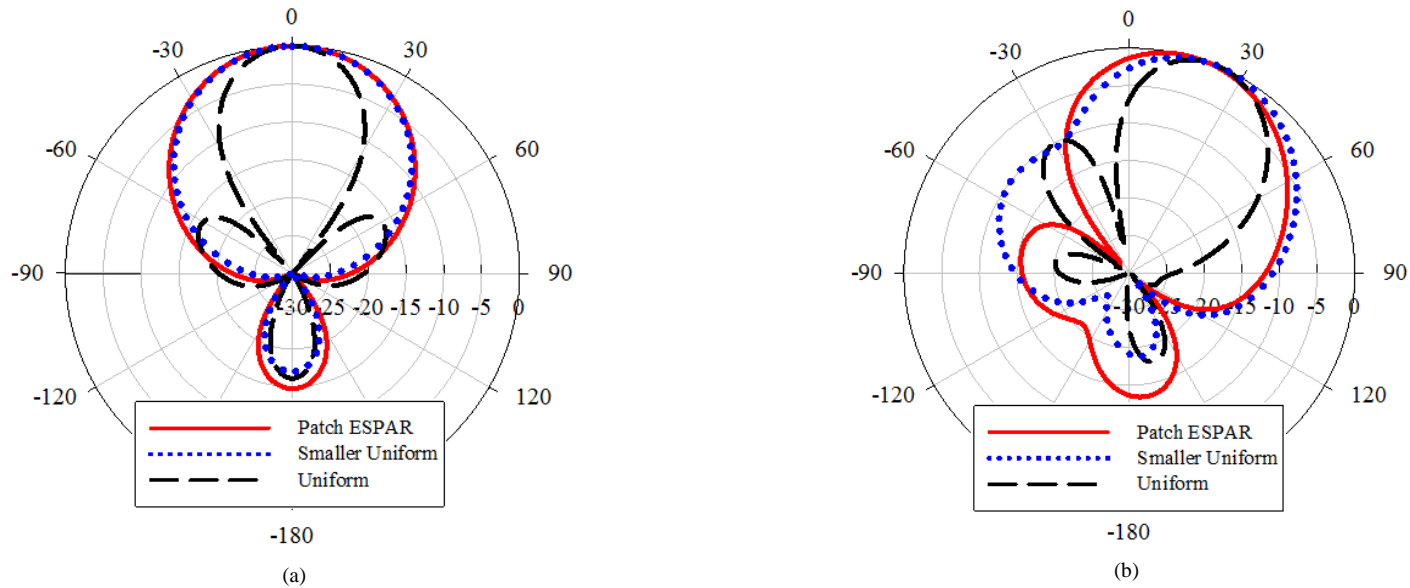
Figure 41: Simulated radiation patterns of the compared arrays. (a) Boresight. (b) Scanned array patterns.

69

The efficiencies of the phased array antennas are also presented in Table 2. Before introducing phase shifter losses, the microstrip patch ESPAR has an efficiency of 81.4%, which is better than both uniformly illuminated arrays. Inclusion of a 1 dB phase shifter loss drops the uniform array efficiencies further to less than 65% for each. The losses are integrated by cascading the appropriate efficiencies with those of the simulated arrays; in total, the ESPAR lags in gain at boresight by 1.3 dB behind the half-wavelength uniform array. It must be noted that such losses would generally increase at higher frequencies, implying that the ESPAR technique would equal or surpass designs employing phase shifters in gain, due to the advantage in efficiency. The beamwidth, maximum scan angle, and directivity are not affected by inclusion of phase shifters.

To illustrate the effects of mutual coupling and non-uniform radiating current magnitude, Figure 42 is presented, which shows normalized current magnitude plots on the antenna elements in the boresight simulations at 1GHz. The patch ESPAR is shown in Figure 42 (a), where the effects of the compensation and coupling capacitances on the radiating current are visible. The current magnitude is quite strong in the region between the coupling capacitors, whereas the parasitic element currents are much weaker, including the region around the compensation varactors. The smaller uniform and half-wavelength uniform arrays are visible in Figure 42 (b) and (c), respectively. From the bird's eye views of Figure 42 (a) and (b), strong electric field interaction between adjacent patches is shown in the inter-element gaps. This effect is absent in Figure 42 (c), where the patches are spaced much further apart. Similarly in Figure 42 (a) and (b), the lower vector magnitude plots show a non-uniform distribution.
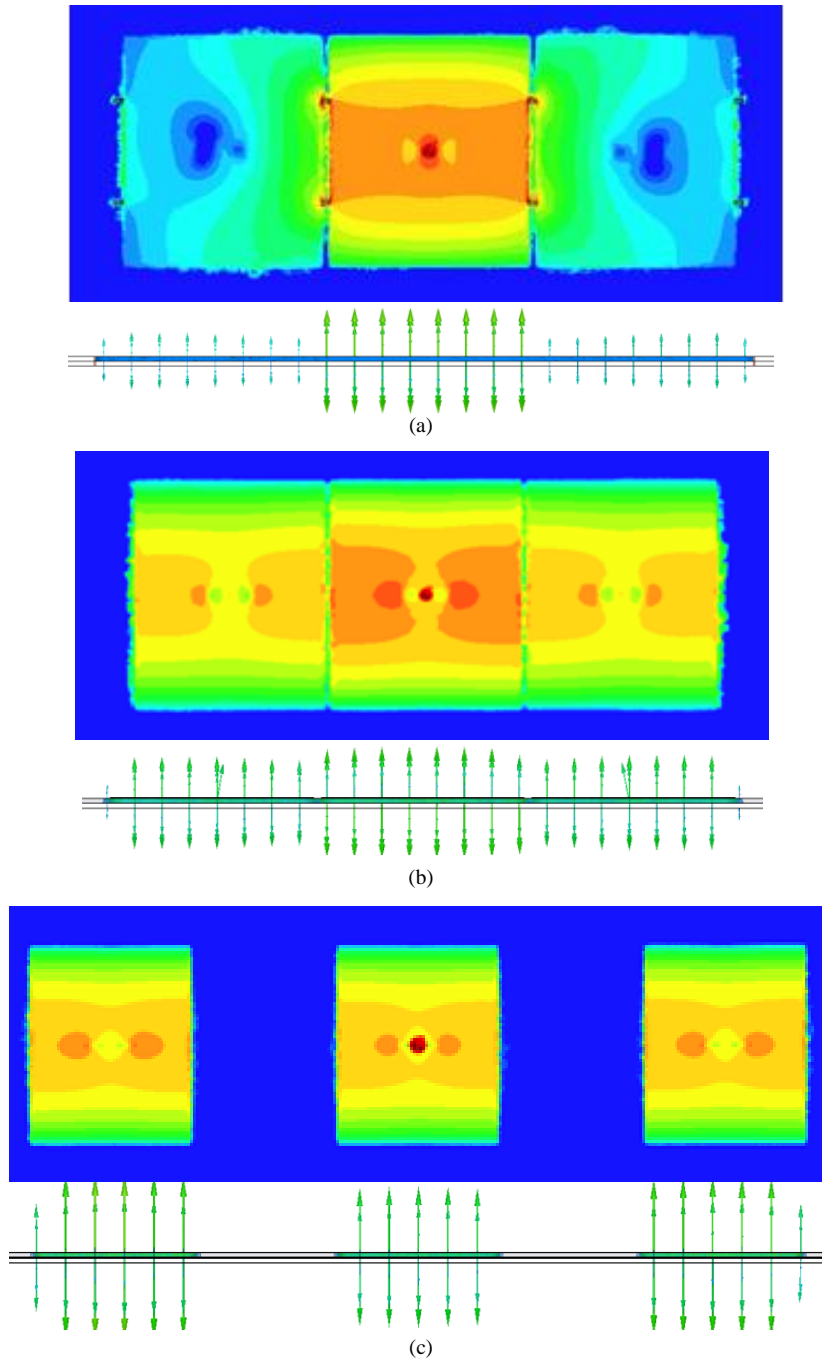
Figure 42: Simulated current distributions in the patch antenna dielectric layer. Top: Current magnitude distribution. Bottom: Side view of E-field vector. (a) Microstrip patch ESPAR. (b) Smaller uniform array. (c) Half-wavelength uniform array.

The parasitic array exhibits this behavior because the passive elements couple only a portion of the energy from the driven element. In Figure 42 (b), the smaller uniform array suffers from uncompensated mutual coupling: energy from the two exterior patches also couples onto the center element, causing a slightly higher field magnitude. The vector plot in Figure 42 (c) for the half-wavelength uniform array shows no such behavior as the gaps are too large for strong coupling to occur.

5.5 Conclusion

The 3-element microstrip patch ESPAR has been thoroughly compared to two uniformly-illuminated patch phased arrays. The ability to scan the radiation pattern without phase shifters results in a less expensive and more efficient design over its more common, uniformly-fed counterparts. Ongoing work includes design simplification to produce a single-layer microstrip patch ESPAR, large array integration, and expansion to include E-plane scanning.

CHAPTER 6: FABRICATION IMPROVEMENTS AND SINGLE-LAYER DESIGN

6.1 Overview

The performance benefits inherent to phased array antennas are negatively offset by the historically high cost of fabrication, which is chiefly attributed to phase shifters [36]. Phase shifters adjust the relative phase of radiating currents for each radiator in an array, allowing control over the angle of the total radiation pattern maximum. To alleviate this cost burden while achieving a scanning radiation pattern, reactively-controlled and switchable arrays have proven effective, including the ESPAR. The ESPAR utilizes intrinsic coupling of closely-spaced elements in conjunction with tunable capacitive loads to achieve scanning control.

Recently, a number of low-cost scanning antenna arrays utilizing microstrip elements have been presented [24, 37]. Integration of these parasitic arrays as cells in larger phased array antennas has been discussed thoroughly in [37], where reconfigurable microstrip Yagi antennas using PIN diodes provided increased scan range. Similarly, PIN diode switches were used in [24] to produce scanning patterns by controlling connection to microstrip loading stubs for non-contact vital sign measurement. In each presentation, it is clear that abrupt changes to the structure caused by ON/OFF switching causes largely varying resonance characteristics. The ESPAR technique avoids such issues by using analog reactive loads with continuous tuning capability. To this end, a 3-element microstrip patch ESPAR at 1 GHz was shown to exhibit high

gain, high return loss across the continuous scan range, and excellent efficiency, with stable resonance and pattern quality.

However, the microstrip patch ESPAR design requires thorough DC biasing design to control the reactive loads; namely, the varactors require DC isolated RF grounds. This was previously achieved using an additional fabricated layer containing floating RF grounds in the form of radial microstrip stubs. Additionally, open-circuited microstrip line stubs were utilized as resonance tuning elements for the parasitic patch antennas. Both of these solutions complicate the fabrication process, with the required multilayer alignment and bonding increasing the probability of failure. Furthermore, multilayer designs place an upper limit on the application of this structure, as on-wafer arrays do not generally have access to multilayer techniques. In this paper, these features will be shown to be unnecessary, as the same performance can be achieved in their absence.

An inset-fed 3-element microstrip patch ESPAR at 1 GHz is presented. This is the first instance of a *single-layer* microstrip ESPAR with explicit reactive control over the mutual coupling and precisely maintained resonance. Reverse-biased diode varactors are placed both between the elements and as resonance tuning elements on the parasitic patch antennas, as illustrated in Figure 43 (a). To change the capacitance of the varactor diodes, the patch antennas and ground plane are DC biased by variable voltage supplies, allowing direct manipulation of the induced current properties, and consequently, the array radiation pattern scan angle. DC biasing was previously achieved by employing RF ground stubs on the feed layer, which provided both

RF grounding and independent DC voltage for the varactors, while introducing design

complexity and increasing cost.

(a)

(b)
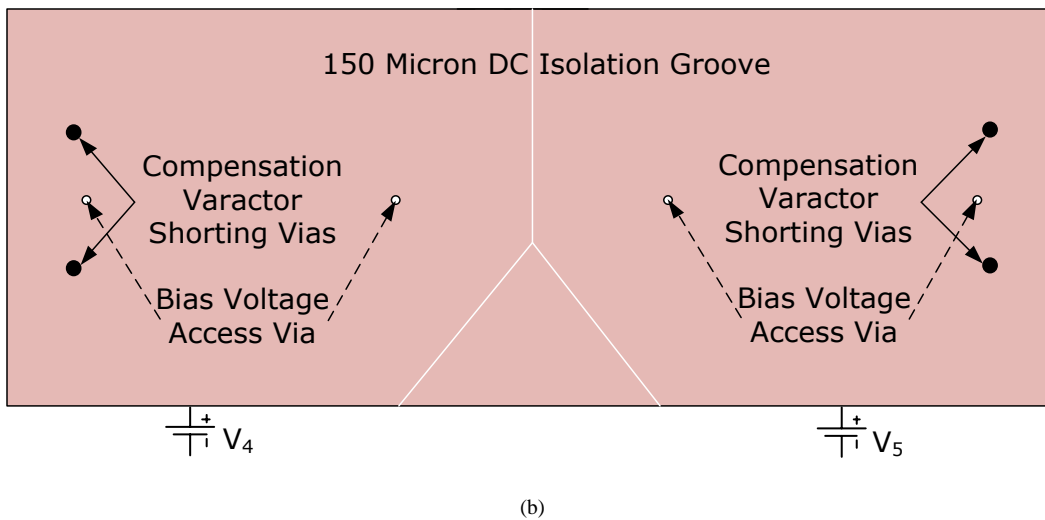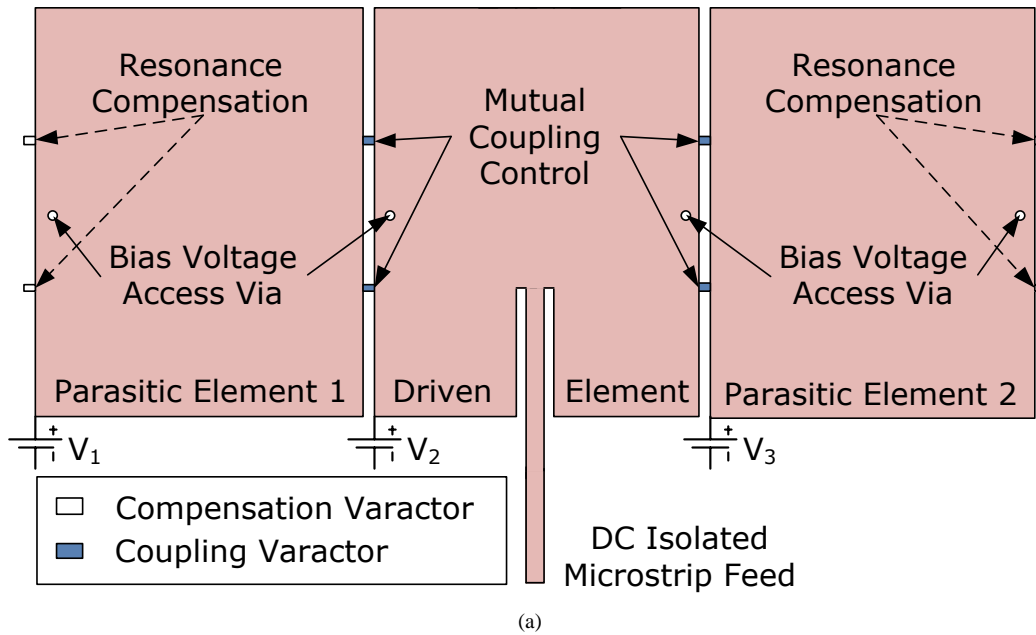
Figure 43: Single layer microstrip patch ESPAR. (a) Patch antenna surface and loading configuration. (b)

Ground layer with inverted-Y isolation groove

To simplify the design, a 150 µm inverted-Y groove is cut longitudinally on the ground plane as seen in Figure 43 (b), which splits below the microstrip feed line to circumvent the SMA connector. Since the array is symmetric and the groove is parallel to the image current, the effects on RF performance are negligible, save for a slight upward shift in resonant frequency. However, by DC isolating the two ground plane halves, the array contains sufficient independent DC nodes to uniquely control each varactor without floating RF grounds. This constitutes a significant simplification over the previous demonstration and provides the crucial benefit of reduced loss. Furthermore, the DC isolation to the signal source, which was intrinsic to the aperture-coupled ESPAR, is integrated by means of the ground plane grooves. This enhancement negates the need for an external DC blocking solution.

By confining the design to a single layer, the microstrip ESPAR design process can be extended to include on-wafer designs at and above Ku band for arrays of any element count. The risks of deformation in the high-temperature bonding stage are mitigated. Further, the single layer ESPAR has a lower profile, and can be readily integrated in a conformal array design.

6.2 Design and Full-wave Simulation

Rectangular microstrip patch antennas of length L and width W as shown in Figure 44, are selected as the radiating elements. The copper patches are created on a single Rogers RT Duroid 5880 board ($\varepsilon_r = 2.2$, $tan\delta = 0.0009$) with thickness of 62 mil, and are fed with 50-ohm microstrip lines. The driven element was designed independently and impedance matched using inset feeding at depth S. Then, the parasitic patch antennas were placed beside the driven element

at a gap width *G,* and the compensation and coupling capacitive loads, *C_CMP* and *C_CPL,* were introduced.
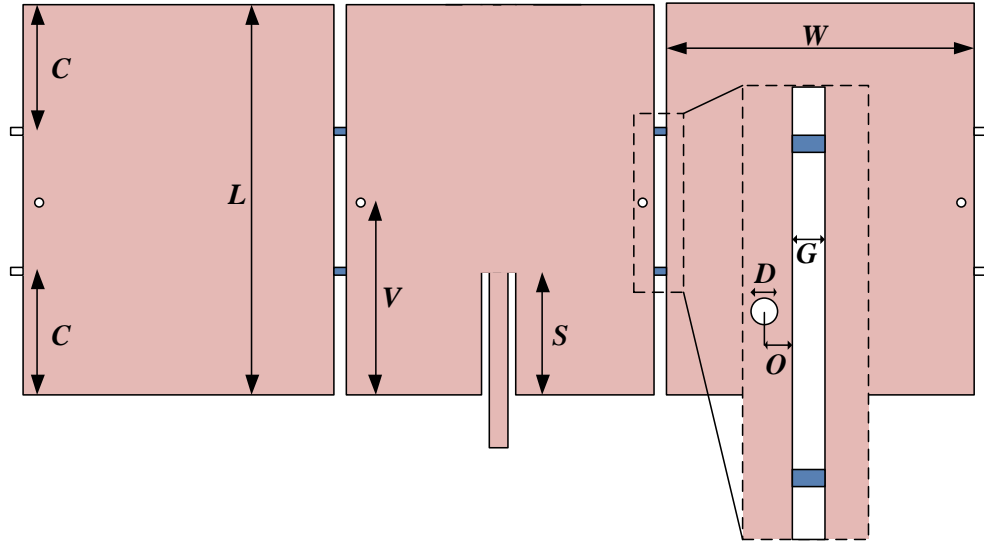
(C = 31, L = 97, V = 48.5, S = 31, W = 77, D = 0.25, G = 3, O = 2.8.) All dimensions are in mm.

Figure 44: Detailed dimensions of the parasitic array antenna layer. Inset: Zoomed view of the inter-element gap with coupling varactors.

These parasitic elements lack any explicit feeding mechanism, and are instead fed solely by mutual coupling. This eliminates losses present in the previous microstrip ESPAR iterations, where the parasitic elements had their feed lines terminated with fully reflective loads.

The lumped element capacitors were set to a value of 3.4 pF, which is the approximate midpoint of the available varactors' loading capability. Tuning of the resonant frequency was achieved by slight modifications to the capacitor load location C and the patch length L. Symmetry in the load maintains symmetry of the entire design, leading to necessarily symmetric radiation patterns with maximum at boresight. Scanning the radiation pattern is achieved by adjusting the coupling and compensation varactor values in a non-symmetric fashion.

77

The microstrip patch ESPAR was simulated in HFSS. Variable-reactance lumped element sheets were used in place of varactors in order to examine the load effects. The DC isolation grooves were cut into the ground plane to incorporate their effects on the RF performance of the array. The signal was injected via wave port on the 50 ohm microstrip line connecting to the inset-fed driven patch, and the array was independently solved for each loading scheme. This allowed extraction of the induced current magnitude and phase characteristics and characterization of their relation to the capacitive load value. The data is collected by exporting the relative electric field intensity inside the radiating slots of the parasitic and driven patch antennas:

$$\beta_P = tan^{-1}\left(\frac{Im\{E_{ZP}\}}{Re\{E_{ZP}\}}\right) - tan^{-1}\left(\frac{Im\{E_{ZD}\}}{Re\{E_{ZD}\}}\right), \tag{15}$$

$$M_P = \frac{|E_{ZP}|}{|E_{ZD}|}. \tag{16}$$

β_P is the relative phase shift of the parasitic patch antenna, and M_P is the relative magnitude. Here, E_{ZP} and E_{ZD} represent the *Z*-Component of the electric field intensity inside the radiating slots of the *parasitic* and *driven* elements, respectively. For the presented ESPAR with one driven and two parasitic elements, the total array radiation pattern can be calculated using the familiar array factor equation:

$$Array\ Factor = 1 + \sum_{i=1}^{2} M_{Pi}e^{j(kd_i*sin\theta+\beta_{Pi})}. \tag{17}$$

The gain of the proposed array was simulated to be 7.3 dBi, which shows that the single layer design does not lose significant performance compared to the previously demonstrated multilayer design, simulated at 7.5 dBi.

6.3 Fabrication, Measurement, and Results

A prototype array was fabricated using a combination of copper etching and milling. Access holes were drilled through the patches for applying DC voltage, which housed 0.25 mm diameter wires. These wires were insulated to avoid shorting the patches to the RF ground plane, and their high inductance and precise location provided for a negligible effect on resonance and radiation performance. Shorting vias were placed at the resonance compensation varactors. Infineon BB857E7902 varactors were soldered in the coupling gaps and on the exterior parasitic element edges.

The array, seen in Figure 45, was mounted for measurement in an anechoic chamber.

(a)   (b)
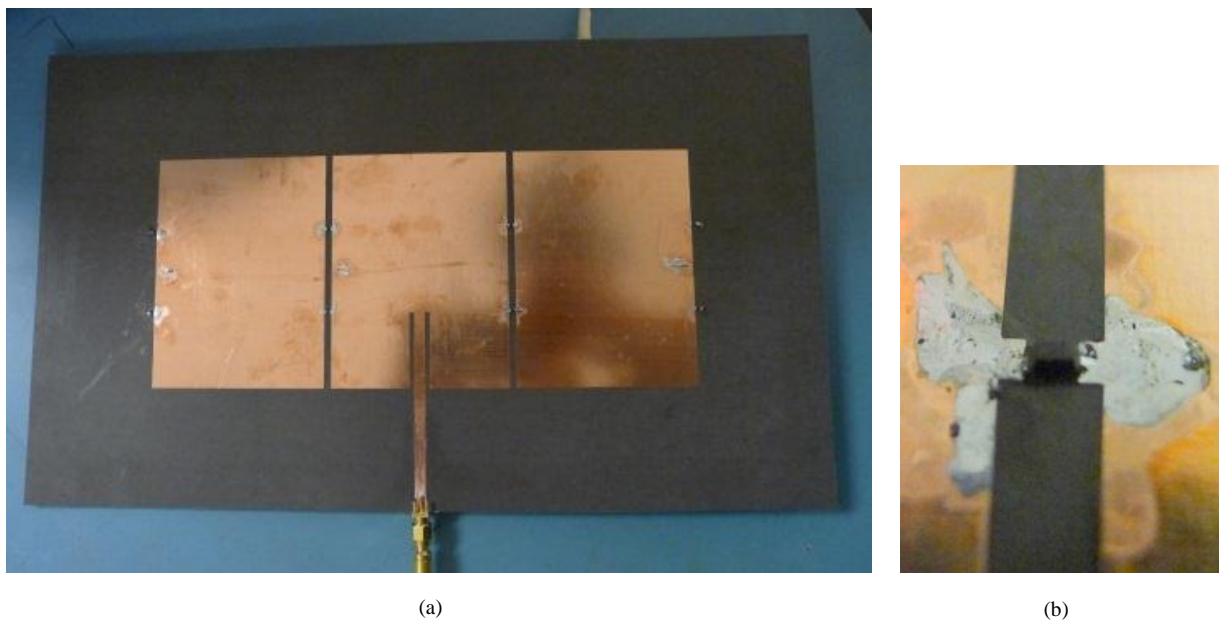
Figure 45: Photograph of the prototype phased array antenna. (a) View of the finalized patch antenna surface. (b) Close-up view of a chip varactor in the coupling position.

DC power supplies were set to produce bias voltages corresponding to the boresight and scan cases, and the input reflection coefficient and radiation pattern were measured, as seen in Figure 46 and Figure 47, respectively.

(a)

(b)
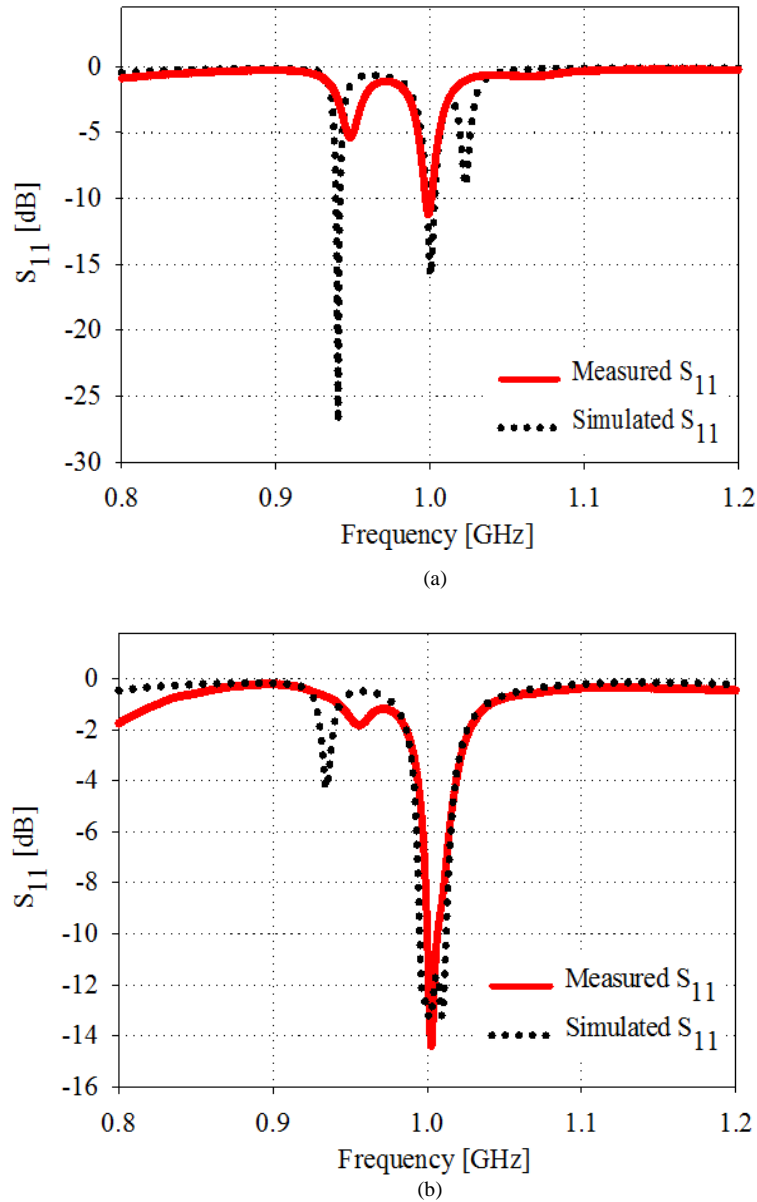
Figure 46: Simulated and measured S11 of the microstrip patch ESPAR. (a) Boresight. (b) Scan angle 15°.
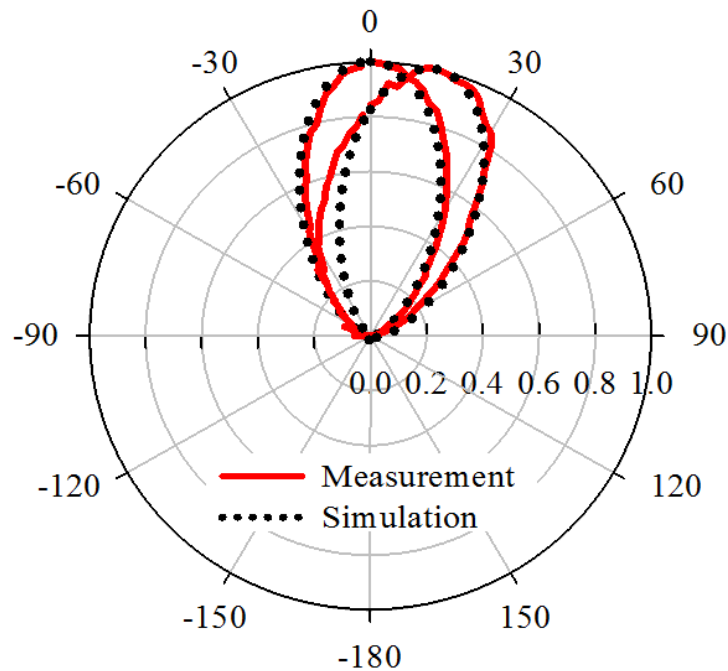
Figure 47: Simulated and measured normalized linear radiation patterns at 1 GHz for boresight and 15° scan angles.

It is noted that the good impedance matching of better than 10 dB is consistent through the scan angle extrema, from boresight to 15°, and the resonance is clearly kept stable at the operation frequency. The multi-resonant response is inherent to the ESPAR technique, where coupled identical resonant structures exhibit resonance splitting. The 1 GHz resonance is the even mode resonance, while the lower frequency mode is the odd mode of the structure. The higher resonance seen in Figure 46 (a) at 1.03 GHz in the simulation curve results from the excitation of the 2nd mode of the parasitic elements. This is absent in measurement due to the presence of the patch DC bias wires, which disrupt that mode. The radiation patterns are in excellent agreement

with simulation, demonstrating narrow main beams and a lack of side lobes. Scanning to negative angles is easily achieved due to symmetry by reversing the varactor loading.

6.4 Conclusion

The microstrip patch ESPAR has been simplified to a single layer design, as evidenced by the 1 GHz 3-element array presented herein. Vast improvements to the design process have resulted in a more reliable fabrication process and less complex design method. These improvements have expanded the applications of the microstrip ESPAR to include higher frequency, on-wafer and conformal designs, with no loss in performance compared to previously demonstrated iterations. The culmination of the research into the microstrip ESPAR topic includes integration of these subarrays into a larger planar phased array with higher directivity.

CHAPTER 7: ARRAY INTEGRATION OF THE MICROSTRIP PATCH ESPAR

7.1 Introduction

Highly directive uniformly-illuminated arrays require high precision feed networks, calibrated both in magnitude and phase, to maximize the potential directivity enhancement allotted by their electrically large aperture size [38]. The phase shifters or true time delay units for each element account for a considerable share of the array fabrication cost, and therefore, a substantial reduction in the cost of phased arrays can be achieved by eliminating the need for some or all of the phase shifters. A wide variety of solutions have surfaced which are capable of electronic beam scanning without discrete packaged phase shifters [39-41]. The ESPAR technology is a response to the simultaneous demand for electronic beam scanning with reduced feed network complexity and diminished production cost. Generally, the ESPAR technique generates arrays which scan without the use of phase shifters by employing mutual coupling as a feed for parasitic radiators. As the tuning is achieved via analog reactive loads rather than RF switches, the scanning is continuous [23, 33, 42, 43].

The microstrip patch ESPAR was designed specifically to extend the inexpensive electronic scanning technique to larger planar arrays, providing the higher gain and pattern scanning associated with phased array antennas while lowering the number of necessary phase shifters. A design exhibiting H-Plane scanning up to 15° off boresight was presented in [33]. This array employed tunable capacitive loading to adjust the mutual coupling between the driven

patch and adjacent parasitic radiators, with additional tuned capacitive loads on the parasitic elements for maintaining resonance at the operation frequency. While successful as a proof-of-concept for the microstrip patch as a suitable ESPAR candidate, the necessary bonding between the feed and radiation layers was not well-suited for integration in a larger array. The technology was improved in this regard in [20], where a 3-element array was designed on a single layer and featured an integrated DC biasing system. This simplification to the fabrication stage was a critical step toward full array integration.

In this paper, a fully integrated array of microstrip patch ESPAR antenna subarray cells is presented for the first time. This array consists of 12 total radiating elements, with a 2x2 cell layout, as shown in Figure 48.
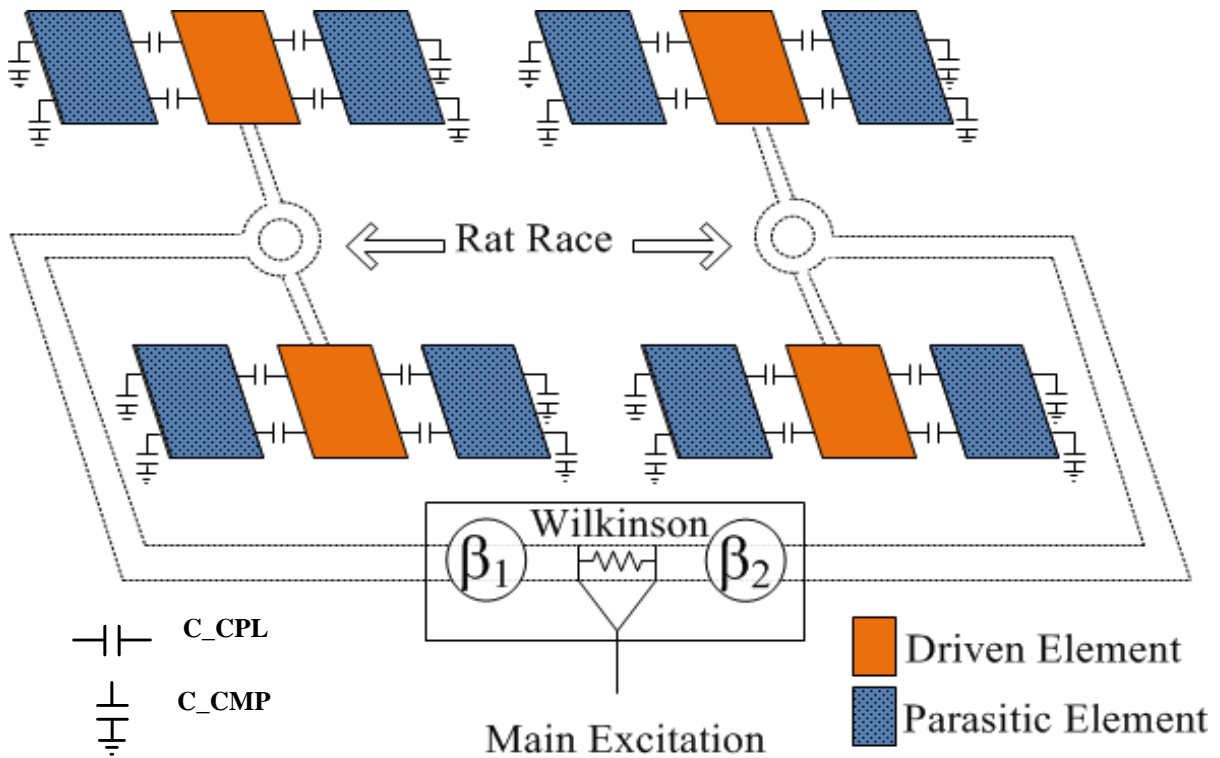
Figure 48: Proposed microstrip ESPAR array layout.

Vertically-aligned cells are rotated 180°, which facilitates the compact feed network centered on the backside. These subarrays are 3-element microstrip patch ESPARs with one driven element, two parasitic elements, and no phase shifters, capable of scanning -20° to +20° in the H-Plane. The mutual coupling control capacitors *C_CPL* and resonance compensation capacitors *C_CMP* are depicted at the inter-element gaps and parasitic element exterior resonant edges, respectively. One ESPAR subarray cell is illustrated in Figure 49 to scale. The simulated performance of the single-layer microstrip patch ESPAR is recorded below in Table 3.
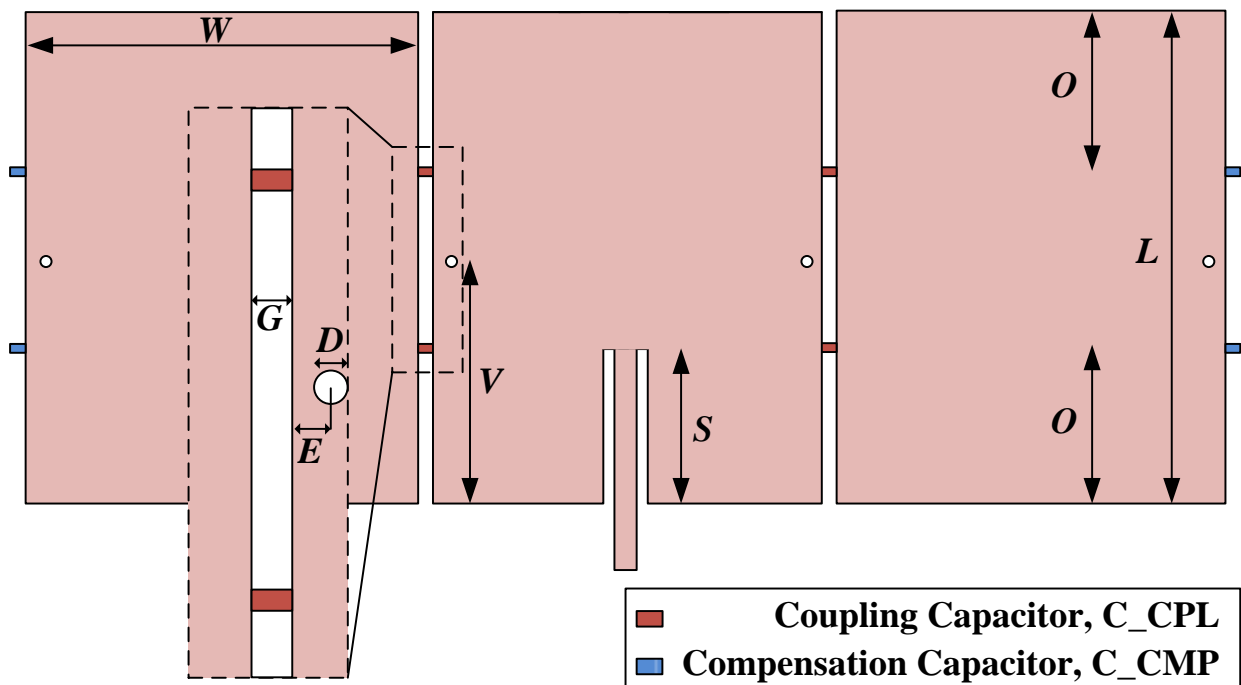
[O = 31, L = 97, V = 48.5, S = 31, W = 77, D = 0.25, G = 3, E = 2.8] All dimensions in mm.
Figure 49: Proposed microstrip ESPAR subarray cell design.

Table 3: Simulated Subcell ESPAR Performance.

(ALL VALUES GIVEN AT 1 GHZ.)

Boresight Performance		20° Scan Performance	
Gain [dBi]	7.8	Gain [dBi]	6.9
HPBW [°]	58	HPBW [°]	51
S_{11} [dB]	-15	S_{11} [dB]	-11
η [%]	81.1	η [%]	71.6
1st S_{LL} [dB]	-	1st S_{LL} [dB]	-13
1st Sidelobe [°]	-	1st Sidelobe [°]	-64

7.2 Array Theory and Design

Traditional uniformly-illuminated scanning arrays avoid the growth of high sidelobes by maintaining the special sampling period at or below a half-wavelength, which prevents the growth of grating lobes in the array factor by satisfying the Nyquist sampling criterion for scans up to 90° [44]. The primary difference of the ESPAR array is the tighter element spacing within the subarray cell, which are necessary to create strong mutual coupling. The chosen subarray cell spacing of one wavelength does not result in large sidelobes due to the ability to scan the subarray cell radiation pattern in tandem with the desired full array beam direction. Proper execution of this array design technique requires careful, simultaneous consideration of both the ESPAR subarray cell and the array layout.

7.2.1) Array Factor Considerations

For a given array aperture size, eliminating phase shifters implies an increase in the sampling period between phase-corrected radiators. The microstrip patch ESPAR selected to mitigate this undesired effect compensates by correcting the relative phases within the subarray cell. To illustrate, Eqn. (18) shows the equivalent normalized array factor (*AF*) derivations for a 12-element phased array antenna in the *XY* plane, with element 1 centered at (0,0). It assumes identical radiating elements with arbitrary phase delays β_i and unequal relative current magnitude I_i:

$$AF = 1 + \sum_{i=2}^{12} \left|\frac{I_i}{I_1}\right| e^{j(kdx_i sin\theta cos\phi + \beta_i)} e^{j(kdy_i sin\theta sin\phi)} \qquad (18)$$

where k is the wavenumber, and $d_{X,Y}$ are the relative X-Y coordinates of each of the 12 elements. However, if the 3-element subarrays can be assumed to exhibit identical performance, with corresponding elements exhibiting the same magnitude and phase distributions, it is valid and more convenient to treat the system as an array of subarray cells. Further, as scanning is only required in the elements' H-Plane (*XZ* plane), that cut of the array factor ($\varphi = 0°$) simplifies to

$$AF = 1 + \sum_{i=2}^{4} e^{j(kd*sin\theta + \beta_x)}. \qquad (19)$$

Rather than calculating an array factor with regard to each individual microstrip patch element, it is more appropriate to treat each subarray cell as an element with the distance between the driven elements taken as the spacing. These parameters are substituted in (19) for boresight and scanned cases, and the resulting array factors are plotted in Figure 50 (a) and (b), respectively. Grating lobes appear in Figure 50 (b) at roughly -40°, on the opposite side to the desired main beam peak

at +20°. This is inconsequential for the ESPAR array, where the subarray cell pattern is scanned as well, reducing the element pattern in the direction of these undesired lobes.
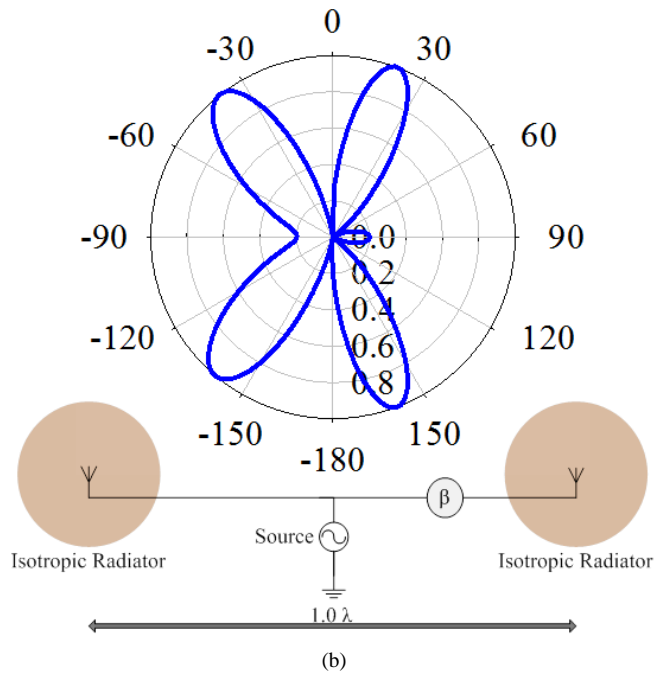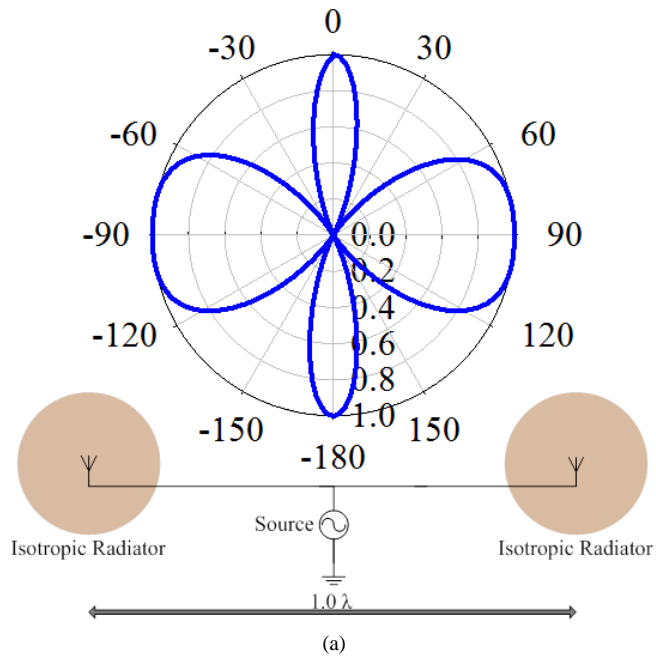
Figure 50: Array factor calculations for n=2 isotropic elements with a spacing of 300mm. (a) Boresight case.

(b) Scanned to 20° [β = 127°.]

89

The period between driven elements in the phased array is inversely proportional to the expense afforded to the T/R modules for those elements. For a constant aperture size, the microstrip patch ESPAR array is less expensive than an array employing the traditional half-wavelength lattice. For a 2λ linear space in the H-Plane, the microstrip ESPAR requires a maximum of 2 phase shifters; therefore, the cost is 50% of that for the 4 phase shifters in the traditional lattice with spacing of $\lambda/2$.

Figure 51 illustrates the advantage of the microstrip patch ESPAR compared to a thinned array.
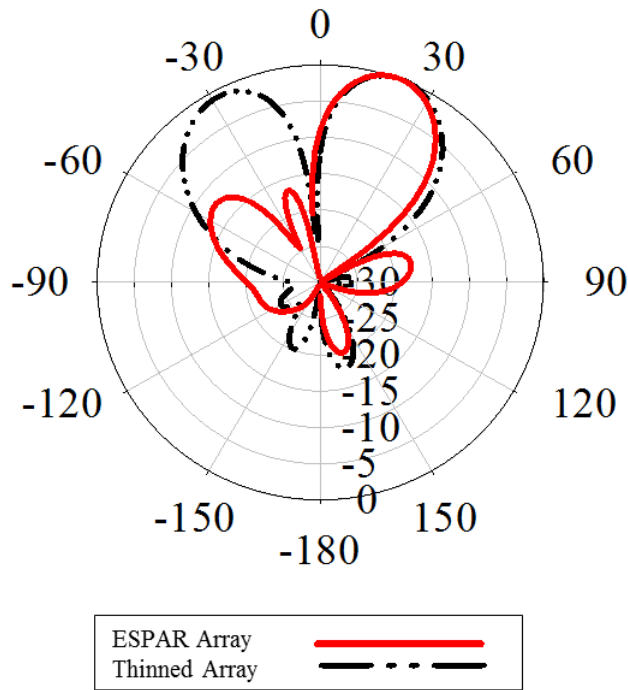
Figure 51: Simulated radiation patterns of the microstrip ESPAR array and the thinned array when scanned to 20°.

The schematics for each radiating structure are shown in Figure 52. The spacing is set to one wavelength, and a single phase shifter is used for each, with additional phase correction in the ESPAR structure by the tunable varactors.
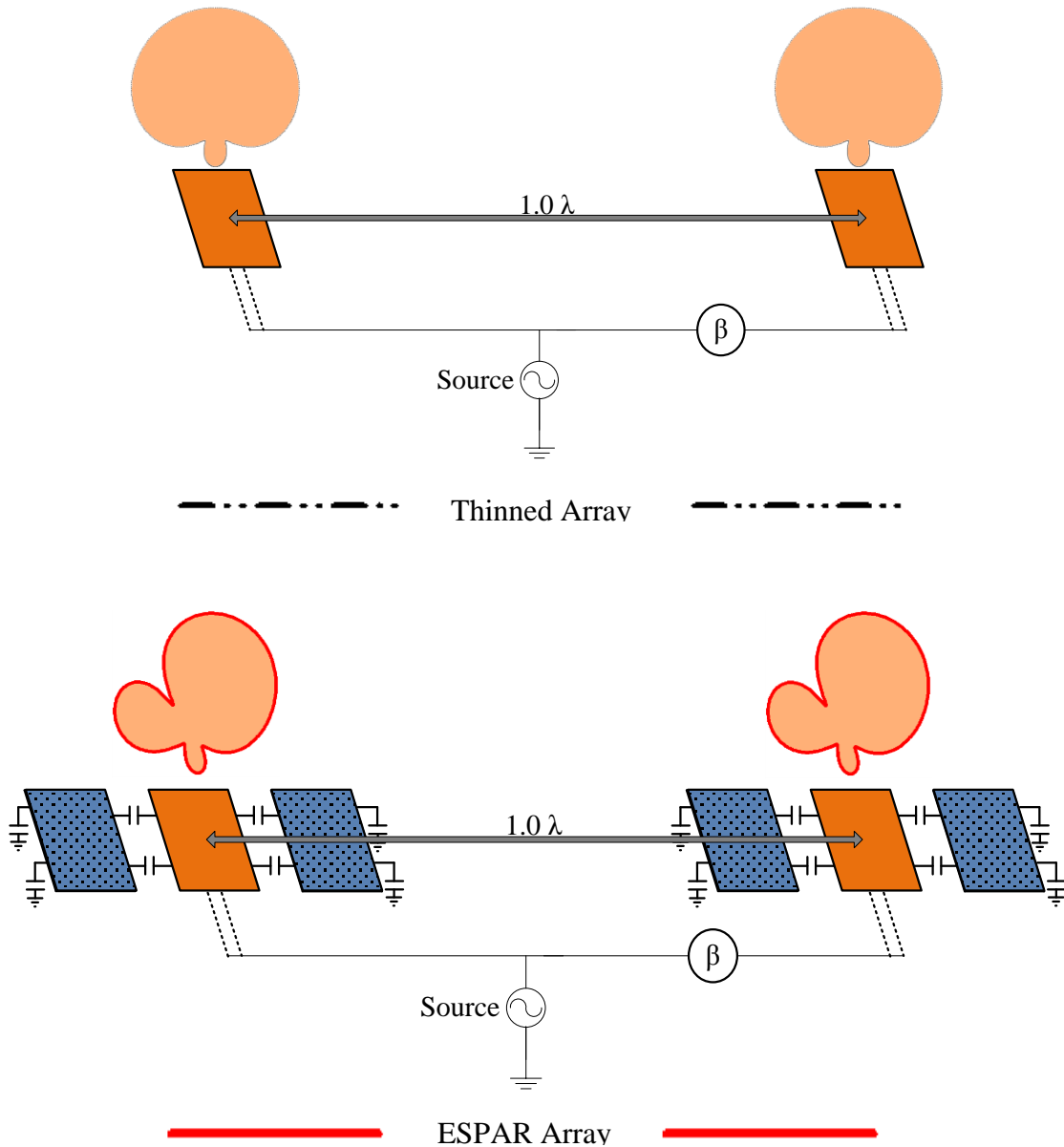
Figure 52: Illustration of the ESPAR and thinned scanning arrays with wavelength spacing.

While the full wavelength spacing utilized by the ESPAR can also be used for single patch antenna elements leading to the thinned array and reduced total phase shifters, the resulting array is prone to poor aperture efficiency and high side lobes. In the figure, patch elements identical to the ESPAR driven element are fed with a uniform progressive phase shift to scan to 20°. The ESPAR is similarly scanned, but is also scanned at the subarray cell level, resulting in a side lobe level more than 10 dB better than the thinned array.

7.2.2) ESPAR Single-Layer Subarray Cell Design

The subject phased array antenna employs the 3-element parasitic array presented in [20] as a subarray cell. Rogers RT-Duroid 5880 with thickness of 62 mil is utilized as the substrate, as the low permittivity and loss tangent (2.2 and 0.0009) each facilitate higher gain. A 50-ohm microstrip line carries the signal from the edge-mount SMA connector to a single driven patch antenna in the center of the subarray cell. A parasitic patch identical in size to the driven element is coupled in the H-Plane on each side. Two surface mount reverse-bias diode varactors are used in the gaps on either side of the driven element to directly connect with the parasitic patch antennas. These varactors are called the "coupling capacitors," designated C_CPL, and are used to control the mutual coupling. Each parasitic element is also loaded with grounded capacitors to compensate resonant frequency shifting. These are called "compensation capacitors" and are designated C_CMP. These capacitors are actively tuned by adjusting the reverse bias voltage across their terminals. The voltages are chosen based on the capacitive loading schemes determined in the simulation stage.

The voltages are fed to the system in 5 locations: the driven element and two parasitic elements are each biased at a different voltage, determined by the required loading schemes. The ground plane is biased with the final two voltages. Figure 53 shows the five nodes of the biasing circuit on the ESPAR subcells, as well as the common connections between corresponding nodes of different subcells in the array.
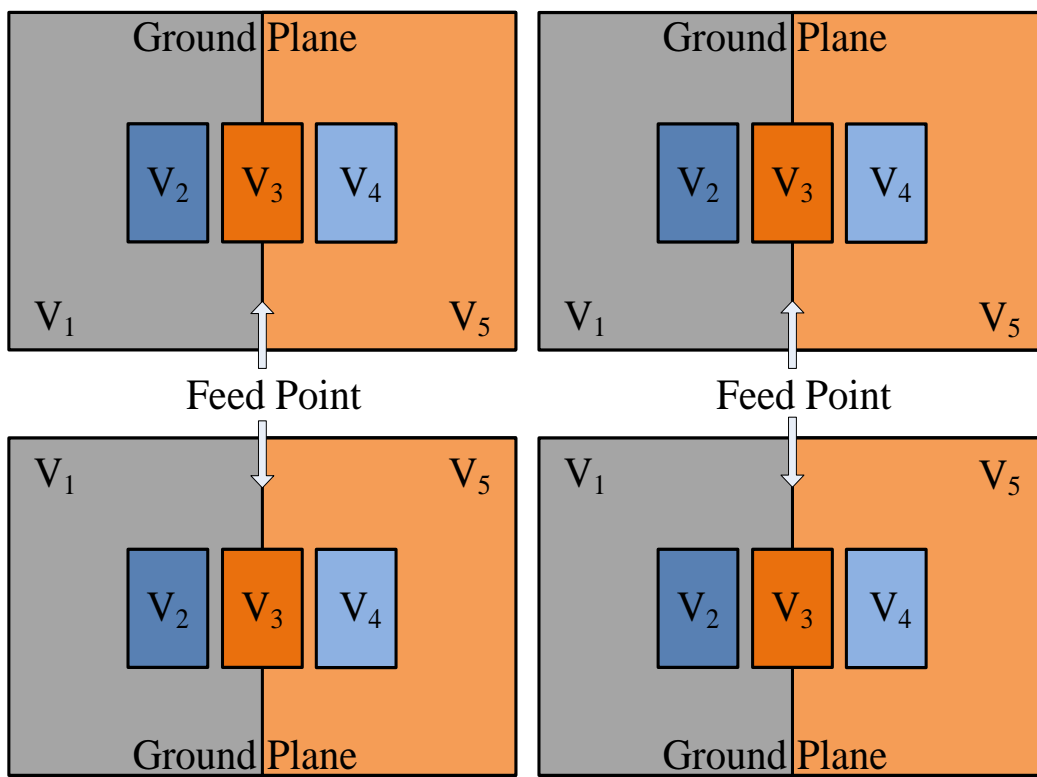
Figure 53: Varactor bias voltage scheme.

The specific orientation of the varactors anodes on a given subarray cell is chosen to simplify the DC biasing, as illustrated in the figure. Here, it is clear that two vertically aligned subarray cells, such as the upper and lower left, will share identical voltage differences from node to node, allowing greatly expedited and simplified verification of the biasing during

operation. To accomplish the independent DC nodes in the ground plane, a 100 micron groove is cut through the ground plane beneath the driven element to bisect it, creating two independent DC nodes. This groove splits into a V-shape to circumvent the SMA connector, which would otherwise short-circuit the two nodes, with the final shape of the groove being an inverted-Y. Simple wires are run from the DC voltage supplies and are connected to the ground planes and parasitic elements using the techniques from [20, 33].

A unique biasing scheme is utilized for the final node in the biasing circuit. The driven patch antenna is physically connected to the microstrip line, which is also shorted to the coaxial cable's signal line via the SMA connector. Therefore, all four driven elements and the signal traces of the feed network are at the same voltage potential. Instead of running a wire to directly connect to the driven patch antenna, a microstrip bias tee is utilized.

7.2.3) Array Feed Network

The corporate feed network used to route the RF signal to the ESPAR panels divides the signal equally to all four driven elements. First, the signal trace is set to the appropriate voltage by attaching a wire from the corresponding DC supply to the bias tee. This circuit is then connected to the Wilkinson power divider by an SMA cable, where the first equal power split occurs. This stage also applies any necessary phase shifting at the subarray cell level for scanning in the H-Plane. Smaller semi-rigid cables now feed the split signal into two ring hybrid couplers. The outputs are connected to the microstrip ESPAR panels through a final set of identical cables. The selections of the Wilkinson and Ring Hybrid couplers were made to

maintain a low-profile and compact feed network. In Figure 54, the wooden mounting structure is shown in transparent green.
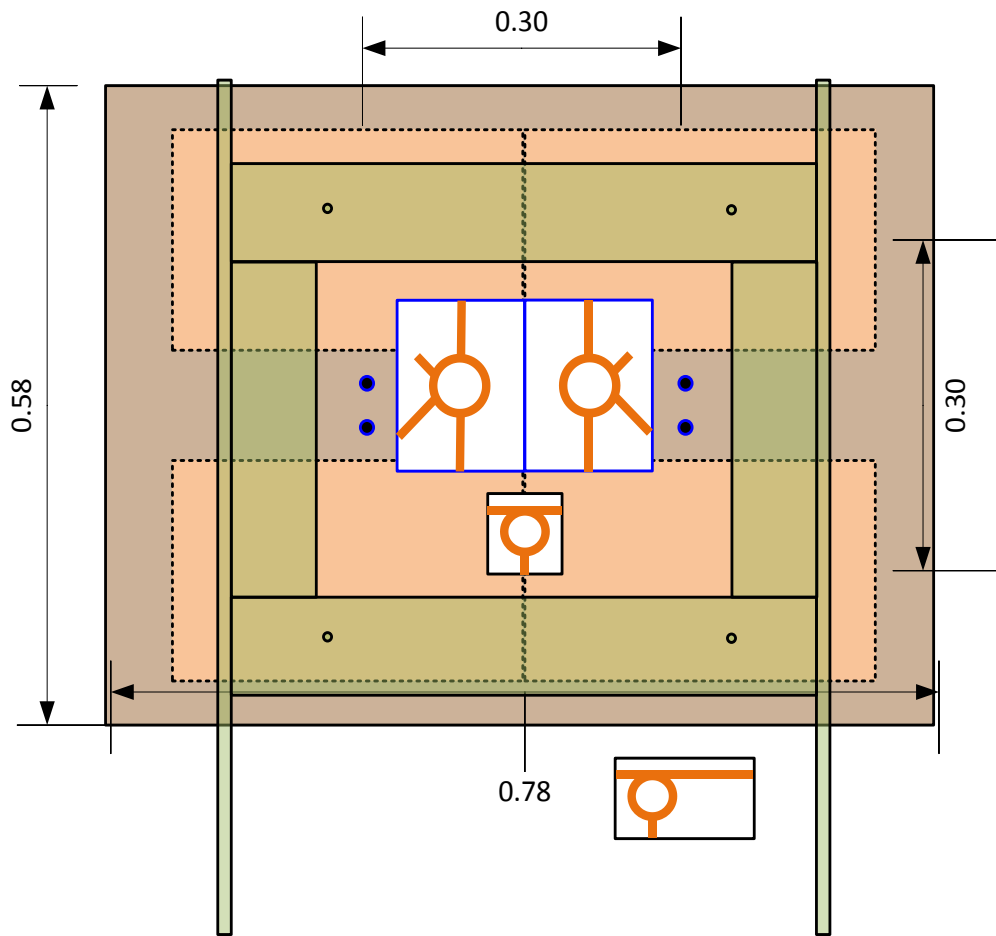
Dimensions given in meters.
Figure 54: Feed network layout and array mounting structure.

The feed network was required to fit within the inner boundary of the wooden section, requiring that the couplers be oriented as shown. The cables are omitted. In the lower right of the figure, an additional Wilkinson divider is shown with an additional delay line segment. For

demonstration purposes, these Wilkinson dividers are switched out to provide the appropriate subarray-level phase shifts for beam scanning.

(a)   Microstrip Radial Stub Bias Tee

The bias tee is utilized to introduce a DC voltage to the driven elements by biasing the signal traces throughout the entire feed network. The structure consists of a 50Ω microstrip through-line, which is connected at the center to a shunt high-impedance line. The high characteristic impedance of the narrow microstrip facilitates the shunt line connection without causing an impedance mismatch, preventing detrimental insertion loss. This quarter-wavelength line ends at the vertex of a radial stub, where the DC biasing wire is connected. The stub provides a virtual RF short in parallel with the DC wire, ensuring isolation between the RF signal trace and the DC power supply. The virtual short is transformed by the quarter-wavelength high-impedance line and appears as an open circuit to the RF circuit. A packaged SMA DC-block is attached to the radial stub circuit input to isolate the RF source from the DC voltage.

(b)   Wilkinson Power Divider

The Wilkinson power divider is a 3-port network capable of providing equal power division with identical output phase, and is therefore well-suited for the corporate feed network [21]. The model utilized is shown in Figure 55.
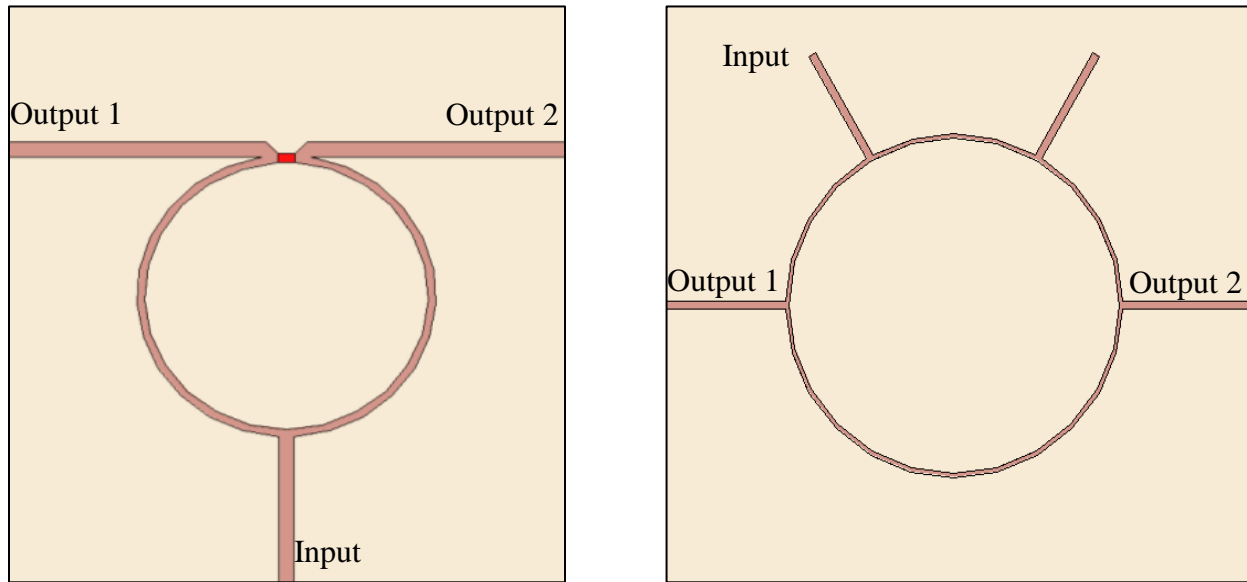
Figure 55: Feed network microstrip circuits. Left: Phase-balanced Wilkinson power divider. Right: Ring hybrid coupler.

The signal enters through the input port on the bottom, and is equally split across two quarter-wave arms with impedance of $\sqrt{2}Z_0$. The two arms meet again toward the top of the structure, where a 100Ω resistor is placed in series between them. The 50Ω output ports provide a balanced insertion loss of 3dB and equal phase shifts. Finally, phase shifting is accomplished for the scanned cases by appending some additional microstrip line length to the corresponding output port.

(c)   Ring Hybrid Coupler

The ring hybrid is a 4-port network with the ability to provide equal magnitude splitting and an output phase difference of 0° or 180°, with high return loss and low insertion loss [21]. For this array implementation, the footprint of the feed network and necessarily cabling length are significantly reduced by facing the subarray cells in opposite directions in the E-Plane. The

ring hybrid is utilized in the differential mode to overcome the inherent phase mismatch, with the orientation labeled in Figure 55. The signal is input at port 1, and is equally split with opposite phase shifts to ports 2 and 3.

7.3 Full-wave Simulation

7.3.1) Simulation Package and Configuration

A combination of Ansoft HFSS - a full-wave electromagnetic solver - and MATLAB post-processing were used to calculate the array performance. The ESPAR subarray cells are first simulated in HFSS. Then, the radiation patterns are exported to MATLAB, allowing analysis of the full array performance and calculation of the appropriate subarray cell-level phase shifts. These phase shifts are integrated as appended delay-line segments on the Wilkinson power dividers. Finally, absolute gain predictions are made by adding the subarray cell gains to the array factor directivity increase, and subtracting the feed circuit losses.

Following the design procedure outlined in [20], the 3-element microstrip patch ESPAR was created with the dimension shown in Figure 49. A wave port launches the 1 GHz signal along the microstrip line and lumped elements are used to simulate the effects of variable capacitive loads. Due to the negligible RF performance impact imposed by the biasing circuit, the DC biasing is excluded from the full-wave simulations. Loading configurations corresponding to desired scan cases are simulated, where the pattern quality, gain, and return loss are verified. The microstrip circuit elements were also simulated using HFSS. As aperture

efficiency is highly dependent on uniformity in the current distribution across the driven elements, the power dividers in the corporate feed network are tuned in simulation to achieve equal splitting. Further, optimal gain for the array is only achieved for high return loss in the feed network, necessitating that the impedance matching is maintained at all ports.

7.3.2) Simulation Results

The ESPAR cells were solved across a frequency sweep from 800 MHz to 1.2 GHz to illustrate the resonance behavior about the operation frequency of 1 GHz. A parametric analysis of the lumped element capacitor values provided the loading schemes. In each configuration, the changing capacitors alter the mutual coupling and parasitic element resonant frequencies. This results in varied parasitic element current distributions and therefore varied radiation patterns for each case. Simultaneously, the impedance matching at 1 GHz is monitored to ensure the scanning the radiation pattern does not result in heavily diminished gain; loading configurations which result in diminished impedance match are rejected. Table 4 records the loading configurations utilized in the final array.

Table 4: Measured ESPAR Array Performance for Various Scan Cases

Scan Angle [Deg]	ESPAR Array Performance Characteristics at 1 GHz							
	Gain [dBi]	First Side Lobe Level [dB]	Wilkinson Delay Phase, β_x [Deg]	Wilkinson Delay Line Length [mm]	C_CPL 1 Value [pF]	C_CPL 2 Value [pF]	C_CMP 1 Value [pF]	C_CMP 2 Value [pF]
-20	12.9	10.2	-127	62.0	2.0	3.5	0.8	2.3
-10	13.2	13.1	-62.5	31.25	2.0	3.0	1.3	3.0
0	13.6	11.3	0.0	0.0	3.0	3.0	4.0	2.0
10	13.2	13.1	62.5	31.25	3.5	2.0	3.0	1.3
20	12.9	10.2	127	62.0	3.5	2.0	2.3	0.8
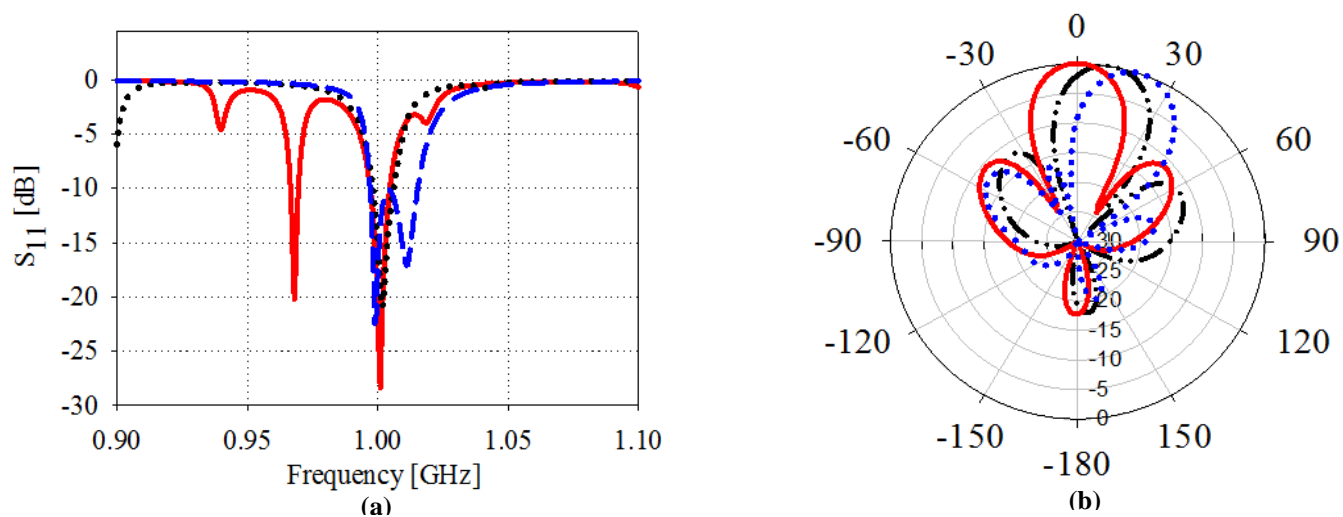
Figure 56: Simulated performance. (a) S11 vs. frequency. (b) Normalized radiation patterns (dBi) at 0°, 10°, and 20° scans.

7.4 Fabrication, Measurement, and Results

7.4.1) Fabrication Technique

The microstrip patch ESPAR array was fabricated using a combination of common PCB fabrication and custom handwork. The subarray cells were constructed first. Radiation and ground plane layer files were directly converted from the HFSS design file. A milling machine then patterned the copper patches, microstrip inset feed, capacitor lands, and grounding via pads. The majority of the fabrication handwork involved soldering the varactors to the radiation layer. These varactors, which are Infineon BB857H7902 surface mount chips, are soldered in 8 positions per subarray cell. The varactors are mounted to the patch layer visible in Figure 57 (a), and are oriented with all anodes facing in the same direction for a given subarray cell. This orientation ensures that the progression of bias voltages from node to node is monotonic and therefore easier to check during measurement. The narrow inverted-Y DC isolation groove on the ground plane was milled at 100 micron width using alignment pins to ensure the groove ran parallel to, and centered under, the driven patch, as shown in Figure 57 (b). The biasing and grounding via holes were machined with a drill press, then metallized by electroplating. As the biasing vias were simply through-holes for 0.5 mm diameter oxide-insulated DC wires, the electroplating was removed from these vias by hand with an appropriately small drill bit.
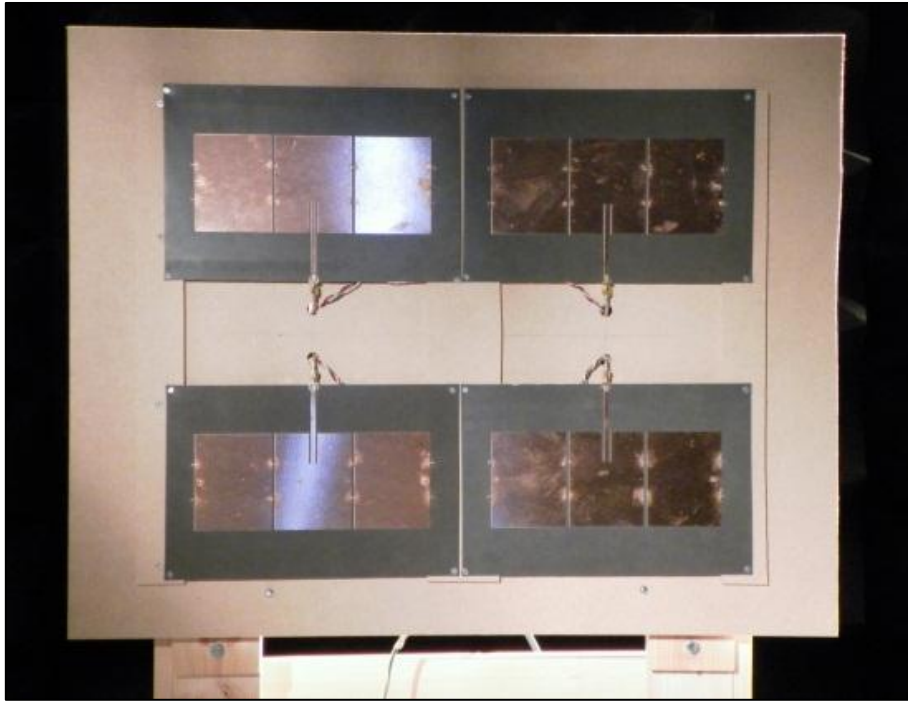
(a)
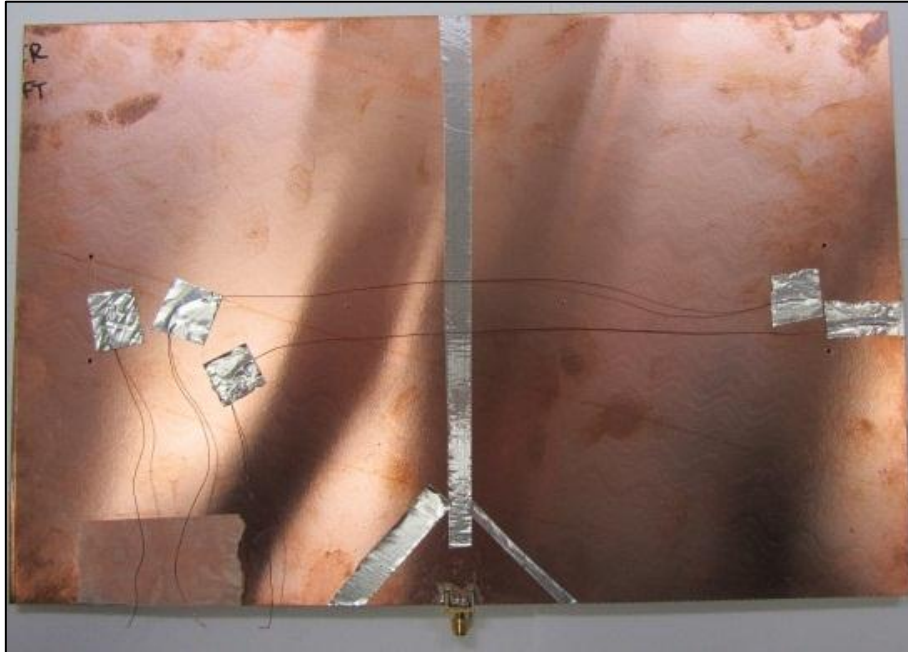
(b)

Figure 57: Photos of the functional ESPAR array. (a) Radiating surface. (b) Subarray cell ground plane with biasing wires and sealed groove measurement.
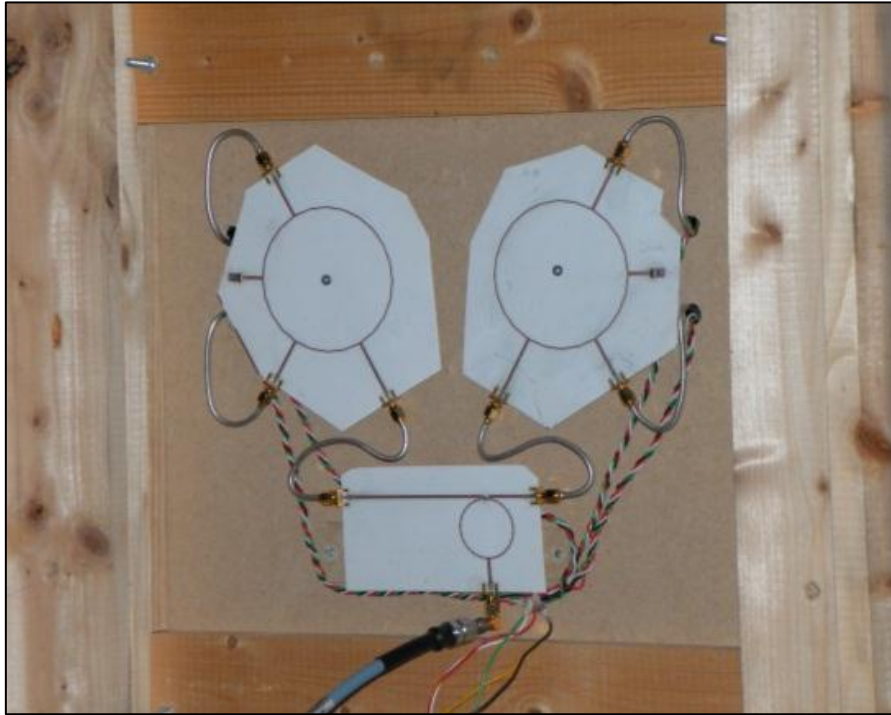
(a)
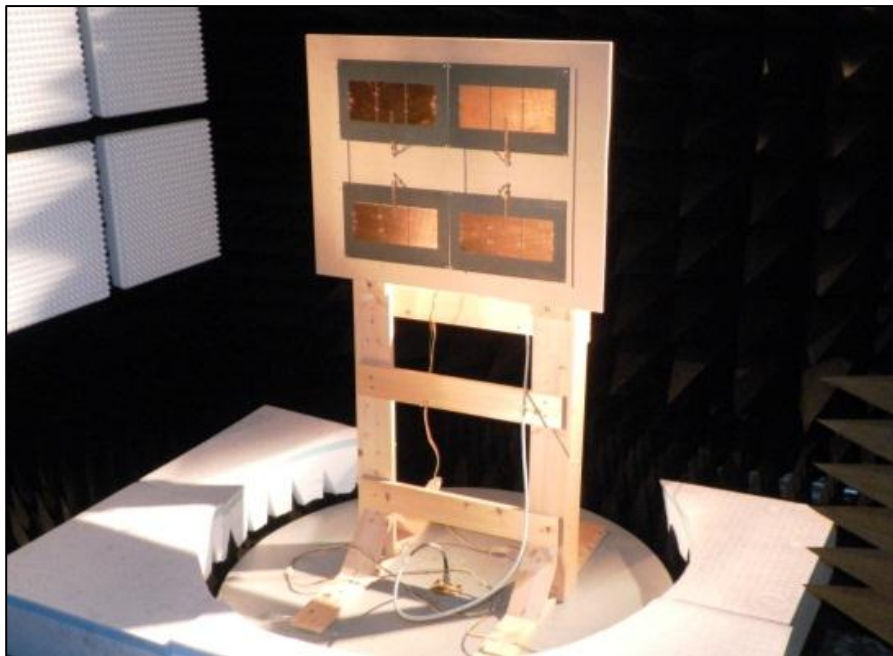
(b)

Figure 58: Photos of the functional ESPAR array. (a) Corporate feed network. (b) Mounted prototype during measurement.

103

Acid etching was the primary fabrication technique for the feed network microstrip circuits. The circuit traces were patterned on .032" thick Rogers 4003 substrates. A sodium persulfate bath was used to remove extraneous feed layer copper. Chip resistors are utilized in the Wilkinson power dividers; the 50Ω lines dictate a 100Ω resistance, which is achieved by soldering two 200Ω resistors in parallel, adjoining the output lines. This increases the maximum input power level for the RF signal compared to using a single 50Ω chip with the same form factor. The isolated ports on the ring hybrids are terminated to ground with a matched load. Similar to the Wilkinson circuits, four 200Ω resistors are placed in parallel between the signal trace and a grounding pad, matching the isolated port, as seen in Figure 58 (a). The symmetry of the array and mounting structure requires that the two ring hybrids are mirrored images of one another. This allows absolute symmetry through the entire feed network, and maintained equality in the phase delay through each branch.

The array was laid out to mount on the wooden structure visible in Figure 58 (b). The ESPAR panels were screwed to the ¼" thick fiber board, with ½" holes drilled through to pass the SMA cable and biasing wires. The microstrip circuits were cut on a band saw and screwed to the back side of the fiber board, oriented such that the entire feed network and cables fit within the support structure framing. This reduced the feed network footprint, conserving space and reducing electrical loss due to path length. Hand-formable 6" Amphenol SMA cables carry the RF signal from the Wilkinson power divider to the ring hybrids, and then on to the ESPAR panels through the holes in the fiber board.

7.4.2) DC Biasing

Active control over the radiation pattern scan angle requires variable reactance values, and therefore, adjustable reverse bias voltages over the varactors. A five-stranded braid of 22 AWG wires, visible in Figure 58 (a), connects to four DC voltage supplies, while one wire is grounded with respect to the biasing circuit. The highest and lowest voltages, V_1 and V_5, are connected to the two RF ground plane halves. V_2 and V_4 are soldered to the surface of the parasitic patches after being passed through the drilled vias. The final voltage, V_3, energizes the entire feed network signal trace simultaneously by way of the bias tee circuit.

The inverted-Y isolation groove is designed to minimize its impact on the RF performance of the array. However, this effect is not negligible and distorts both the resonant frequency of the center patch and the impedance of the microstrip line. These effects are nullified by the placement of a conductive aluminum tape over the entire groove. The thin adhesive film on the tape is not conductive. These conditions simulate a continuous RF ground plane in the vicinity of the groove while maintaining DC isolation of the ground plane halves.

7.4.3) Array Performance and Measurement Results

Following the fabrication and final assembly procedures, the ESPAR subarray cells were individually tested. A multimeter was used to check the consistency of forward bias voltage for the diode varactors between nodes. This served as verification that all varactors were functioning properly and were soldered sufficiently. The bias voltage wires were connected to the power supplies, and the voltages corresponding to the loading configurations of Table 4 were set. An

Agilent PNA-X was utilized to measure the input reflection characteristics for each configuration. These results are recorded below in Figure 59, where the response of each subarray cell is present for the boresight and 20° scan cases.
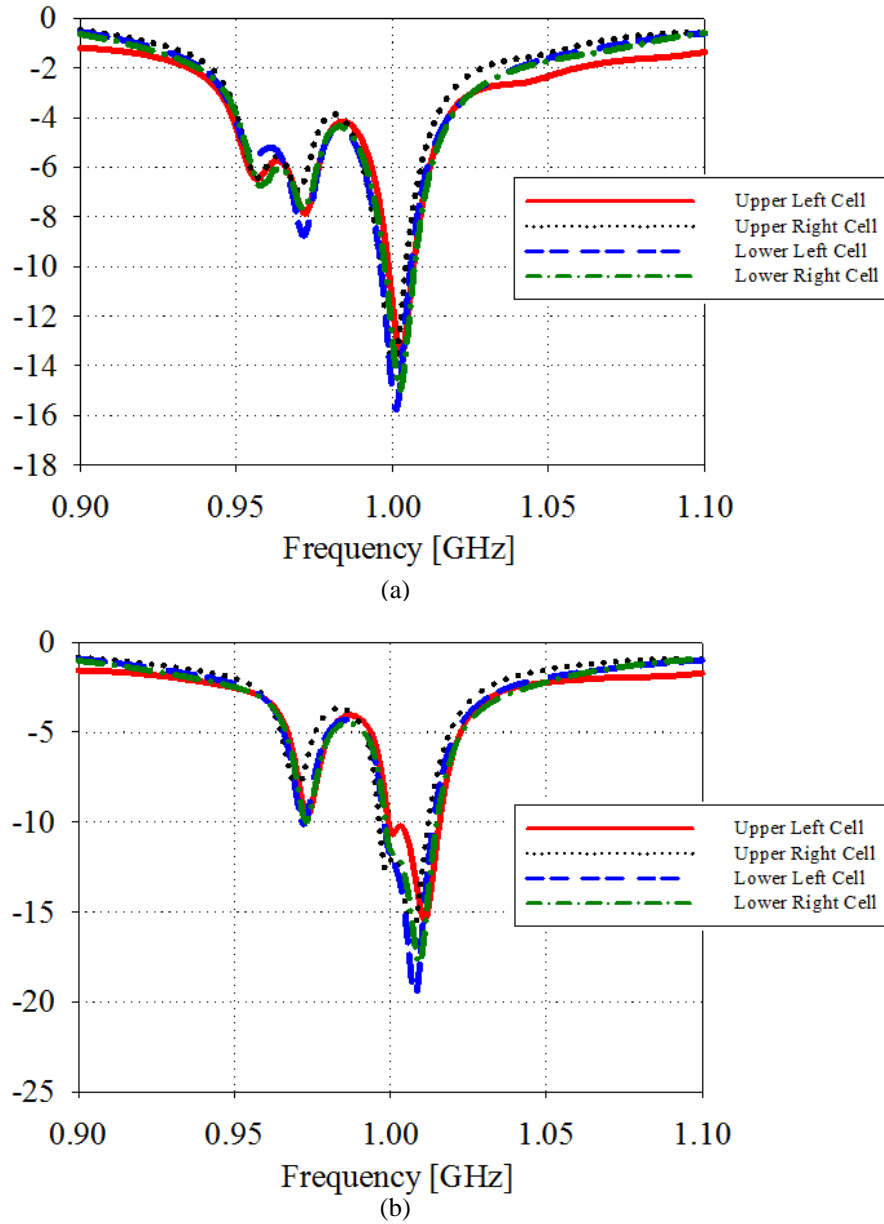

(a)

(b)

Figure 59: Measured scattering parameters for different scan angles. (a) Boresight. (b) 20°.

It is clear that the loading configurations cause large variations in the number, locations, and depth of the resonant nulls in S_{11}. These dips correspond to the resonance splitting often seen in filtering responses and are caused by the coupling of the resonant modes in the structure [29]. However, this additional resonance behavior does not increase the functional bandwidth. The return loss at 1 GHz is preserved better than 10 dB, verifying the full-wave simulations and indicating success in the utilization of the resonance compensation varactors.

The array was mounted inside the anechoic chamber at the University of Central Florida, where the radiation properties were then measured. The absolute gain of the array at boresight is measured to be 12.1 dBi, compared to the simulated gain of 13.6 dB. This difference is due to the non-ideal feed network in the measured device, which includes ohmic losses and phase mismatches in the couplers, whereas the simulation included no feed network loss and perfect phase shifts between subcells in both principal planes. The gain of the ESPAR array decreases roughly 0.5 dB across the scan range, as seen in Figure 60. This phenomenon is consistent from full-wave prediction to the measured device, as evidenced by the excellent matching in the shape of the two curves. Pattern measurements in the H-Plane are visible in Figure 61 for the five illustrated loading cases in Table 4. While only five patterns are shown, the scanning range is continuous from -20° to +20° and is only limited by the precision of the power supplies, as the varactors loads are analog devices. The pattern main lobes match the simulated results exceptionally well in both beamwidth and direction of peak gain, showing continuous scanning across the -20° to +20° range.
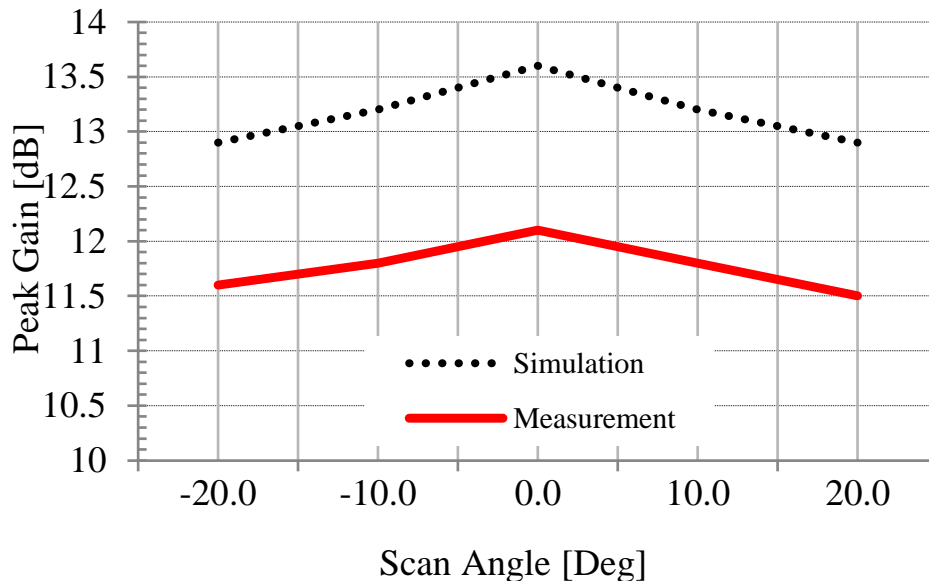
Figure 60: Absolute gain versus scan angle.

The location and relative level of the sidelobes match with similar accuracy for the boresight and ±10° scans, with the sidelobe level better than 10 dB below peak gain. In the ± 20° scans, the sidelobe level worsens to 8.5 and 7.0 dB below peak gain, compared to the simulated level of 10 dB. This is due to the non-ideality of the varactors used when pushed to their minimal capacitance value. The inner-subcell phase difference is consequently larger than the simulated values, causing growth of the sidelobe. One method to avoid such issues in the future would be to move the varactors closer to the center of the patch, where larger values of capacitance would produce the same loading effect while avoiding pushing the varactors to their extreme value.

(a) **-15°.** (b) **-7 °.** (c) **0 °.** (d) **7 °.** (e) **15 °.**
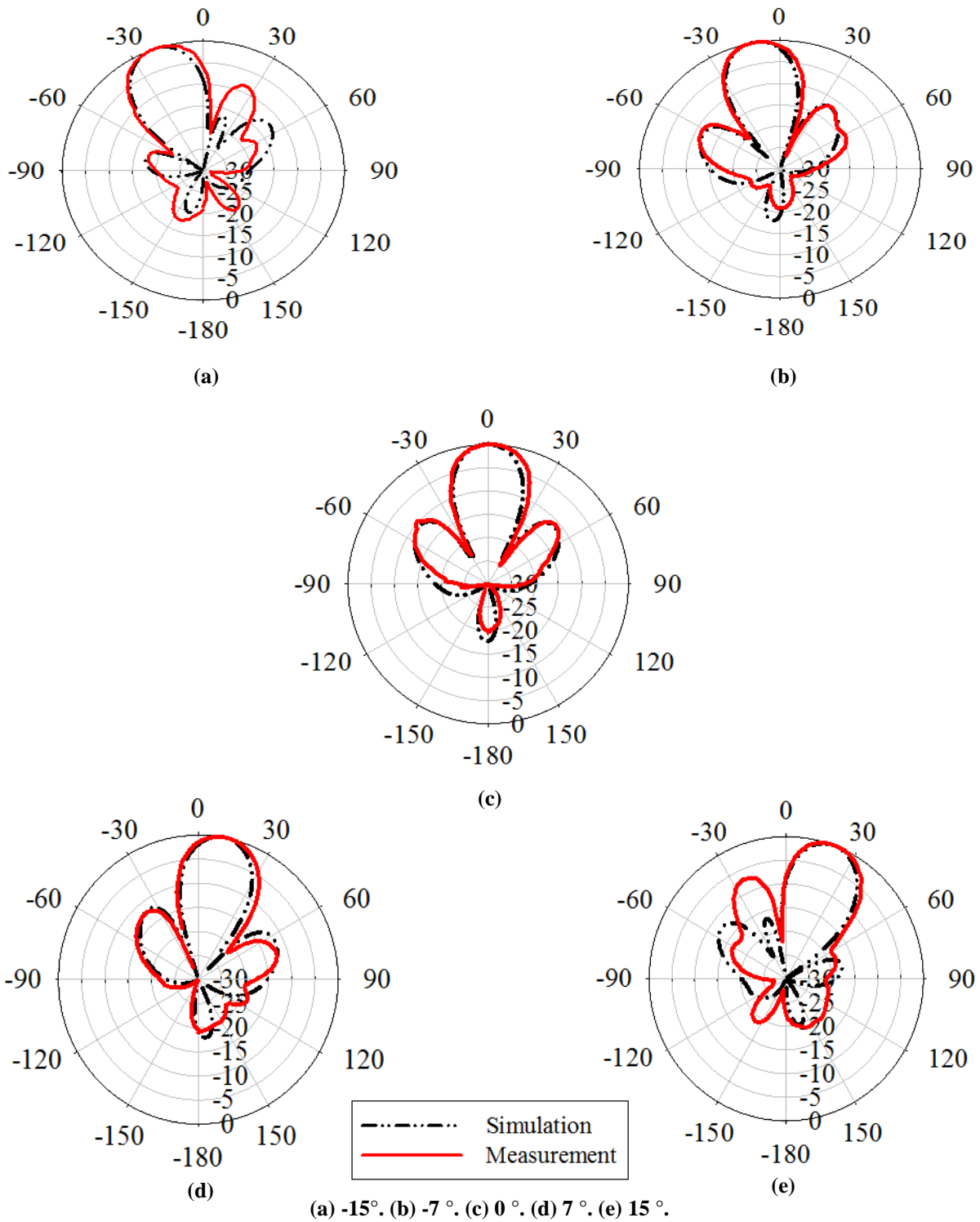
Figure 61: Simulated and measured normalized linear gain patterns for different scanning angles.

109

7.5 Conclusion

Integration of the microstrip ESPAR into a larger planar array has been presented for the first time. The combination of a compact feed network with the 3-element microstrip ESPAR phased array has produced an array capable of beam scanning with reduced phase shifters and cost compared to a traditional uniform array, with better side lobes and gain than the thinned patch array. This proof of concept enables even further integration of the ESPAR technique into existing phased array antenna design methods.

The application of the ESPAR technique to planar arrays must be studied further to enable improvements to scan range and gain. For example, designs incorporating coupled cavity-backed slot antennas will allow high-magnitude coupling, ensuring high aperture efficiency and low side lobes across the scan range. Additionally, traditional uniform arrays with half-wavelength spacing, intended for applications requiring low-sidelobes would benefit from the introduction of phase-correcting parasitic elements similar to the use in the microstrip ESPAR.

CHAPTER 8: CONCLUSIONS, PERSPECTIVES, AND FUTURE WORK

8.1   Summary

The cost benefit associated with reducing T/R modules in phased array antennas has inspired novel pattern reconfigurability techniques in the recent literature. However, until recently, a trade-off between critical performance metrics for large scanning arrays was necessary. The desire for inexpensive, highly directive, high return loss phased array antennas had not yet been satisfied.

The introduction of the microstrip patch ESPAR has enabled inexpensive phased array fabrication without sacrificing RF performance. The introduction of the coupling and compensation varactors between the patch elements has exhibited the explicit mutual coupling control for the first time. As standalone 2 or 3 element arrays, the microstrip patch ESPAR achieves continuous range beam scanning with maintained gain, high return loss, and low sidelobes. The simplification of the patch ESPAR fabrication technique to a single layer has proven critically important to further expansion of this phased array type; for example, on-wafer designs at K_A-band and above require that the array topology be single-layered. Functional prototypes at 1 GHz provide proof that the reactively controlled directive array concept can alleviate cost and power requirements for wireless transceivers.

Electrically-large phased array antennas will benefit from the patch ESPAR array integration method explored in this dissertation. The simplicity of the control network and ability

to maintain resonance at the desired operation frequency for many pattern shapes allow advanced array techniques, such as beam synthesis and adaptive control, to be explored. With these methods, the high directivity associated with large radiating apertures will be coupled with the null-steering benefits to SINR while reducing the prohibitive fabrication cost. Low-cost target track radar systems can be fabricated with the simultaneous ability to detect targets at long range while reducing sensitivity to electronic countermeasures such as jamming systems.

8.2 Future Work

8.2.1) On-Wafer ESPAR Arrays

Expansion of the ESPAR to include microstrip patches has opened up the possibility for numerous applications. With the complexity reduction of the single-layer design, on-wafer superdirective arrays are possible. While lumped components are subject to frequency limitation by way of packaging parasitic effects, the use of ferroelectric materials such as barium-strontium-titanate (BST) can relieve this requirement. In this manner, the surface-mount capacitors on the patch edges can be replaced by interdigital capacitors (IDC), with similar biasing to the demonstrated ESPAR prototypes. This will allow the development of inexpensive conformal antenna arrays using BST phase shifters and varactors on LCP using the technique in [45]. The first step in integrating the BST material in the patch ESPAR design will be to characterize the tuning effect of the dielectric on the ESPAR coupling level. Then, the techniques

described throughout this work can be utilized to demonstrate a scanning array with on-wafer fabrication.

8.2.2) E-Plane Parasitic Coupling and Additional Element Types

The second further development area will see the microstrip patch ESPAR include E-Plane parasitically-coupled elements and scanning along these two dimensions. By carefully controlling the coupling between the four parasitic elements and the driven element in the cross-shape while compensating for the resonance of the structure, the return loss can be maintained to an acceptable level while scanning fully along theta and phi simultaneously.

Finally, the mutual coupling control method explored in this dissertation will allow expansion of the ESPAR technique to even more broadside radiator types. For example, Figure 62 shows the concept of an ESPAR antenna utilizing coupled-resonator cavity-backed slot antennas.
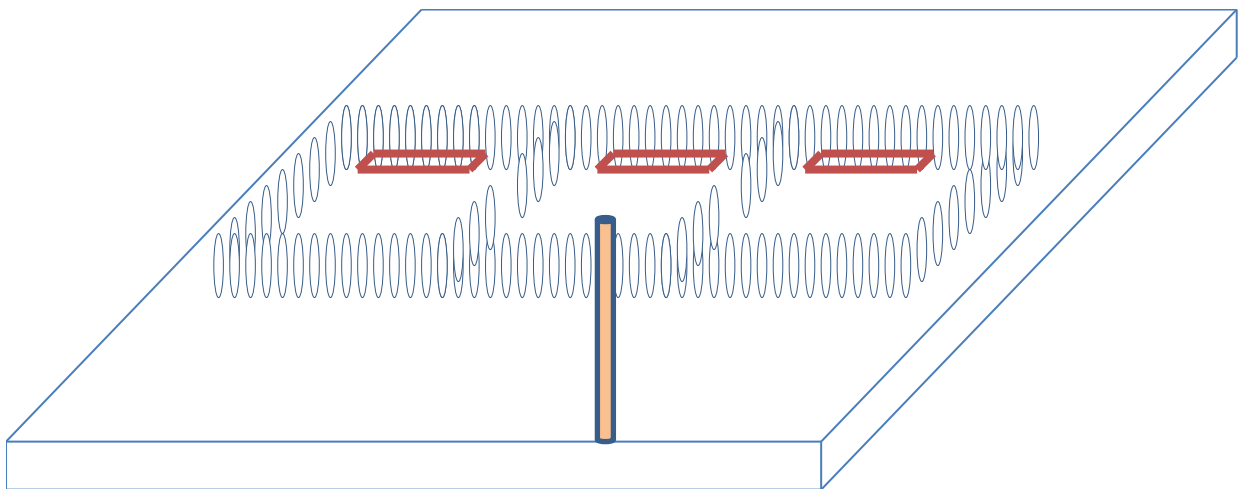
Figure 62: Cavity-backed Slot Antenna ESPAR Concept.

In this design, the high-Q nature of EBG cavities on low-loss substrates will allow excellent aperture efficiency by maintaining a high coupling level. Finally, this technique can be further improved with the filter-antenna integration technique explored in [46]. This will result in compact, highly-efficient, and cost-effect scanning phased array antennas for a wide range of applications.

REFERENCES

[1]   G. M. Rebeiz, *RF MEMS: Theory, Design, and Technology*: Wiley, 2004.

[2]   A. S. Nagra and R. A. York, "Distributed analog phase shifters with low insertion loss," *Microwave Theory and Techniques, IEEE Transactions on,* vol. 47, pp. 1705-1711, 1999.

[3]   M. Fakharzadeh, P. Mousavi, S. Safavi-Naeini, and S. H. Jamali, "The Effects of Imbalanced Phase Shifters Loss on Phased Array Gain," *Antennas and Wireless Propagation Letters, IEEE,* vol. 7, pp. 192-196, 2008.

[4]   G. H. Huff and J. T. Bernhard, "Integration of packaged RF MEMS switches with radiation pattern reconfigurable square spiral microstrip antennas," *Antennas and Propagation, IEEE Transactions on,* vol. 54, pp. 464-469, 2006.

[5]   S. Nikolaou, R. Bairavasubramanian, C. Lugo, I. Carrasquillo, D. Thompson, G. E. Ponchak*, et al.*, "Pattern and frequency reconfigurable annular slot antenna using PIN diodes," *Antennas and Propagation, IEEE Transactions on,* vol. 54, pp. 439-448, 2006.

[6]   D. Peroulis, K. Sarabandi, and L. P. B. Katehi, "Design of reconfigurable slot antennas," *Antennas and Propagation, IEEE Transactions on,* vol. 53, pp. 645-654, 2005.

[7]   D. Gray, L. Jun Wei, and D. V. Thiel, "Electronically steerable Yagi-Uda microstrip patch antenna array," *Antennas and Propagation, IEEE Transactions on,* vol. 46, pp. 605-608, 1998.

[8]   R. Harrington, "Reactively controlled directive arrays," *Antennas and Propagation, IEEE Transactions on,* vol. 26, pp. 390-395, 1978.

[9]   H. Yagi, "Beam Transmission Of Ultra Short Waves," *Proceedings of the IEEE,* vol. 85, pp. 1864-1874, 1997.

[10]   T. Ohira and K. Gyoda, "Electronically steerable passive array radiator antennas for low-cost analog adaptive beamforming," in *Phased Array Systems and Technology, 2000. Proceedings. 2000 IEEE International Conference on*, 2000, pp. 101-104.

[11]   R. Schlub, L. Junwei, and T. Ohira, "Seven-element ground skirt monopole ESPAR antenna design from a genetic algorithm and the finite element method," *Antennas and Propagation, IEEE Transactions on,* vol. 51, pp. 3033-3039, 2003.

[12]   J. Lu, D. Ireland, and R. Schlub, "Dielectric Embedded ESPAR (DE-ESPAR) Antenna Array for Wireless Communications," *Antennas and Propagation, IEEE Transactions on,* vol. 53, pp. 2437-2443, 2005.

[13]   G. Kumar and K. C. Gupta, "Broad-band microstrip antennas using additional resonators gap-coupled to the radiating edges," *Antennas and Propagation, IEEE Transactions on,* vol. 32, pp. 1375-1379, 1984.

[14]   Y. K. Cho, G. H. Son, G. S. Chae, L. H. Yun, and J. Hong, "Improved analysis method for broadband rectangular microstrip antenna geometry using E-plane gap coupling," *Electronics Letters,* vol. 29, pp. 1907-1909, 1993.

[15]   D. Pozar, "Input impedance and mutual coupling of rectangular microstrip antennas," *Antennas and Propagation, IEEE Transactions on,* vol. 30, pp. 1191-1196, 1982.

[16]   Y. Yusuf and G. Xun, "A Low-Cost Patch Antenna Phased Array With Analog Beam Steering Using Mutual Coupling and Reactive Loading," *Antennas and Wireless Propagation Letters, IEEE,* vol. 7, pp. 81-84, 2008.

[17]   J. Seongheon, H. Dohyuk, and W. J. Chappell, "A planar parasitic array antenna for tunable radiation pattern," in *Antennas and Propagation Society International Symposium, 2009. APSURSI '09. IEEE*, 2009, pp. 1-4.

[18]   C. A. Balanis, *Antenna Theory: Analysis and Design*: Wiley, 2012.

[19]   K. K. Karnati, Y. Yusuf, S. Ebadi, and G. Xun, "Theoretical Analysis on Reflection Properties of Reflectarray Unit Cells Using Quality Factors," *Antennas and Propagation, IEEE Transactions on,* vol. 61, pp. 201-210, 2013.

[20]   J. J. Luther, S. Ebadi, and X. Gong, "Single-layer design of microstrip patch Electrically Steerable Parasitic Array Radiator (ESPAR) with integrated DC isolation," in *Microwave Symposium Digest (MTT), 2012 IEEE MTT-S International*, 2012, pp. 1-3.

[21]   D. M. Pozar, *Microwave Engineering*: Wiley, 2004.

[22]   R. Schlub and D. V. Thiel, "Switched parasitic antenna on a finite ground plane with conductive sleeve," *Antennas and Propagation, IEEE Transactions on,* vol. 52, pp. 1343-1347, 2004.

[23]   H. Kawakami and T. Ohira, "Electrically steerable passive array radiator (ESPAR) antennas," *Antennas and Propagation Magazine, IEEE,* vol. 47, pp. 43-50, 2005.

[24]   J. B. L. Rao, G. V. Trunk, and D. P. Patel, "Two low-cost phased arrays," in *Phased Array Systems and Technology, 1996., IEEE International Symposium on*, 1996, pp. 119-124.

[25]   M. R. Islam and M. Ali, "Elevation Plane Beam Scanning of a Novel Parasitic Array Radiator Antenna for 1900 MHz Mobile Handheld Terminals," *Antennas and Propagation, IEEE Transactions on,* vol. 58, pp. 3344-3352, 2010.

[26]   S. L. Preston, D. V. Thiel, J. W. Lu, S. G. O'Keefe, and T. S. Bird, "Electronic beam steering using switched parasitic patch elements," *Electronics Letters,* vol. 33, pp. 7-8, 1997.

[27]   E. Van Lil and A. Van de Capelle, "Transmission line model for mutual coupling between microstrip antennas," *Antennas and Propagation, IEEE Transactions on,* vol. 32, pp. 816-821, 1984.

[28]   R. Jedlicka, M. Poe, and K. Carver, "Measured mutual coupling between microstrip antennas," *Antennas and Propagation, IEEE Transactions on,* vol. 29, pp. 147-149, 1981.

[29]   H. A. Haus, *Waves and fields in optoelectronics*: Prentice-Hall, 1984.

[30]   J. Zhang and A. Mortazawi, "An L-band tunable microstrip antenna using multiple varactors," in *Antennas and Propagation Society International Symposium, 2003. IEEE*, 2003, pp. 524-527 vol.4.

[31]   D. V. Thiel and V. Moyle, "Using mutual coupling to calculate the radiation pattern for parasitic patch antennas," in *Antennas and Propagation Society International Symposium, 2003. IEEE*, 2003, pp. 597-600 vol.1.

[32]   E. Erdil, K. Topalli, M. Unlu, O. A. Civi, and T. Akin, "Frequency Tunable Microstrip Patch Antenna Using RF MEMS Technology," *Antennas and Propagation, IEEE Transactions on,* vol. 55, pp. 1193-1196, 2007.

[33]   J. J. Luther and G. Xun, "A microstrip patch phased array antenna with parasitic elements and reactance-tuned coupling," in *Antennas and Propagation (APSURSI), 2011 IEEE International Symposium on*, 2011, pp. 3291-3294.

[34]   J. J. Luther, S. Ebadi, and G. Xun, "A Microstrip Patch Electronically Steerable Parasitic Array Radiator (ESPAR) Antenna With Reactance-Tuned Coupling and Maintained Resonance," *Antennas and Propagation, IEEE Transactions on,* vol. 60, pp. 1803-1813, 2012.

[35]   J. J. Luther, S. Ebadi, and G. Xun, "Electrically steerable Parasitic Array Radiator (ESPAR) antenna design for arrays with two and three parasitically-coupled elements," in *Radio and Wireless Symposium (RWS), 2012 IEEE*, 2012, pp. 79-82.

[36]   B. Yan-Ying, X. Shaoqiu, T. Ming-Chun, D. Zhuo-Fu, and W. Bing-Zhong, "Wide-Angle Scanning Phased Array With Pattern Reconfigurable Elements," *Antennas and Propagation, IEEE Transactions on,* vol. 59, pp. 4071-4076, 2011.

[37]   P. Zivin and L. Jenshan, "A Beam-Steering Broadband Microstrip Antenna for Noncontact Vital Sign Detection," *Antennas and Wireless Propagation Letters, IEEE,* vol. 10, pp. 235-238, 2011.

[38]   R. J. Mailloux, *Phased Array Antenna Handbook*: Artech House, 2005.

[39]   B. Elamaran, C. Iao-Mak, C. Liang-Yu, and C. Jung-Chih, "A beam-steerer using reconfigurable PBG ground plane," in *Microwave Symposium Digest. 2000 IEEE MTT-S International*, 2000, pp. 835-838 vol.2.

[40]   C. J. Panagamuwa, A. Chauraya, and J. C. Vardaxoglou, "Frequency and beam reconfigurable antenna using photoconducting switches," *Antennas and Propagation, IEEE Transactions on,* vol. 54, pp. 449-454, 2006.

[41]   S. Zhang, G. H. Huff, J. Feng, and J. T. Bernhard, "A pattern reconfigurable microstrip parasitic array," *Antennas and Propagation, IEEE Transactions on,* vol. 52, pp. 2773-2776, 2004.

[42]   K. Gyoda and T. Ohira, "Design of electronically steerable passive array radiator (ESPAR) antennas," in *Antennas and Propagation Society International Symposium, 2000. IEEE*, 2000, pp. 922-925 vol.2.

[43]   L. Junwei, R. Schlub, and T. Ohira, "A performance comparison of smart antenna technology for wireless mobile computing terminals," in *Microwave Conference, 2001. APMC 2001. 2001 Asia-Pacific*, 2001, pp. 581-584 vol.2.

[44]   D. H. Johnson and D. E. Dudgeon, *Array signal processing: concepts and techniques*: P T R Prentice Hall, 1993.

[45]   S. Ya, S. Ebadi, P. Wahid, and G. Xun, "Tunable and flexible Barium Strontium Titanate (BST) varactors on Liquid Crystal Polymer (LCP) substrates," in *Microwave Symposium Digest (MTT), 2012 IEEE MTT-S International*, 2012, pp. 1-3.

[46]   Y. Yusuf and X. Gong, "Compact Low-Loss Integration of High-Q 3D Filters with Highly Efficient Antennas," *Microwave Theory and Techniques, IEEE Transactions on,* vol. 59, pp. 857-865, 2011.